

Doctoral Dissertation (Censored)

博士論文（要約）

Magnetoluminescence of Organic Radicals:
Luminescence-Spin Correlated Properties
Controlled by a Degree of Assembly

（有機ラジカルにおける磁場応答発光：
凝集度により制御される発光 - スピン相関物性）

A Dissertation Submitted for the Degree of Doctor of Philosophy

December 2020

令和2年12月博士（理学）申請

Department of Chemistry, School of Science,

The University of Tokyo

東京大学大学院理学系研究科

化学専攻

Shun Kimura

木村 舜

Abstract

本内容の一部については、5年以内に雑誌等で刊行予定のため、非公開。

Organic radicals with unpaired electrons have been contributing to organic materials science through providing unique electronic and magnetic properties, which are correlated with their spin states. However, spin-correlated luminescence properties in organic radicals have never been accomplished despite their prospect as an approach to yield novel photofunctions unique to radicals. This thesis describes magnetic-field-sensitive luminescence, magnetoluminescence of organic radicals as the first photofunction of radicals based on the interplay between spin and luminescence.

Chapter 1: I described general introduction on organic radicals, including magnetic, electric, and catalytic properties and their emerging interests as luminescent materials.

Chapter 2:

Chapter 3: The luminescence properties of (3,5-dichloro-4-pyridyl)bis(2,4,6-trichlorophenyl)methyl radical (PyBTM) doped in host molecular crystals were investigated. The 0.05 wt%-doped crystals showed an excellent emission quantum yield of 0.89 at room temperature. The magnetoluminescence in organic radicals was observed for the first time in 4, 10, and 20 wt%-doped crystals. The key factors of the magnetoluminescence were determined as the magnetic-field-sensitive spin sublevel population of aggregated radicals in the ground states.

Chapter 4: I aimed to expand the scope of radical compounds showing magnetoluminescence. Zn^{II} complexes with ligated PyBTM doped in host matrices were prepared. The 5, 10, and 20 wt%-doped crystals showed magnetic-field-sensitive emission, suggesting the generality of magnetoluminescence for doublet emitters.

Chapter 5:

Chapter 6: The achievements in this thesis were summarized as concluding remarks.

Contents

Abstract

Chapter 1	General introduction	1
1-1	Organic radicals	2
1-1-1	Stable organic radicals	2
1-1-2	Unique properties of organic radicals	3
1-2	Luminescent organic radicals	6
1-2-1	Luminescence of organic radicals	6
1-2-2	Polychlorinated triphenylmethyl radical	8
1-2-3	Pyridyl-substituted triarylmethyl radicals	11
1-3	Aim of this research	13
1-4	References	15
Chapter 2	Open-shell 2D coordination polymers based on a tris-pyridyl-substituted triarylmethyl radical	19
2-1	Introduction	20
2-1-1	Radical-based 2D coordination polymers	20
2-1-2	trisPyM	21
2-2	Experimental section	23
2-2-1	Materials	23
2-2-2	Syntheses	23
2-2-3	Instruments and experimental methods	28
2-3	Results and discussion	31
2-3-1	Preparation and characterization of trisPyM	31
2-3-2	Electronic properties of trisPyM	36
2-3-3	Electrochemistry of trisPyM	38
2-3-4	Optical properties of trisPyM	39
2-3-5	Photostability of trisPyM	45
2-3-6	Preparations of trisZn and trisCu	47
2-3-7	Luminescence and magnetic properties of trisZn	53
2-3-8	Magnetic property of trisCu	56
2-3-9	Preparation of trisZnTPP	61

2-4	Conclusions	63
2-5	References	64

Chapter 3 Magnetoluminescence of PyBTM doped in matrices 67

3-1	Introduction	68
3-1-1	Magnetic field effect	58
3-1-2	Magnetoluminescence of radicals	69
3-2	Experimental section	71
3-2-1	Materials	71
3-2-2	Instruments and experimental methods	71
3-3	Results and discussion	76
3-3-1	Preparation of Py_R	76
3-3-2	Optical properties of Py_R at ambient conditions	80
3-3-3	Magnetoluminescence of Py_R	87
3-3-4	Doping concentrations dependency of magnetoluminescence of Py_R	93
3-3-5	Temperature dependency of magnetoluminescence of Py_R	96
3-3-6	Mechanism of magnetoluminescence of Py_R	99
3-4	Conclusions	108
3-5	References	109

Chapter 4 Magnetoluminescence of PyBTM-based Zn^{II} complexes doped in matrices 113

4-1	Introduction	114
4-2	Experimental section	116
4-2-1	Materials	116
4-2-2	Syntheses of Zn ^{II} (hfac) ₂ (α H-PyBTM) ₂	116
4-2-3	Instruments and experimental methods	117
4-3	Results and discussion	120
4-3-1	Preparation of PyZn_R	120
4-3-2	Optical properties of PyZn at ambient conditions	123
4-3-3	Magnetoluminescence of PyZn	128
4-4	Conclusions	133
4-5	References	134

Chapter 5 Magnetoluminescence of radical-based coordination polymers

135

5-1	Introduction	136
5-2	Experimental section	138
5-2-1	Materials	138
5-2-2	Syntheses of $[\text{Zn}^{\text{II}}(\text{hfac})_2(\text{bisPyTM})]_n$ (bisZn)	138
5-2-3	Instruments and experimental methods	139
5-3	Results and discussion	141
5-3-1	Preparation of the compounds	141
5-3-2	Magnetic properties	143
5-3-3	Luminescence properties	145
5-3-4	Magnetoluminescence properties	146
5-4	Conclusions	157
5-5	References	158

Chapter 6 Concluding remarks

159

Appendix

163

Crystallographic data of trisPyM	164
Crystallographic data of trisZn	167
Crystallographic data of trisCu	174
Crystallographic data of trisZnTPP	181
Crystallographic data of bisZn	186

List of publications

191

Acknowledgement

193

Chapter 1

General introduction

1-1 Organic radicals

1-1-1 Stable organic radicals

Organic radicals with an unpaired electron have been known as highly reactive and unstable species. Since the discovery of triphenylmethyl radical in 1900 by M. Gomberg,¹ many studies have been conducted on improving the stabilities of radicals.² To date, two methods are known as representative ways to obtain stable radicals: kinetic stabilization by the introductions of bulky groups to protect radical centers and thermodynamic stabilization by the delocalization of electronic spins.²⁻⁴ By combining these methods, there have been many reports of stable organic radicals to date, which can be treated under ambient conditions. These include triarylmethyl radical derivatives, 2,2,6,6-tetramethylpiperidine 1-oxyl (TEMPO) derivatives, nitronyl nitroxide derivatives, and phenalenyl derivatives (Figure 1-1-1).²

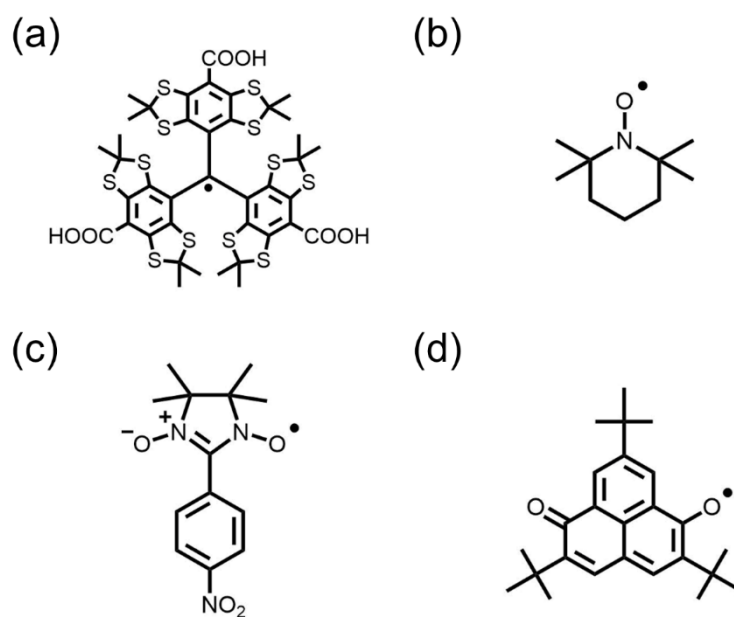


Figure 1-1-1. Examples of stable organic radicals. (a) a tetrathiatriarylmethyl radical derivative and (b) TEMPO (c) *p*-nitrophenyl nitronyl nitroxide (*p*-NPNN), and (d) 2,5,8-tri-*tert*-butyl-6-oxophenalenoxyl.

1-1-2 Unique properties of organic radicals

Studies on stable radicals have revealed unique magnetic, electric and catalytic properties attributed to their unpaired electrons. Magnetic properties of materials are governed by exchange interactions between spins induced by overlaps of spin orbitals. Scientists have tried to achieve an organic ferromagnet by designing molecules since the 1930's⁵ and *p*-NPNN (Figure 1-1-1c) was reported as the first example in 1991 by M Kinoshita *et al.* (Figure 1-1-2).⁶ Continuous efforts for improving the performance of magnets have realized various types of magnets, including room temperature magnets based on pure organic radicals⁷ or metal-organic magnets with ordering temperature at 515 K.⁸ In the meantime, radicals have also been the focus of research in organic electric conductors.⁹ While organic compounds are generally electric insulators, some radicals in charge transfer (CT) complexes achieved metallic conductivities^{10,11} and even superconductivities.^{12,13} (TTF)(TCNQ) (where TTF and TCNQ are tetrathiafulvalene and tetracyanoquinodimethane, respectively; Figure 1-1-3a) is a typical metallic conductor found in 1973,¹¹ and CT in the crystals forms radical cations and anions with the formal charge of (TTF^{+0.59})(TCNQ^{-0.59}). The donor (TTF) and the acceptor (TCNQ) have their own 1D columns independently in the crystals, which work as electron conducting pathways (Figure 1-1-3b)¹⁴. Following studies on one-dimensional metallic conductors, superconductivities were found in the CT complexes using TTF analogues, TMTSF¹² and BEDT-TTF^{13,15} (Figure 1-1-3b). These crystals have layer structures where donor molecules align in parallel and are regarded as quasi one- or two-dimensional conductors (Figure 1-1-3cd). Besides these magnetic and electric properties, nitroxyl radicals such as TEMPO derivatives are utilized as oxidation catalysts in chemical reactions. For example, primary alcohols are selectively oxidized into aldehydes in the presence of sodium hypochlorite or iodobenzene diacetate (Figure 1-1-4a).¹⁶ Catalytic photoreducing reactions by organic radicals were also recently achieved with an acridine radical (Figure 1-1-4b).¹⁷ Stable radicals have been extensively studied also in other fields and been applied to spin probe,^{2,18} rechargeable battery electrode,^{2,19} organic memory device,²⁰ and so on.

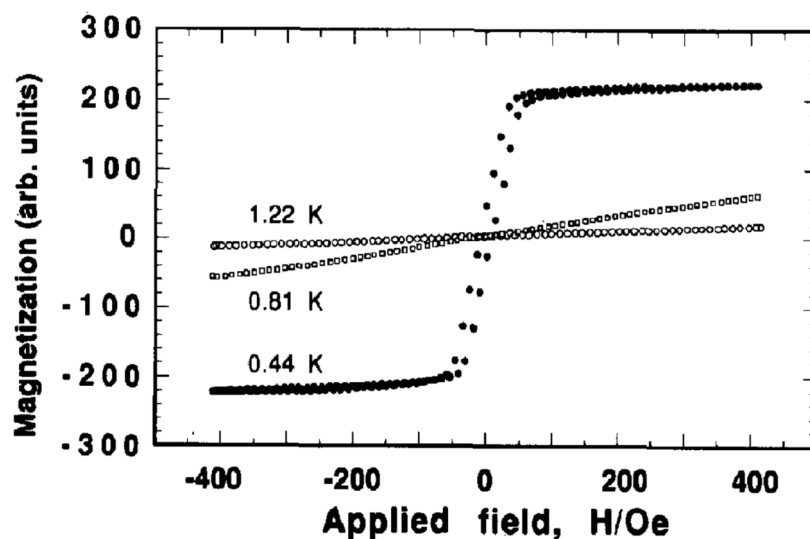


Figure 1-1-2. The magnetization curves of β -phase single crystal of *p*-NPNN above and below a Curie temperature, $T_c = 0.60$ K. (Reprinted with permission from ref. 6. Copyright 1991 Elsevier B.V.)

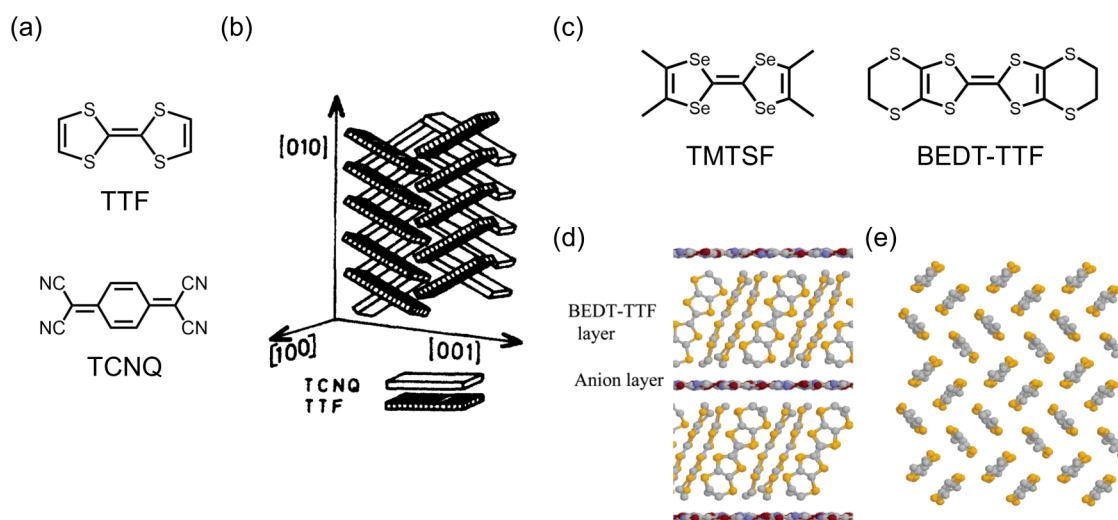
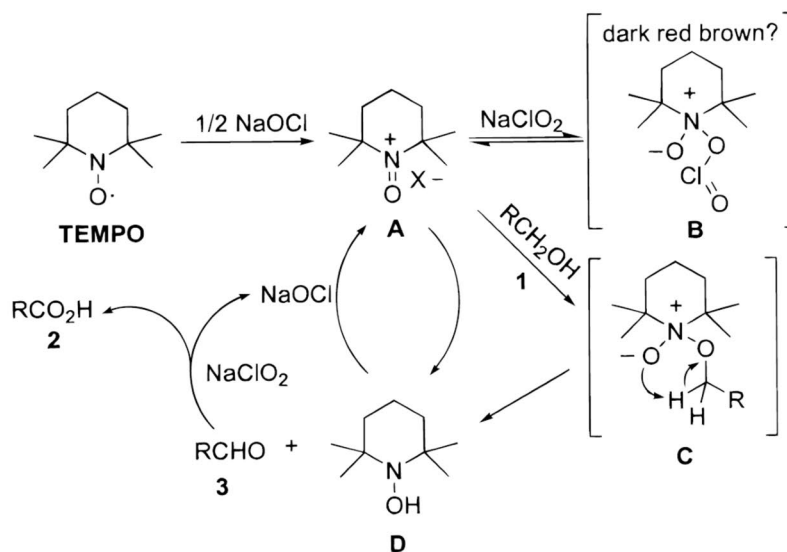


Figure 1-1-3. Electric-conducting organic radicals. (a) Chemical structures of TTF and TCNQ. (b) Schematic view of crystal structure of (TTF)(TCNQ). (c) Chemical structures of TMTSF and BEDT-TTF. (d) Crystal structure of κ -(BEDT-TTF) $_2$ X. (e) Arrangement of BEDT-TTF in the conducting layer. ((b) Reprinted with permission from ref. 14. Copyright 1977 by the American Physical Society. (d,e) Reprinted with permission from ref. 15. Copyright 2004 American Chemical Society.)

(a)



(b)

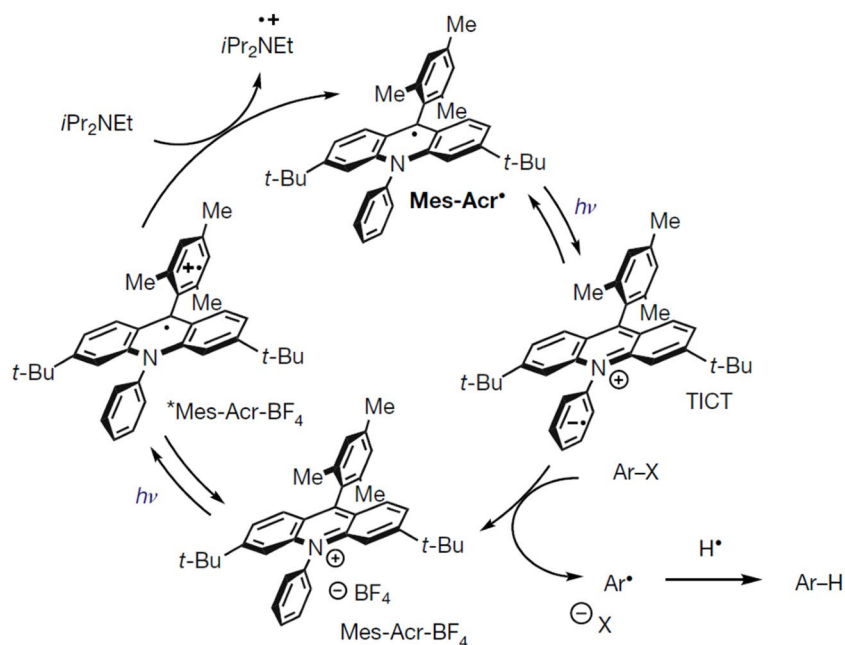


Figure 1-1-4. Catalytic reactions utilizing organic radicals. (a) Catalytic cycle for the TEMPO/NaOCl-catalyzed oxidation and (b) proposed scheme for reductive dehalogenation of aryl halides by acridine radical photoredox catalysis. ((a) Reprinted with permission from ref. 16. Copyright 1999 American Chemical Society. (b) Reprinted with permission from ref. 17. Copyright 2020 Springer Nature Limited.)

1-2 Luminescent organic radicals

1-2-1 Luminescence of organic radicals

Luminescent organic molecules have been developed for a wide-ranging research interests in scientific and engineering applications, including organic light-emitting diodes (OLEDs), bioimaging, and chemosensors. Several types of emission mechanisms, such as fluorescence from singlet excited states,²¹ phosphorescence based on triplet-singlet transitions,²² and thermally activated delayed fluorescence,^{23,24} have been studied to yield the desired photochemical and photophysical properties.

In contrast with conventional closed-shell molecules with singlet ground states organic radicals have recently been attracting much attention as a new class of luminescent materials.²⁵⁻³⁷ Although organic radicals have long been recognized as non-luminescent molecules acting as quenchers of luminophores, some radicals were reported to display the luminescence based on the transition from doublet lowest excited states (D_1) to doublet ground states (D_0). Owing to their unusual electronic structures, radicals show unique characteristics such as long emission wavelengths without extended π -conjugation³⁸ and the absence of the heavy atom effect. A particularly important property is the high internal electron-photon conversion efficiency of up to 100% in OLEDs,^{27,39,40} which has been experimentally achieved recently by the groups of F. Li and R. Friend.²⁸ While conventional closed-shell luminescence molecules suffer from quenching via the triplet excited state (T_1), which is statistically generated with the singlet excited state (S_1) in a 3:1 ratio, organic radicals can avoid this problem because of the lack of excited states with other spin multiplicities between D_1 and D_0 and the spin-allowed D_1 - D_0 transitions (Figure 1-2-1).²⁷

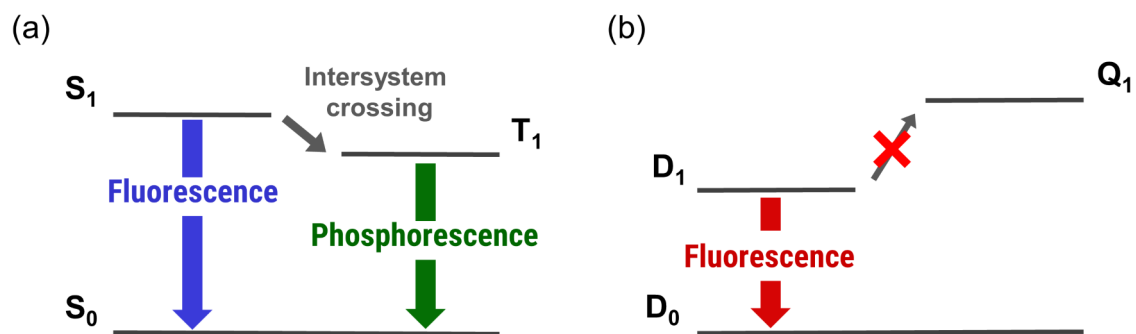


Figure 1-2-1. Emission processes of the organic molecules. (a) Closed-shell molecules and (b) open-shell doublet molecules. In (b), the lowest quartet excited state (Q_1) has much higher energy than D_1 .

1-2-2 Polychlorinated triphenylmethyl radical

Luminescence properties of organic radicals have been the focus of research in recent years; nevertheless they have been investigated much less than those of closed-shell molecules. This is mainly because of limited examples of luminescent organic radicals and their low photostability. Following studies on the luminescence properties of in-situ-generated unstable diarylmethyl or triarylmethyl radicals,⁴¹⁻⁴³ tris(2,4,6-trichlorophenyl)methyl radical (TTM) and polychlorinated triphenylmethyl radical (PTM) (Figure 1-2-2ab) have been developed as luminescent radicals.^{44,45} While these radicals are stable under ambient conditions, they undergo efficient photolysis reactions and decompose into non-luminescent species (Figure 1-2-2c).^{46,47} Therefore, improving the photostability of luminescent radicals is a critical issue for developing photofunctions of radicals.

Donor-acceptor type molecules utilizing TTM or PTM as the acceptor moieties have also been studied (Figure 1-2-3). Although emission quantum yields (ϕ_{em}) of TTM and PTM were low (~ 0.02), high ϕ_{em} values were reported in carbazole-bound TTM with ϕ_{em} of 0.64 in cyclohexane by L. Juliá *et al.*^{25,48,49} and triarylamine-bound PTM with ϕ_{em} of 0.38 in cyclohexane by C. Lambert *et al.*^{26,50,51} These luminescent radical-based donor-acceptor type molecules have been utilized as fluorophores of OLED very recently^{28,39,40} (Figure 1-2-4) and further studies realized ϕ_{em} of more than 90% in CHCl_3 .⁵² Noteworthy, a recent study reported that these radicals showed great improvements in their photostability compared with those of TTM or PTM.⁵²

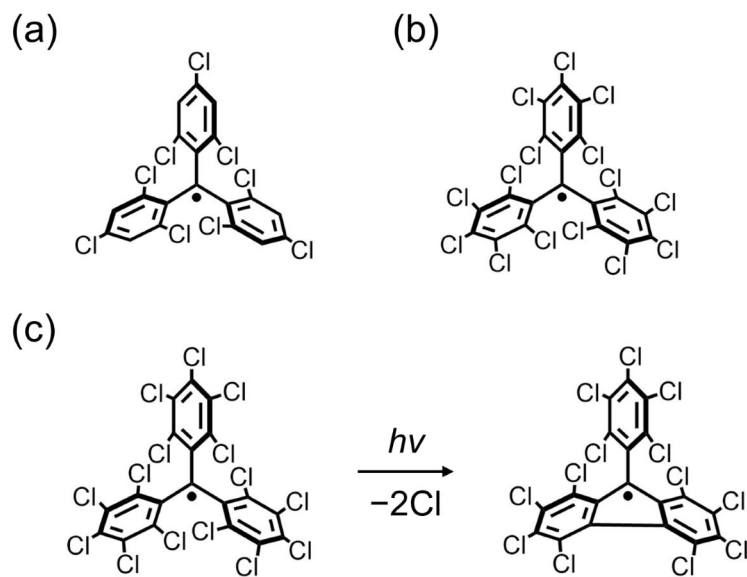


Figure 1-2-2. Molecular structures and photolysis reaction of polychlorinated triphenylmethyl radical. Molecular structures of (a) TTM and (b) PTM. (c) Photolysis reaction of PTM radical.

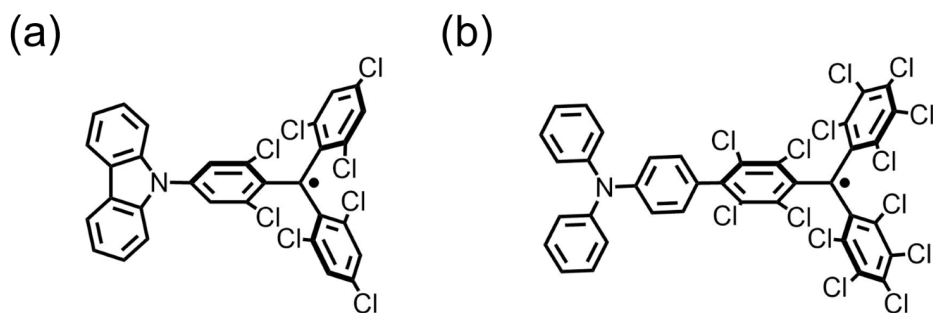


Figure 1-2-3. Molecular structures of donor-acceptor type radical molecules. (a) Carbazole-bound TTM and (b) triarylamine-bound PTM.

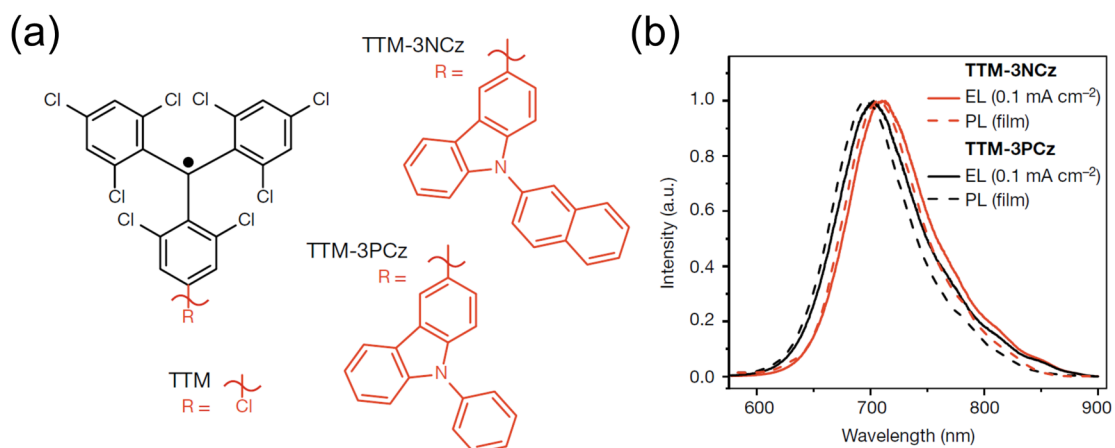


Figure 1-2-4. Electroluminescence of organic radicals in OLEDs. (a) Molecular structures of TTM, TTM-3NCz and TTM-3PCz. (b) Electroluminescence (solid lines) and photoluminescence (dotted lines) spectra for TTM-3NCz (red) and TTM-3PCz (black). (Reprinted with permission from ref. 28. Copyright 2018 Springer Nature Limited.)

1-2-3 Pyridyl-substituted triarylmethyl radicals

Another molecular strategy to improve the chemical stability of radicals upon photoirradiation is the introduction of nitrogen atoms to the TTM skeleton. T. Kusamoto and H. Nishihara *et al.* have prepared a novel luminescent organic radical, (3,5-dichloro-4-pyridyl)bis(2,4,6-trichlorophenyl)methyl radical (PyBTM; Figures 1-2-5a and 1-2-6).²⁷ PyBTM showed the luminescence with ϕ_{em} of 0.01–0.03 in organic solution and ϕ_{em} of 0.26 in poly(methyl methacrylate) film at room temperature. Its half-life ($t_{1/2}$) under photoirradiation was 115 times longer than that of TTM. This great high photostability of PyBTM has enabled us to explore photofunctions of radicals.

Additionally, the pyridyl nitrogen atom of PyBTM can act as not only a chemical stimulus-responsive site^{27,53} but a coordination site to metal ions.⁵⁴⁻⁵⁹ The photofunctions of metal complexes with ligated luminescent radicals have been firstly investigated by using PyBTM derivatives as a ligand (Figure 1-2-5b). These studies have revealed increased photostability and ϕ_{em} upon coordination to metal ions⁵⁴⁻⁵⁶ and the absence of heavy atom effects in doublet emitters.⁵⁷

Further improvement on photostability of organic radicals has been achieved by the introduction of the second pyridyl ring into the TTM framework. In the master course I have newly prepared bis(3,5-dichloro-4-pyridyl)(2,4,6-trichlorophenyl)methyl radical (bisPyTM; Figure 1-2-5c) and investigated its luminescence properties.⁶⁰ bisPyTM displayed the emission with ϕ_{em} of 0.009 in CH₂Cl₂ solution and up to 71 times longer $t_{1/2}$ than PyBTM. The luminescence of bisPyTM in the crystalline state were also observed at 77 K as the first example of definite solid-state emission of radicals. Moreover, two nitrogen atoms of bisPyTM enable a two-stage response to chemical stimuli and forming a 1D coordination polymer through coordination to Cu^{II}(hfac)₂ (where hfac is hexafluoroacetylacetonato; Figure 1-2-5d).⁶¹

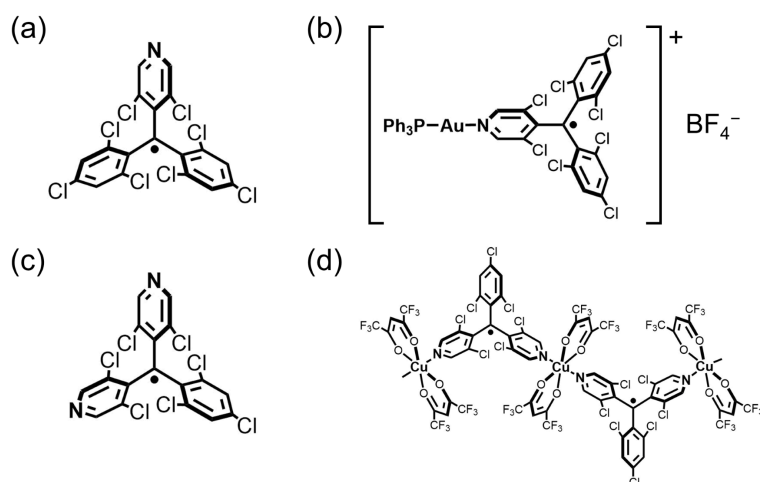


Figure 1-2-5. Molecular structures of pyridyl-substituted radicals and their metal complexes. (a) PyBTM, (b) $[\text{Au}^{\text{I}}(\text{PyBTM})\text{PPh}_3]\text{BF}_4$, (c) bisPyTM, and (d) $[\text{Cu}^{\text{II}}(\text{hfac})_2(\text{bisPyTM})]_n$.

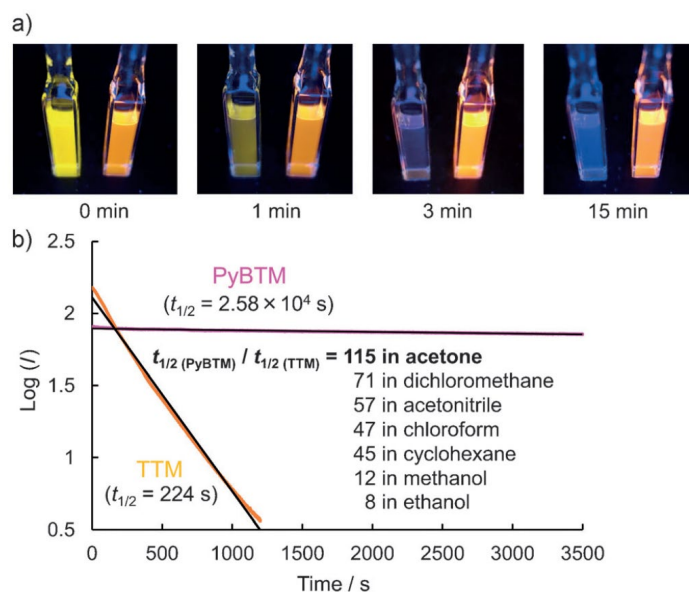


Figure 1-2-6. Photostability of PyBTM and TTM radicals. (a) Photographs of TTM and PyBTM solutions (left and right cuvette in each image, respectively; 2.5×10^{-4} M) in acetone under irradiation with UV light at $\lambda = 370$ nm. (b) Plots showing the emission decays of PyBTM and TTM in acetone under continuous excitation with UV light at $\lambda = 370$ nm. (Reprinted with permission from ref. 27. Copyright 2014 John Wiley & Sons, Inc.)

1-3 Aim of this research

As described Section 1-1-2, organic radicals have been providing unique electric and magnetic properties, which are difficult to achieve with closed-shell molecules. These properties were correlated with their spin states and the spin-spin interactions play key roles in the phenomena. Therefore, controlling a manner or a degree of assembly of radical molecules, which regulates the spin-spin interactions, would be a promising strategy to obtain spin-correlated properties unique to radicals.

The aim of my research is to establish the novel luminescence properties of organic radicals, where spin and luminescence were correlated. Such properties of organic radicals have never been accomplished despite their prospect as an approach to yield novel photofunctions unique to radicals. To achieve the purpose, in this research, I prepared assembled (aggregated) radicals and investigated their luminescence properties (Figure 1-3-1). Pyridyl-substituted luminescent radicals were employed as materials for the investigations to avoid the problem of photodecomposition.

First, I prepared a new organic radical with three pyridyl rings, tris(3,5-dichloro-4-pyridyl)methyl radical (trisPyM) and its 2D coordination polymers (CPs) to expand the scope of luminescent radical materials and manners of assembly of radicals (Chapter 2). Both trisPyM and its 2D CP with $\text{Zn}^{\text{II}}(\text{hfac})_2$ were luminescent and the latter was the first example of luminescent 2D radical-based CPs. Investigations on the magnetic properties of the 2D CP with $\text{Cu}^{\text{II}}(\text{hfac})_2$ and the construction of the 2D CP with $\text{Zn}^{\text{II}}(\text{TPP})$ (where TPP is tetraphenylporphyrinato) were also performed.

Then I took on the challenge to develop a photofunction based on interplay between spin and luminescence. Here I focused on magnetic field effects (MFEs) on the luminescence, namely magnetoluminescence. Magnetic-field-sensitive emissions of aggregated PyBTM in host molecular crystals were observed as the first example of magnetoluminescence of radicals,⁶² and its mechanism was investigated via the time-resolved emission measurements and the quantum mechanical simulations (Chapter 3). The general nature of magnetoluminescence in radicals was confirmed by the observation of the MFEs on luminescence in PyBTM- $\text{Zn}^{\text{II}}(\text{hfac})_2$ complexes doped into matrices (Chapter 4).⁶³ Moreover, an alternate methodology to achieve magnetoluminescence without doping into matrices, constructing radical-based CPs,

was demonstrated (Chapter 5). These findings establish magnetoluminescence as the first example of spin-luminescence correlated properties of radicals.

Radical × **Assembly** × Luminescence = **Magnetoluminescence**

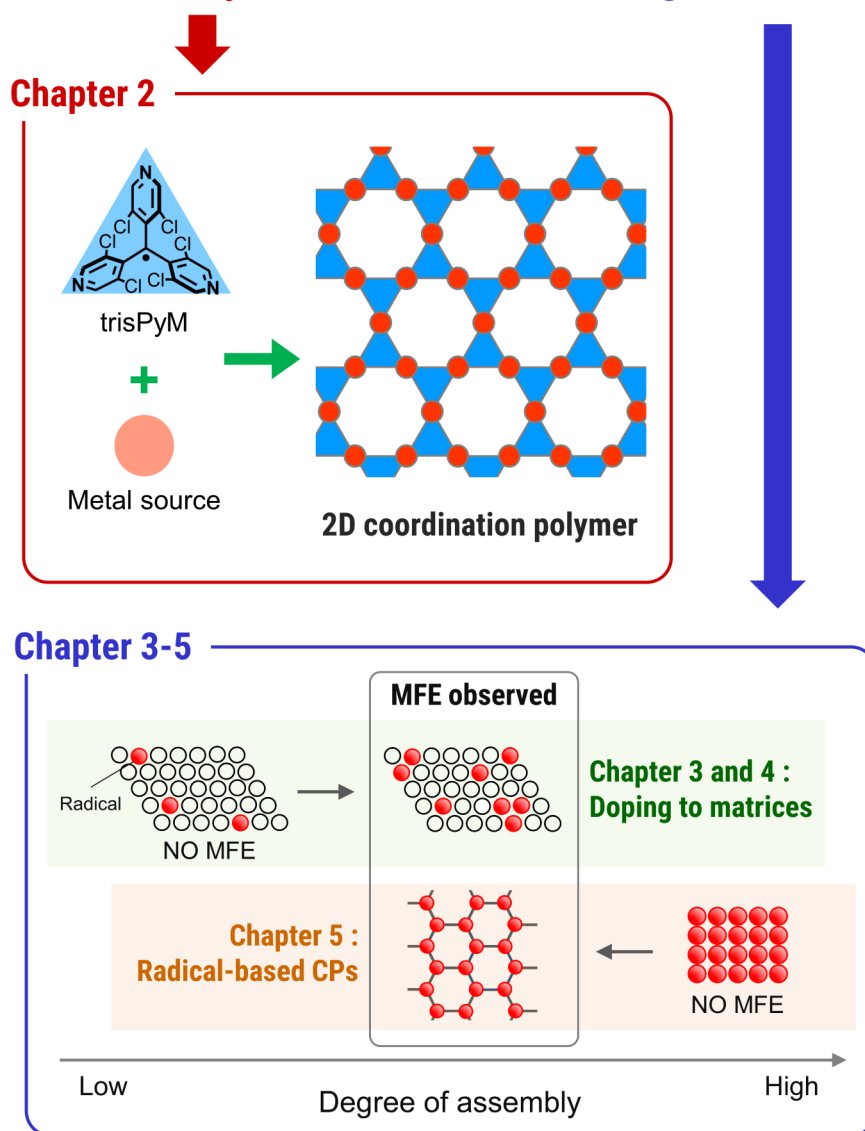


Figure 1-3-1. Conceptual scheme showing the studies in this thesis.

1-4 References

- [1] M. Gomberg, *J. Am. Chem. Soc.*, 1900, **22**, 757–771.
- [2] R. G. Hicks, *Stable Radicals: Fundamentals and Applied Aspects of Odd-Electron Compounds*, Wiley, Chichester, 2010.
- [3] R. G. Hicks, *Org. Biomol. Chem.*, 2007, **5**, 1321–1338.
- [4] D. Shimizu and A. Osuka, *Chem. Sci.*, 2018, **9**, 1408–1423.
- [5] M. Kinoshita *Jpn. J. Appl. Phys.*, 1994, **33**, 5718–5733
- [6] M. Tamura, Y. Nakazawa, D. Shiomi, K. Nozawa, Y. Hosokoshi, M. Ishikawa, M. Takahashi and M. Kinoshita, *Chem. Phys. Lett.*, 1991, **186**, 401–404.
- [7] H. Phan, T. S. Herng, D. Wang, X. Li, W. Zeng, J. Ding, K. P. Loh, A. T. Shen Wee and J. Wu, *Chem*, 2019, **5**, 1223–1234.
- [8] P. Perlepe, I. Oyarzabal, A. Mailman, M. Yquel, M. Platunov, I. Dovgaliuk, M. Rouzières, P. Négrier, D. Mondieig, E. A. Suturina, M. A. Dourges, S. Bonhommeau, R. A. Musgrave, K. S. Pedersen, D. Chernyshov, F. Wilhelm, A. Rogalev, C. Mathonière and R. Clérac, *Science*, 2020, **370**, 587–592.
- [9] T. Mori and T. Kawamoto, *Annu. Rep. Prog. Chem., Sect. C: Phys. Chem.*, 2007, **103**, 134–172.
- [10] A. J. Epstein, S. Etemad, A. F. Garito and A. J. Heeger, *Phys. Rev. B*, 1972, **5**, 952–977.
- [11] J. Ferraris, D. O. Cowan, V. Walatka and J. H. Perlstein, *J. Am. Chem. Soc.*, 1973, **95**, 948–949.
- [12] D. Jérôme, A. Mazaud, M. Ribault and K. Bechgaard, *J. Physique Lett.*, 1980, **41**, 95–98.
- [13] E. B. Yagubskii, I. F. Schegolev, V. N. Laukhin, P. A. Kononovich, M. V. Karatsovnik, A. V. Zvarykina and L. I. Buravov, *JETP Lett.*, 1984, **39**, 12–16.
- [14] S. K. Khanna, J. P. Pouget, R. Comes, A. F. Garito and A. J. Heeger, *Phys. Rev. B*, 1977, **16**, 1468–1479.
- [15] K. Miyagawa, K. Kanoda and A. Kawamoto, *Chem. Rev.*, 2004, **104**, 5635–5653.
- [16] M. Zhao, J. Li, E. Mano, Z. Song, D. M. Tschäen, E. J. J. Grabowski and P. J. Reider, *J. Org. Chem.*, 1999, **64**, 2564–2566.
- [17] I. A. MacKenzie, L. Wang, N. P. R. Onuska, O. F. Williams, K. Begam, A. M. Moran, B. D. Dunietz and D. A. Nicewicz, *Nature*, 2020, **580**, 76–80.

- [18] T. J. Stone, T. Buckman, P. L. Nordio and H. M. McConnell, *Proc. Nat. Acsd. Sci. USA*, 1965, **54**, 1010–1017
- [19] H. Nishide and K. Oyaizu, *Science*, 2008, **319**, 737–738.
- [20] Y. Yonekuta, K. Susuki, K. Oyaizu, K. Honda and H. Nishide, *J. Am. Chem. Soc.* 2007, **129**, 14128–14129.
- [21] C. W. Tang and S. A. Vanslyke, *Appl. Phys. Lett.*, 1987, **51**, 913–915.
- [22] M. A. Baldo, D. F. O'brien, Y. You, A. Shoustikov, S. Sibley, M. E. Thompson and S. R. Forrest, *Nature*, 1998, **395**, 151–154.
- [23] A. Endo, M. Ogasawara, A. Takahashi, D. Yokoyama, Y. Kato and C. Adachi, *Adv. Mater.*, 2009, **21**, 4802–4806.
- [24] H. Uoyama, K. Goushi, K. Shizu, H. Nomura and C. Adachi, *Nature*, 2012, **492**, 234–238.
- [25] L. Fajari, R. Papoular, M. Reig, E. Brillas, J. L. Jorda, O. Vallcorba, J. Rius, D. Velasco and L. Juliá, *J. Org. Chem.*, 2014, **79**, 1771–1777.
- [26] A. Heckmann, S. Du, J. Pauli, M. Margraf, J. Ko, D. Stich, C. Lambert, I. Fischer and U. Resch-genger, *J. Phys. Chem. C*, 2009, **113**, 20958–20966.
- [27] Y. Hattori, T. Kusamoto and H. Nishihara, *Angew. Chem. Int. Ed.*, 2014, **53**, 11845–11848.
- [28] X. Ai, E. W. Evans, S. Dong, A. J. Gillett, H. Guo, Y. Chen, T. J. H. Hele, R. H. Friend and F. Li, *Nature*, 2018, **563**, 536–540.
- [29] H. Guo, Q. Peng, X. K. Chen, Q. Gu, S. Dong, E. W. Evans, A. J. Gillett, X. Ai, M. Zhang, D. Credgington, V. Coropceanu, R. H. Friend, J. L. Brédas and F. Li, *Nat. Mater.*, 2019, **18**, 977–984.
- [30] Y. Beldjoudi, M. Nascimento, Y. J. Cho, H. Yu, H. Aziz, D. Tonouchi, K. Eguchi, M. M. Matsushita, K. Awaga, I. O. Osorio-roman, C. P. Constantinides and J. M. Rawson, *J. Am. Chem. Soc.*, 2018, **140**, 6260–6270.
- [31] Y. Beldjoudi, I. Osorio-Román, M. A. Nascimento and J. M. Rawson, *J. Mater. Chem. C*, 2017, **5**, 2794–2799.
- [32] P. Mayorga Burrezo, V. G. Jiménez, D. Blasi, I. Ratera, A. G. Campaña and J. Veciana, *Angew. Chem. Int. Ed.*, 2019, **58**, 16282–16288.
- [33] P. Mayorga-Burrezo, V. G. Jiménez, D. Blasi, T. Parella, I. Ratera, A. G. Campaña and J. Veciana, *Chem. –Eur. J.*, 2020, **26**, 3776–3781.
- [34] D. Blasi, D. M. Nikolaidou, F. Terenziani, I. Ratera and J. Veciana, *Phys. Chem. Chem. Phys.*, 2017, **19**, 9313–9319.

- [35] E. V. Tretyakov, V. F. Plyusnin, A. O. Suvorova, S. V. Larionov, S. A. Popov, O. V. Antonova, E. M. Zueva, D. V. Stass, A. S. Bogomyakov, G. V. Romanenko and V. I. Ovcharenko, *J. Lumin.*, 2014, **148**, 33–38.
- [36] K. An, G. Xie, S. Gong, Z. Chen, X. Zhou, F. Ni and C. Yang, *Sci. China Chem.*, 2020, **63**, 1214–1220.
- [37] Y. Teki, *Chem. –Eur. J.*, 2020, **26**, 980–996.
- [38] H. Namai, H. Ikeda, Y. Hoshi, N. Kato, Y. Morishita and K. Mizuno, *J. Am. Chem. Soc.*, 2007, **129**, 9032–9036.
- [39] Q. Peng, A. Obolda, M. Zhang and F. Li, *Angew. Chem. Int. Ed.*, 2015, **54**, 7091–7095.
- [40] A. Obolda, X. Ai, M. Zhang and F. Li, *ACS Appl. Mater. Interfaces*, 2016, **8**, 35472–35478.
- [41] M. Sakamoto, X. Cai, M. Hara, S. Tojo, M. Fujitsuka and T. Majima, *J. Am. Chem. Soc.*, 2005, **127**, 3702–3703.
- [42] J. C. Scaiano, L. J. Johnston, W. G. McGimpsey and D. Weir, *Acc. Chem. Res.*, 1988, **21**, 22–29.
- [43] D. Meisel, P. K. Das, G. L. Hug, K. Bhattacharyya and R. W. Fessenden, *J. Am. Chem. Soc.*, 1986, **108**, 4706–4710.
- [44] M. Ballester, J. Riera, J. Castatier, C. Badfa and J. M. Monsó, *J. Am. Chem. Soc.*, 1971, **93**, 2215–2225.
- [45] O. Armet, J. Veciana, C. Rovira, J. Riera, J. Castaner, E. Molins, J. Rius, C. Miravittles, S. Olivella and J. Brichfeus, *J. Phys. Chem.*, 1987, **91**, 5608–5616.
- [46] M. A. Fox, E. Gaillard and C. Chen, *J. Am. Chem. Soc.*, 1987, **109**, 7088–7094.
- [47] S. R. Ruberu and M. A. Fox, *J. Phys. Chem.*, 1993, **97**, 143–149.
- [48] V. Gamero, D. Velasco, S. Latorre, F. López-Calahorra, E. Brillas and L. Juliá, *Tetrahedron Lett.*, 2006, **47**, 2305–2309.
- [49] D. Velasco, S. Castellanos, M. López, F. López-Calahorra, E. Brillas and L. Juliá, *J. Org. Chem.*, 2007, **72**, 7523–7532.
- [50] A. Heckmann, C. Lambert, M. Goebel and R. Wortmann, *Angew. Chem. Int. Ed.*, 2004, **43**, 5851–5856.
- [51] A. Heckmann and C. Lambert, *J. Am. Chem. Soc.*, 2007, **129**, 5515–5527.
- [52] A. Abdurahman, T. J. H. Hele, Q. Gu, J. Zhang, Q. Peng, M. Zhang, R. H. Friend, F. Li and E. W. Evans, *Nat. Mater.*, 2020, **19**, 1224–1229.

- [53] T. Kusamoto, S. Kimura, Y. Ogino, C. Ohde and H. Nishihara, *Chem. –Eur. J.*, 2016, **22**, 17725–17733.
- [54] Y. Hattori, T. Kusamoto and H. Nishihara, *Angew. Chem. Int. Ed.*, 2015, **54**, 3731–3734.
- [55] Y. Hattori, T. Kusamoto, T. Sato and H. Nishihara, *Chem. Commun.*, 2016, **52**, 13393–13396
- [56] Y. Ogino, T. Kusamoto, Y. Hattori, M. Shimada, M. Tsuchiya, Y. Yamanoi, E. Nishibori, K. Sugimoto and H. Nishihara, *Inorg. Chem.*, 2017, **56**, 3909–3915.
- [57] Y. Hattori, S. Kimura, T. Kusamoto, H. Maeda and H. Nishihara, *Chem. Commun.*, 2018, **54**, 615–618.
- [58] T. Kusamoto, Y. Hattori, A. Tanushi and H. Nishihara, *Inorg. Chem.*, 2015, **54**, 4186–4188.
- [59] T. Kusamoto, S. Kimura and H. Nishihara, *Chem. Lett.*, 2016, **45**, 1057–1059.
- [60] S. Kimura, A. Tanushi, T. Kusamoto, S. Kochi, T. Sato, H. Nishihara, *Chem. Sci.*, 2018, **9**, 1996–2007.
- [61] S. Kimura, H. Uchida, T. Kusamoto and H. Nishihara, *Dalton Trans.*, 2019, **48**, 7090–7093.
- [62] S. Kimura, T. Kusamoto, S. Kimura, K. Kato, Y. Teki and H. Nishihara, *Angew. Chem. Int. Ed.*, 2018, **57**, 12711–12715.
- [63] S. Kimura, S. Kimura, H. Nishihara and T. Kusamoto, *Chem. Commun.*, 2020, **56**, 11195–11198.

Chapter 2

Open-shell 2D coordination polymers based on a tris-pyridyl-substituted triarylmethyl radical

本章については、5 年以内に雑誌等で刊行予定のため、非公開。

Chapter 3

Magnetoluminescence of PyBTM doped in matrices

3-1 Introduction

3-1-1 Magnetic field effect

Magnetic fields modulate the behaviors of electrons. Magnetic field effects (MFEs) have attracted attention as an effective tool for studying and controlling the spin dynamics in molecules and chemical reactions.¹⁻¹⁵ This technique has been utilized in optical imaging¹ or optoelectronic devices.^{2,3}

MFEs on molecular luminescence have been extensively studied to understand the excited-state characteristics and spin dynamics of luminescent molecules and several mechanisms have been proposed. The most studied system involves intersystem crossing (ISC) between singlet and triplet radical pairs (RPs) generated upon electron transfer in photo- or electro-excited states.⁵⁻¹⁰ Magnetic field influences on the rate of ISC between energetically comparable excited states with different spin multiplicities (singlet and triplet excited states, for example) by processes called Δg , hyperfine coupling (hfc), and relaxation mechanisms. These modulations dynamically change the distributions of spin states (*i.e.*, spin statistics) in the excited states and the yields of emissive recombined species, resulting in magnetic field-sensitive luminescence properties. MFEs have also been observed in other processes involving changes in the spin multiplicities in the excited states, such as triplet–triplet annihilation. These MFEs have been studied for crystalline compounds,^{11,12} amorphous compounds,¹³ and solutions.^{14,15}

3-1-2 Magnetoluminescence of radicals

As described in Chapter 1, an important challenge that remains in the research of luminescent radicals is to develop photofunctions based on the interplay between luminescence and spin, such as magnetic-field-sensitive luminescence, namely magnetoluminescence. There are no reports of the apparent magnetoluminescence from stable radicals, and F. Li and co-workers have shown the absence of MFE on electroluminescence at room temperature for the fields of smaller than 200 mT.¹⁶

In this study, I focused on aggregated radicals to realize the MFE on luminescence of organic radicals. While monoradicals that are isolated or well-dispersed similarly to their solution state cannot interact with each other and their spin multiplicities are always doublet, aggregated radicals could form radical pairs and possess different spin multiplicities through intermolecular spin-spin interactions (Figure 3-1-1). From this point of view, I prepared PyBTM-doped¹⁷ αH -PyBTM crystals^{18,19} (**Py_R**, where R indicates the concentration (wt%) of PyBTM in the crystal; Figure 3-1-2) as aggregated radicals and investigated their luminescence properties under magnetic fields.²⁰ αH -PyBTM is the precursor of PyBTM and a closed-shell molecule. PyBTM is expected to be randomly dispersed and fixed in host crystals owing to their similar molecular sizes and structures. This rigid environment enables to not only suppress the molecular vibrations that cause the loss of emission efficiency but also control the degree of aggregation by changing the dopant concentration. Two notable findings from this chapter are as follows: (1) the **Py_0.05** exhibited luminescence with an excellent absolute emission quantum yield (ϕ_{em}) of 0.89 at room temperature; (2) **Py_4**, **Py_10**, and **Py_22** showed drastic changes in their emission spectra at 4.2 K under a magnetic field of up to 18 T. This is the first observation of magnetoluminescence in organic radicals; (3) the mechanism and main factors of the MFE in **Py_R** were determined by time-resolved luminescence measurements and quantum simulations; the magnetic-field-sensitive spin sublevel population of aggregated radicals in the ground states was the key factor governing the MFE.

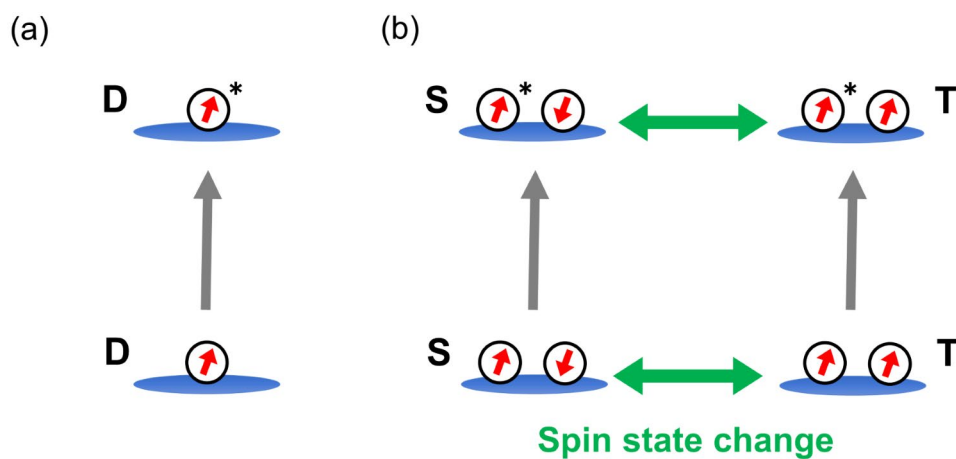


Figure 3-1-1. Schematic images of spin multiplicities. (a) isolated and (b) aggregated monoradicals.

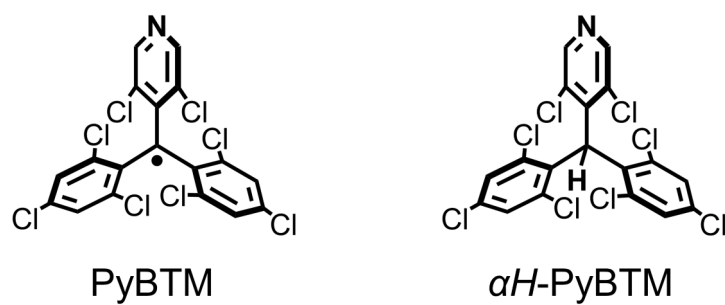


Figure 3-1-2. Molecular structures of PyBTM and αH -PyBTM.

3-2 Experimental section

3-2-1 Materials

All chemicals were reagent grade and purchased commercially. Water was purified using AUTOPURE WD500 (Yamato Scientific Co., Ltd.). Dichloromethane (CH_2Cl_2), diethyl ether (Et_2O), hexane and tetrahydrofuran (THF) used for syntheses were purified through organic solvent purifier (Nikko Hansen Co., Ltd.). PyBTM, αH -PyBTM, bisPyTM, and αH -bisPyTM were prepared according to procedures reported in the literatures.^{17,21}

3-2-2 Instruments and experimental methods

Instrumentation

UV-vis-NIR absorption spectra were recorded with a JASCO V570 spectrophotometer. Steady-state emission spectra at room temperature were measured with JASCO FP8600 spectrometers. Sample solutions were bubbled with argon before measurement. Absolute photoluminescence quantum yields were measured with a Hamamatsu Photonics C9920-02G. Fluorescence lifetime measurements were performed using a Hamamatsu Photonics Quantaaurus-Tau C11367-02.

The data for single crystal X-ray diffraction analysis were collected at 113 K on a Rigaku AFC10 diffractometer with a Rigaku Saturn CCD system equipped with a rotating-anode X-ray generator that emitted graphite-monochromated Mo $K\alpha$ radiation (0.7107 Å). A suitable single crystal was mounted on a looped film (micromount) with liquid paraffin. An empirical absorption correction using equivalent reflections and Lorentzian polarization correction was performed with the program Crystal Clear 1.3.6. The structure was solved using SIR-92²² and the whole structure was refined against F^2 with SHELXL-97.²³ All non-hydrogen atoms were refined anisotropically. Hydrogen atoms were located at idealized positions and were refined using a riding model with fixed thermal parameters. Crystal structure data (CIF, CCDC 1838626) can be obtained free of charge from The Cambridge Crystallographic Data Centre.

Luminescence measurement under magnetic field

The system, which consists of ASAHI MAX-302 with a band-pass filter of 400 nm as a light source, a single grating spectrometer (HORIBA iHR550) and a multichannel CCD detector (Andor iDus DU401-BV), was used for the data in Figures 3-3-10, 3-3-13, and 3-3-20. For the other data, the system for luminescence measurement under magnetic field consists of a picosecond diode laser with the emission wavelength of 375 nm (Advanced Laser Diode Systems PIL037X) as a light source, a single grating spectrometer (Andor Kymera193i-B1), a multichannel CCD detector (Andor iDus DV420A-OE). Photon counting detector (MPD SPD-050-CTE) was operated with time-correlated single photon counting (TCSPC) technique. This optical measurement system is combined with a solenoid type superconducting magnet, which can generate up to 14.5, 16.5, or 18 T.²⁴ Optical fibers are used to lead a light from light sources to a sample at the center of the superconducting magnet and from the sample to the spectrometer. The details of the vicinity of a sample are shown in Figure 3-2-1. The light through the optical fiber is transformed to a parallel beam by the first convex lens. The light beam is focused down by the second convex lens to the sample, and emission from the sample hit the beam splitter and mirror. It transmits through the third convex lens, and is introduced to the spectrometer with a long-pass filter (500 nm) by another optical fiber. In this system, the measurement is carried out in the Faraday configuration, where the magnetic field is parallel to the light direction at a sample.

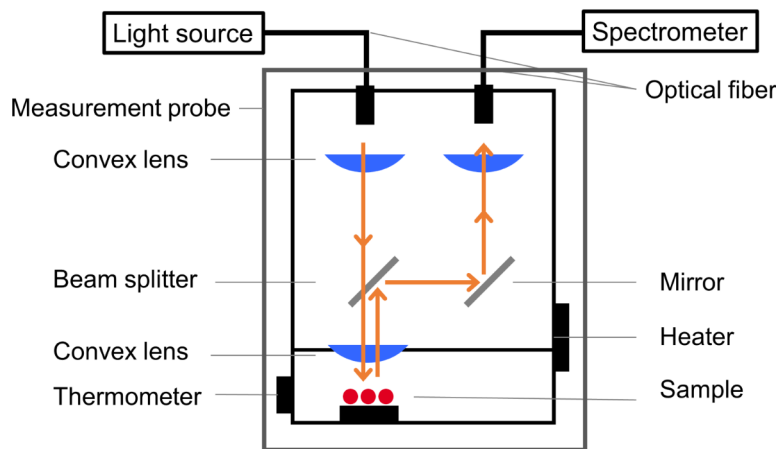


Figure 3-2-1. Schematic view of a sample room for the luminescence measurement under magnetic field.

Identification of doping concentration of **Py_R**

The doping concentration of **Py_R** was confirmed by measuring absorption spectrum of **Py_R** dissolved in CH₂Cl₂. Since the absorption spectra of PyBTM and αH -PyBTM have an isosbestic point at 289 nm (Figure 3-2-2) and ϵ of PyBTM at 289 and 370 nm in CH₂Cl₂ are 2644 and 25406 M⁻¹cm⁻¹, respectively, the doping concentration x is calculated as

$$\frac{25406}{2644} \times \frac{x}{100} = \frac{b}{a}$$

where a and b are the absorbance of **Py_R** at 289 and 370 nm, respectively.

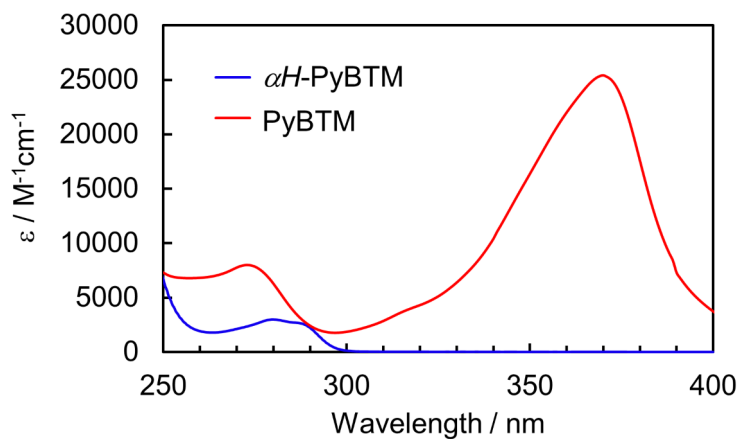


Figure 3-2-2. Absorption spectra of PyBTM and αH -PyBTM in CH₂Cl₂.

Estimation of the exchange interactions (J) between a PyBTM dimer

The intramolecular exchange interactions (J , where $H = -2J \sum \mathbf{S}_1 \cdot \mathbf{S}_2$) of PyBTM dimers in the ground states were estimated by analyzing the magnetic-field-dependence of amplitudes (*i.e.*, photon counts right after photoexcitation) of emission decays. The increase of the amplitude corresponds to the increase of the populations of the triplet close radical pair (close RP) shown later in Figure 3-3-24b, $^3(\text{R--R})^*$, by magnetic field. Because the populations of $^3(\text{R--R})^*$ were determined by the populations of the triplet PyBTM dimer in the ground states, the magnetic-field-dependence of the amplitudes ($I(B)$) in this system is given by

$$I(B) = A \left(1 - \frac{\exp(-J/k_B T)}{\exp(-J/k_B T) + \exp(J/k_B T) + \exp((J + g\mu_B B)/k_B T) + \exp((J - g\mu_B B)/k_B T)} + I_{RP} \right) \quad (\text{Eq. 3-2-1})$$

where A is proportionality factor; g is g value of PyBTM ($= 2.003$); μ_B is Bohr magneton; B is magnetic field strength; k_B is Boltzmann constant; I_{RP} is a constant derived from emission of RPs in Figure 3-3-24a (because both singlet and triplet RPs depicted in Figure 3-3-24a are emissive and the sum of populations of singlet and triplet RPs right after photoexcitation is independent of magnetic field, amplitudes contributed by RPs are constant.). Figure 3-2-3 shows magnetic field dependence of the amplitudes of **Py_10** and the fit based on Eq. 3-2-1, determining J/k_B as -4.8 K.

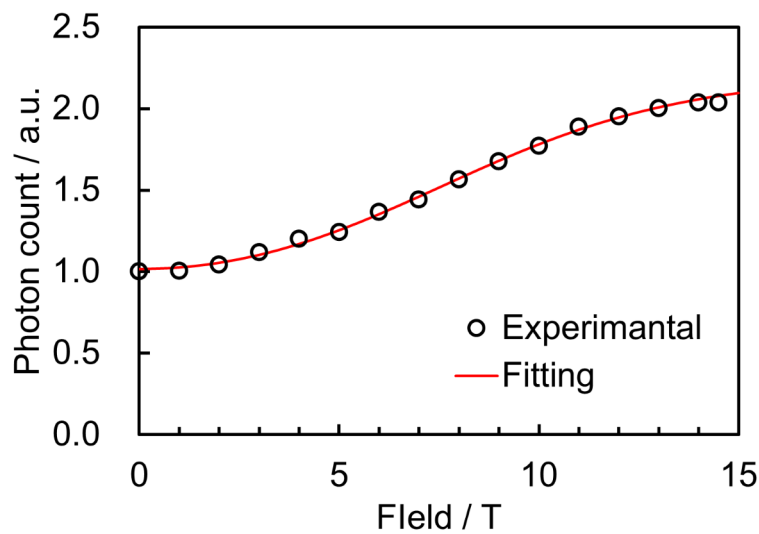


Figure 3-2-3. Magnetic-field-dependence of amplitudes of emission decays of **Py_10** and the fit using Eq. 3-2-1 with $T = 4.2$ K.

Quantum simulations of emission decays of **Py_10**

Emission decays of **Py_10** were simulated based on the kinetic models shown in Figure 3-3-24. The details of calculation methods for the rates of ISC and transitions and the parameters except kinetic constants and J of PyBTM dimers followed our previous work.²⁵ Stretched radiative rate constants, $k(t_n)$, were taken into account by employing the time-dependent transition rate ($k(t)$) given by

$$k(t_n) = \beta k_m (k_m t_n)^{\beta-1}$$

where k_m is the transition rate in the case of the stretch factor, $\beta = 1$ (uniform system).²⁶ To avoid infinite transition rate at $t = 0$, I used the transition rate $k(0) = \beta k_m (k_m t')^{\beta-1}$ with $t' = 0.1289$ ns.

Emission decays of Close RP were calculated by classical mechanical simulation (conventional rate equations) based on Figure 3-3-24b and monomer emission decays of **Py_10** were estimated as the totals of those of RP and Close RP. The monomer emission and excimer emission intensities were obtained by integrating the time-resolved emission from 0 to 696 ns and 0 to 3000 ns, respectively. “No excited-state MFE” in Figures 3-3-25c and 3-3-28 was calculated by classical mechanical simulation based on Figure 3-3-24 with the assumption that ISC between singlet (S) and triplet (T_0) RPs in the excited states does not occur. “No ground-state MFE” in Figures 3-3-25d and 3-3-28 was calculated by fixing the spin-sublevel populations of PyBTM dimer in the ground states as those at 0 T.

The values of parameters, k_{m1} , k_{m2} , β_1 , β_2 , and k_{Sex} were estimated by fitting with experimental emission decays by the least-square methods. I assumed that J is the same as that in Figure 3-3-24 in the fitting for computational reduction.

3-3 Results and Discussion

3-3-1 Preparation of **Py_R**

PyBTM-doped αH -PyBTM crystals at various concentrations (0.05 to 23 wt%) were prepared by co-crystallization. Both PyBTM and αH -PyBTM were dissolved in CH_2Cl_2 and the solvent was slowly evaporated for several days, affording **Py_R** (Figure 3-3-1). The radical concentration was controlled by changing the weight ratio of PyBTM and αH -PyBTM in the solution.

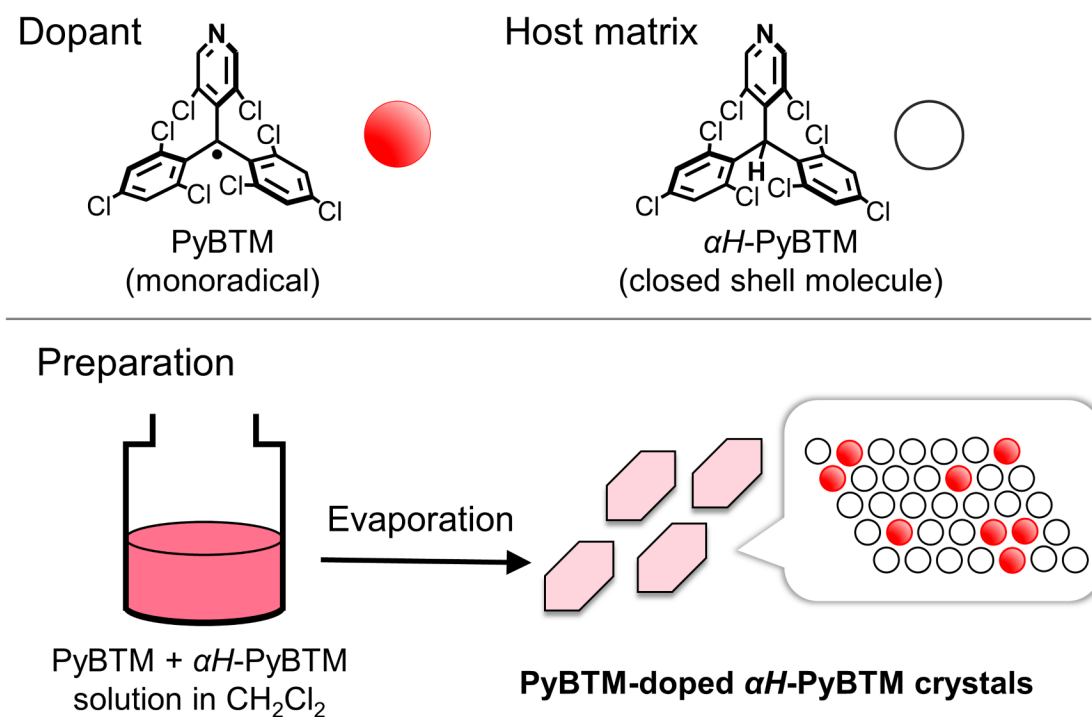


Figure 3-3-1. Schematic image of **Py_R** preparation.

Powder X-ray diffraction (PXRD) analysis was performed to investigate the effect of doping of PyBTM on the crystal structure of the host compound, αH -PyBTM (Figure 3-3-2). The PXRD patterns of **Py_0.90**, **Py_10**, and **Py_23** were similar to that of αH -PyBTM crystals and different from that of PyBTM crystals, suggesting that αH -PyBTM was randomly replaced with PyBTM without changing the crystal structure in this doping region. These behaviors were facilitated probably because of the similarity of the molecular structures of PyBTM and αH -PyBTM, including the bond angles around the central carbon atoms. Although the central carbon atoms of PyBTM and αH -PyBTM are sp^2 and sp^3 hybridized, respectively, the geometry around the central carbon atom of αH -PyBTM is slightly flattened with surrounded six Cl atoms; the C-C-C bond angles around the central carbon atom of αH -PyBTM were 113.9(5), 116.0(5), and 118.6(5) $^\circ$, respectively. The crystal structure and crystallographic data of αH -PyBTM revealed by a single-crystal XRD analysis is shown in Figure 3-3-3 and Table 3-3-1.

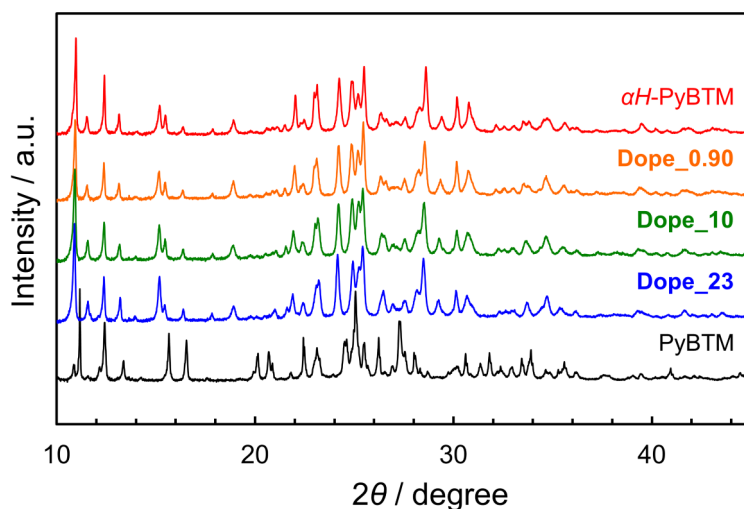


Figure 3-3-2. PXRD patterns of **Py_R** and PyBTM.

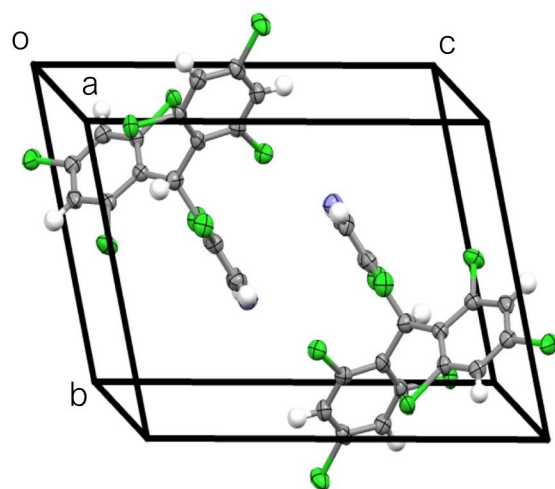


Figure 3-3-3. Packing structure of αH -PyBTM.

Table 3-3-1. Crystallographic data of αH -PyBTM

Empirical formula	C ₁₈ H ₇ Cl ₈ N
$F_w / \text{g mol}^{-1}$	520.88
Crystal system	Triclinic
Space group	$P\bar{1}$
Crystal size / mm	$0.15 \times 0.03 \times 0.02$
Temperature / K	113
$a / \text{\AA}$	8.294(3)
$b / \text{\AA}$	9.816(4)
$c / \text{\AA}$	13.421(5)
$\alpha / ^\circ$	77.841(15)
$\beta / ^\circ$	70.630(15)
$\gamma / ^\circ$	74.272(15)
$V / \text{\AA}^3$	983.4(6)
$\rho_{\text{calcd}} / \text{g cm}^{-3}$	1.759
$\lambda / \text{\AA}$	0.71070
μ / mm^{-1}	1.148
Reflection collected	7814
Independent reflections	4322
Parameters	244
R_{int}	0.0351
R_1^a	0.0719
wR_2^b	0.2117
GoF ^c	1.006

$$^a R_1 = \Sigma ||F^o| - |F^c|| / \Sigma |F^o| \quad (I > 2\sigma(I)). \quad ^b wR_2 = [\Sigma (w(F^{o2} - F^{c2})^2 / \Sigma w(F^{o2})^2)]^{1/2} \quad (I > 2\sigma(I)).$$

$$^c \text{GoF} = [\Sigma (w(F^{o2} - F^{c2})^2 / \Sigma (N^r - N^p)^2)].$$

3-3-2 Optical properties of **Py_R** at ambient conditions

Emission spectra of **Py_R** were measured to reveal the effect of radical concentration on the luminescent behavior (Figure 3-3-4). **Py_0.05**, which had the lowest radical concentration, exhibited luminescence with peak wavelengths (λ_{em}) of 563 and 597 nm and a shoulder around 650 nm. The spectral shape was similar to that of PyBTM in CH_2Cl_2 ,¹⁷ suggesting that the luminescence of **Py_0.05** originated from the PyBTM monomer isolated in the crystal. A new broad emission band appeared at $\lambda_{em} \approx 680$ nm and the emission from the monomer of PyBTM suppressed relatively as the doping concentration increased. The evolution of a long-wavelength emission band with increasing the luminophore concentration in a host matrix is often observed in luminophore doping systems, and thus the new emission band in **Py_R** can be attributed to the excimer.^{19,27-29} A new emission band at the longer wavelength also appeared in a 19 wt% PyBTM-doped poly(methyl methacrylate) (PMMA), confirming that these emissions are attributed not to the matrices but to the excimer of PyBTM (Figure 3-3-5).

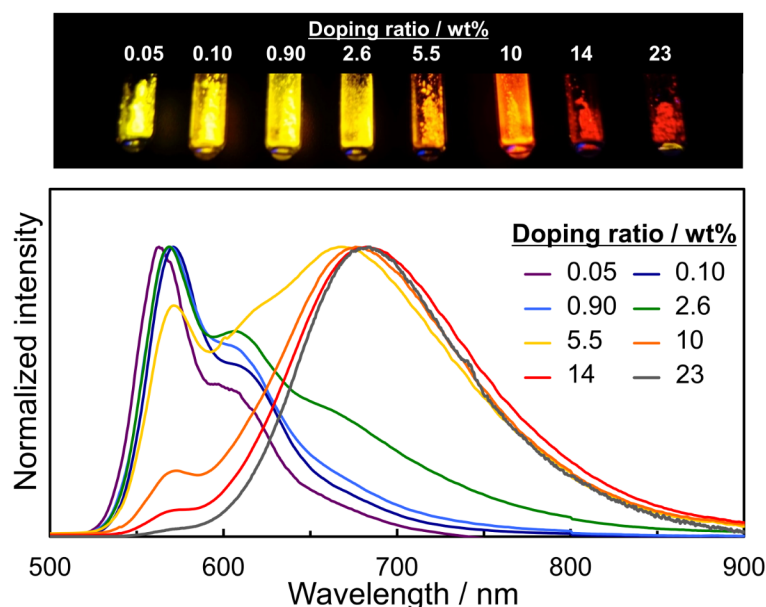


Figure 3-3-4. Emission spectra (lower, $\lambda_{ex} = 370$ nm) and photograph (upper, $\lambda_{ex} = 365$ nm) of **Py_R**.

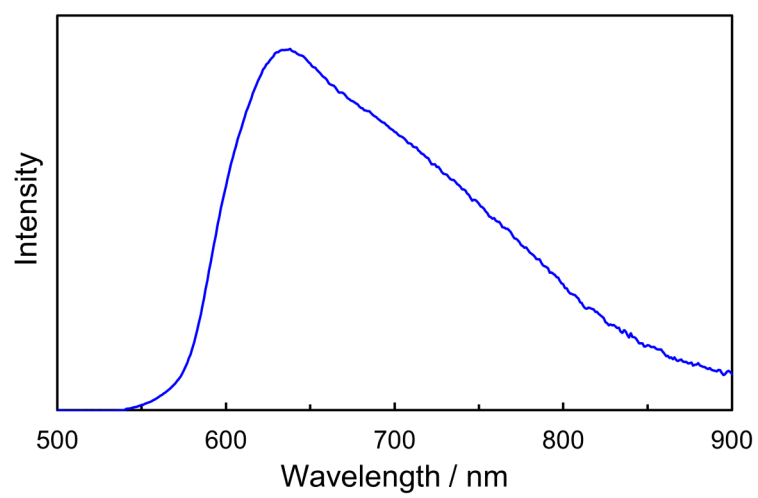


Figure 3-3-5. Emission spectrum of 19 wt% PyBTM-doped PMMA film.

I confirmed the excimer character by measuring the excitation spectra of **Py₁₀** showing the emissions from both the monomer and excimer. The spectra measured at the emission wavelengths of the monomer (570 nm) and excimer (680 nm) were similar to each other (Figure 3-3-6). These were also similar to the absorption spectrum of the CH₂Cl₂ solution of PyBTM.¹⁷ These results suggested that the PyBTM excimer was formed after photoexcitation while the radicals were negligibly interacted and dissociated in the ground states.¹⁹

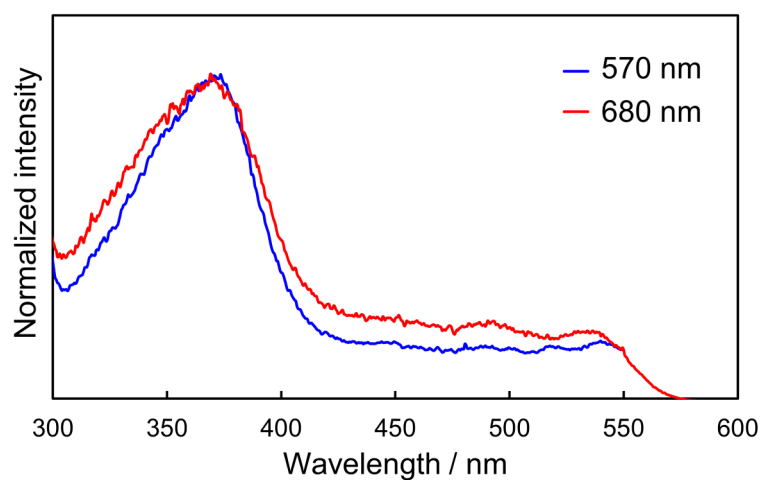


Figure 3-3-6. Excitation spectra of **Py₁₀** at $\lambda_{\text{em}} = 570$ and 680 nm.

Table 3-3-2 summarizes the photophysical properties of **Py_R**. ϕ_{em} increased with decreasing doping concentration, with **Py_0.05** showing the highest ϕ_{em} of 0.89. This value is extraordinarily high and *ca.* 30 times higher than that of the CH₂Cl₂ solution of PyBTM ($\phi_{\text{em}} = 0.03$).¹⁷ This is one of the highest values reported for organic radicals under ambient conditions; ϕ_{em} of 0.856 ± 0.054 for carbazole-substituted tris(trichlorophenyl)methyl radical (TTM) in 4,4-bis(carbazol-9-yl)biphenyl film,³⁰ 0.99 for carbazole-derivative- substituted TTM in the CHCl₃ solution,³¹ and 0.91 for iodo-substituted TTM doped into its precursor³² were reported very recently. The radiative transition rate (k_{r}) and non-radiative transition rate (k_{nr}) of **Py_0.05** were calculated as 6.7×10^6 and $8.3 \times 10^5 \text{ s}^{-1}$, respectively. k_{r} was comparable to that of PyBTM in CH₂Cl₂ ($3.9 \times 10^6 \text{ s}^{-1}$), whereas k_{nr} was 200 times smaller ($k_{\text{nr}} = 1.5 \times 10^8 \text{ s}^{-1}$ for PyBTM).²⁰ These results suggest that the highly rigid environment around PyBTM based on the similar molecular structures of PyBTM and αH -PyBTM restricts vibrational relaxation. These were consistent with our recent theoretical analysis showing that vibrational relaxation is a dominant non-radiative deactivation process in PyBTM.²⁰

Doping concentration strongly affected ϕ_{em} (Table 3-3-2 and Figure 3-3-7). In the low-concentration region, where PyBTM monomer emission was predominant (0.05 to 2.6 wt%), ϕ_{em} decreased sharply, probably due to the long-distance dipole–dipole interactions among separated PyBTM molecules. ϕ_{em} gradually decreased further to 0.05 for **Py_23** as the radical concentration increased and the PyBTM excimer emission became dominant (over 5.5 wt%).

Table 3-3-2. Photophysical properties of Py_R

Doping concentration / wt%	ϕ_{em}	τ^{560} / ns	τ_1^{560}	τ_2^{560}	τ_3^{560}	τ^{670} / ns	τ_1^{670}	τ_2^{670}
0.05	0.89	132	132	-	-	129	129	-
0.1	0.70	128	128	-	-	125	125	-
0.9	0.59	127	127	-	-	181	110 (88.7)	354 (11.3)
2.6	0.39	127	63 (88.0)	248 (12.0)	-	471	67 (79.3)	635 (20.7)
5.5	0.21	104	19 (94.5)	226 (5.5)	-	655	21 (79.8)	727 (20.2)
10	0.16	153	2.7 (81.0)	14 (17.9)	339 (1.1)	813	7 (73.6)	832 (26.4)
14	0.10	118	1.9 (91.0)	10 (8.3)	273 (0.7)	634	37 (59.8)	682 (40.4)
23	0.05	132	0.8 (94.4)	5 (5.0)	235 (0.6)	575	96 (29.5)	607 (70.5)

τ^{560} and τ^{670} are average lifetimes at 560 and 670 nm, respectively. τ_1^{560} , τ_2^{560} , τ_3^{560} , τ_1^{670} , and τ_2^{670} are lifetime components (and relative amplitudes) for τ^{560} or τ^{670} .

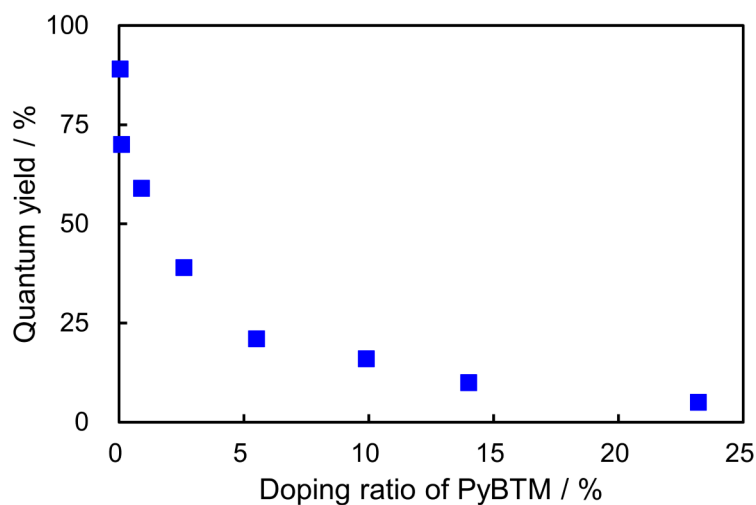


Figure 3-3-7. Absolute photoluminescence quantum yields of **Py_R**.

The decays of monomer-centered emissions at 560 nm for low-concentration samples (**Py_0.05**, **Py_0.10**, and **Py_0.90**) were fitted with a single exponential function and the lifetimes (τ_1^{560}) were all about 130 ns (Table 3-3-2 and Figure 3-3-8a). This τ_1^{560} value reflects the lifetime of PyBTM isolated in αH -PyBTM crystals. Due to the formation of excimers, at higher concentrations, one or two more components with long lifetimes were required for fitting the decay. It was difficult to analyze accurately the decay for samples with doping concentrations higher than 10 wt%, probably owing to the low ϕ_{em} and large contributions of excimer-centered components.

The decay of the excimer-centered emission at 670 nm was reproduced with one (for **Py_0.05** and **Py_0.10**) or two (for samples with doping concentrations higher than 0.10 wt%) components, τ_1^{670} and τ_2^{670} . τ_1^{670} was similar to τ_1^{560} at concentrations from 0.05% to 5.5%, suggesting that τ_1^{670} arose from monomer-centered emissions (Table 3-3-2 and Figure 3-3-8b). This is plausible because the monomer emission band extends over 670 nm. Thus, the remaining component, τ_2^{670} , was attributed to excimer-centered emissions. τ_2^{670} values were much larger than τ_1^{560} values. τ_2^{670} increased to a maximum value of 832 ns in **Py_10**, and then decreased as the radical concentration increased, indicating the formation of another type of radical oligomer or excimer at concentrations over 14 wt%.

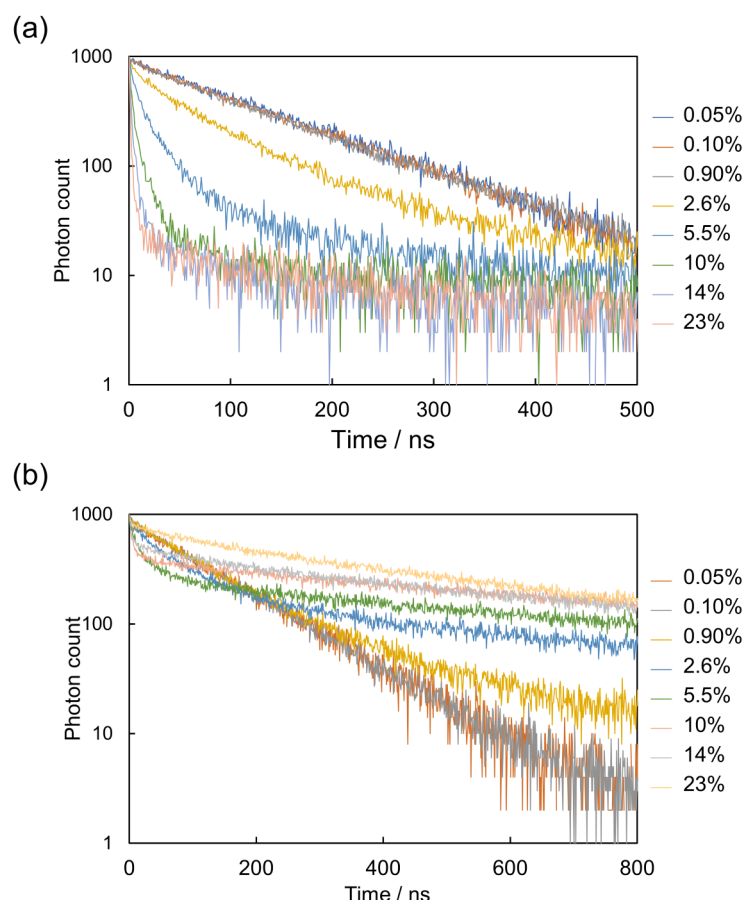


Figure 3-3-8. Emission decays of **Py_R** (a) at 560 and (b) at 670 nm.

3-3-3 Magnetoluminescence of **Py_R**

The emission spectra of the doped crystals were measured under an applied magnetic field below 20 K. Figure 3-3-9 shows the emission spectra of **Py_0.10**, which exhibits only a PyBTM monomer emission at 4.2 K under magnetic fields of 0, 6, 10, and 14.5 T. The spectra were identical in these magnetic fields, suggesting the absence of an MFE. These results show that the luminescence of isolated PyBTM does not display an MFE, reflecting its fluorescent character based on the doublet-doublet transitions and negligibly involving other excited states with different spin multiplicities. No MFE was also observed in the emission spectrum of a PMMA film doped with PyBTM at a low concentration of 0.05 wt% (Figure 3-3-10), supporting the absence of an MFE in the isolated PyBTM.

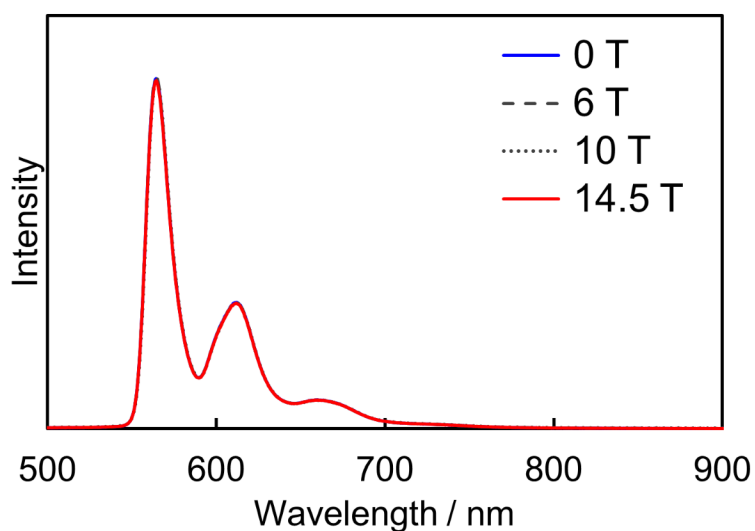


Figure 3-3-9. Emission spectra of **Py_0.10** at 4.2 K under a magnetic field.

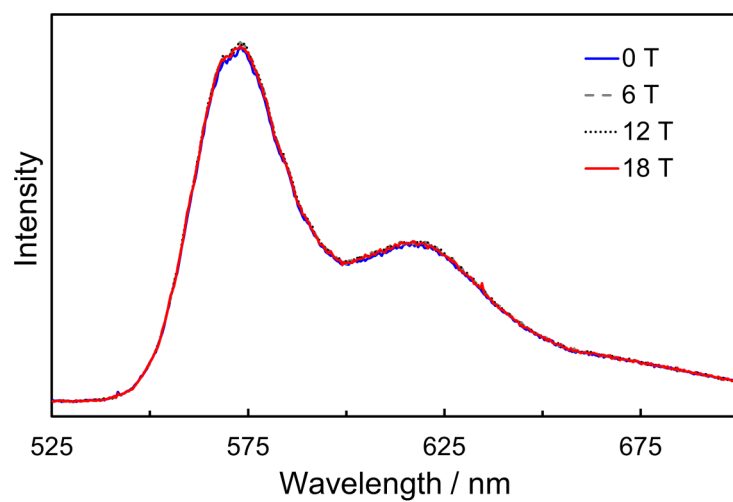


Figure 3-3-10. Emission spectra of 0.05 wt% PyBTM-doped PMMA film at 4.2 K under a magnetic field.

In contrast, the emission behavior of **Py_10** showing both the PyBTM monomer and excimer emissions was strongly modulated by an external magnetic field (Figure 3-3-11). The intensity of the monomer emission at λ_{em} of 563 nm increased significantly, whereas the excimer emission at λ_{em} of 674 nm was slightly suppressed. This is the first example of an MFE on the luminescence of stable radicals to the best of my knowledge. The monomer and excimer emissions were correlated with each other because they exhibited similar intensity changes in magnitude under the magnetic field (Figure 3-3-12). Nearly identical changes in emission spectra under a magnetic field were observed for 14 wt% bisPyTM doped into αH -bisPyTM crystals at 4.2 K (Figure 3-3-13), suggesting some generality in the MFE and its mechanism in this class of luminescent radicals.

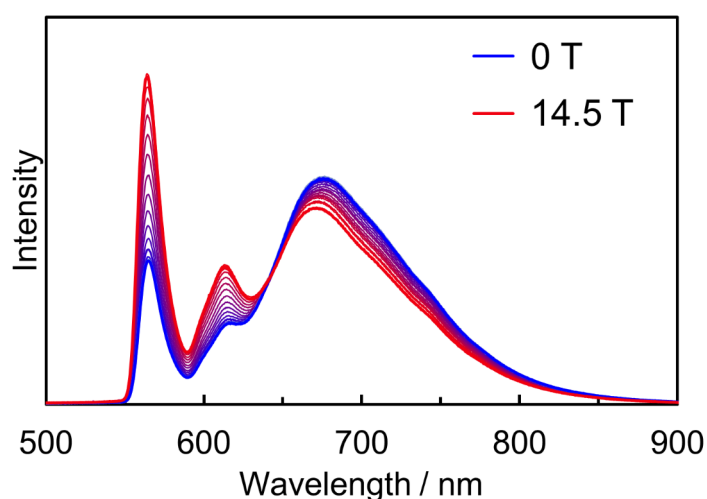


Figure 3-3-11. Emission spectra of **Py_10** at 4.2 K under magnetic fields from 0 to 14.5 T.

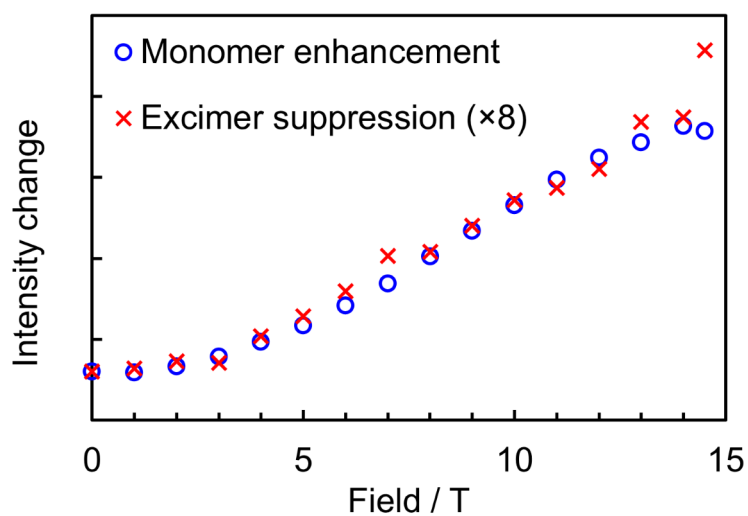


Figure 3-3-12. Intensity changes of **Py₁₀** at 4.2 K under a magnetic field.

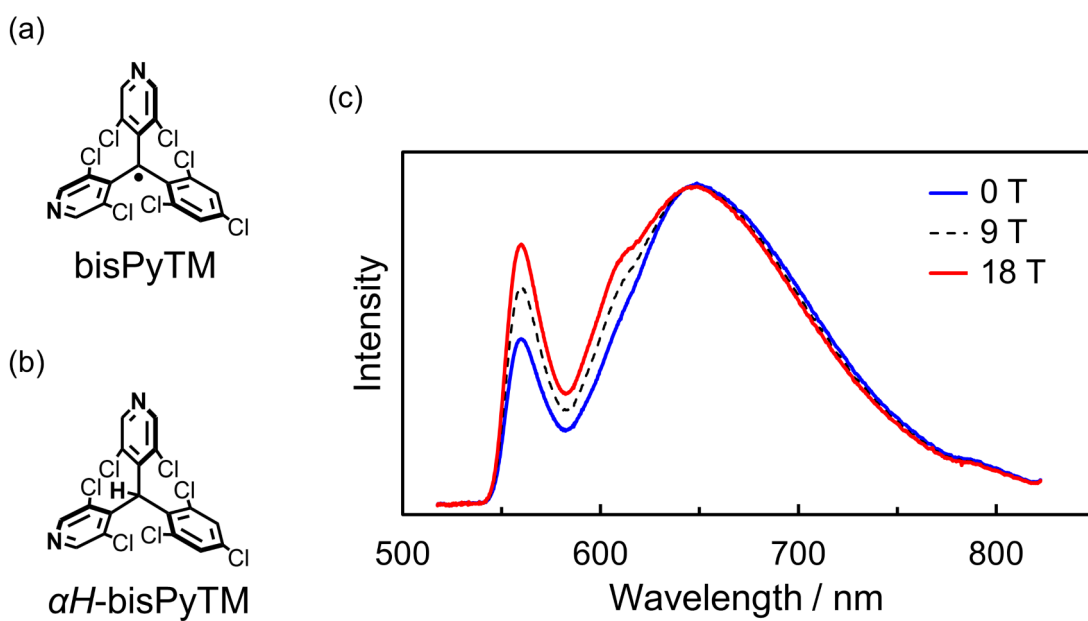


Figure 3-3-13. Magneoluminescence in bisPyTM-doped crystals. Molecular structures of (a) bisPyTM and (b) αH -bisPyTM. (c) Emission spectra of 14 wt% bisPyTM-doped αH -bisPyTM crystals at 4.2 K under a magnetic field.

The emission decay curves of **Py_10** were investigated in detail to elucidate the magnetic field effect on the luminescent behaviors. Decays of monomer and excimer emissions were monitored at both emission peak wavelengths with external magnetic fields from 0 to 14.5 T (Figure 3-3-14). Obtained decay curves were fitted with a stretched exponential function (Eq. 3-3-1) to visualize the changes in decay curves.^{19,26}

$$I(t) = I_0 \exp\{-(t/\tau)^\beta\} \quad (\text{Eq. 3-3-1})$$

where τ is the lifetime and β is the stretch factor, a dimensionless parameter with a range of $0 < \beta \leq 1$. Stretched exponential functions can be utilized when distributions of decay times or rate constants are expected, such as in rigid solutions,³³ polymers,³⁴ and energy transfer in assemblies of fluorophores.³⁵ Figure 3-3-14c summarizes the magnetic field dependences of the lifetimes and amplitudes for the decays of the monomer emission at 563 nm. The lifetimes at 4.2 K increased from 19 ns at 0 T to 24 ns at 14.5 T. The amplitude also increased with the magnetic field and reached about 1.9 times the initial amplitude at 14.5 T. The decays at 674 nm were fitted with two stretched exponential functions; one of which is for the corresponding monomer emission, because the monomer and excimer emissions were expected to overlap at the emission wavelength.²⁵ Figure 3-3-14d shows the magnetic field dependences of the lifetimes and amplitudes for the components corresponding to the excimer-centered emission. The amplitude decreased while the lifetime was almost unchanged as the magnetic field increased. The insensitivity to the magnetic field of the lifetime indicated that the emission from the excimer excited state was the rate-determining process.

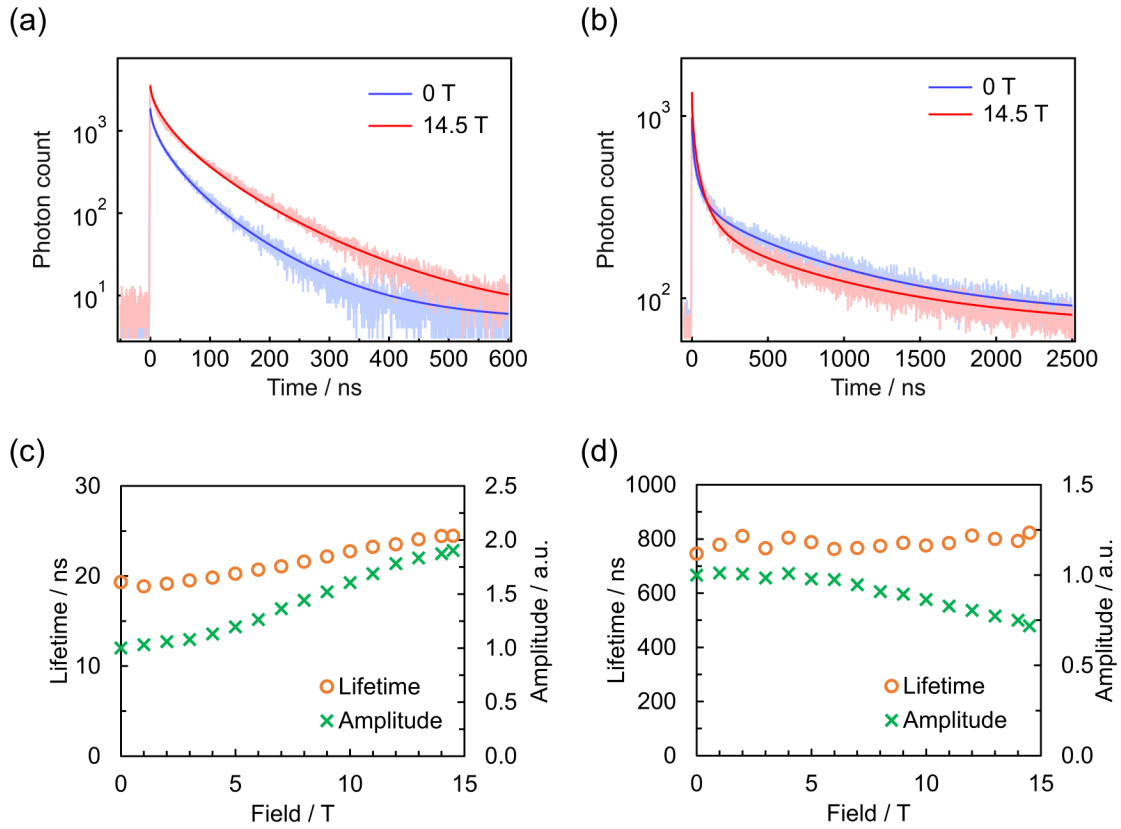


Figure 3-3-14. Emission decays of Py₁₀. (a,b) Emission decays of **Py₁₀** and corresponding fits at 4.2 K under magnetic fields of 0 and 14.5 T at (a) 563 nm (b) and 674 nm. (c,d) Magnetic field dependences of lifetimes and amplitudes at 4.2 K at (c) 563 nm with $\beta = 0.59$ and (d) 674 nm with $\beta = 0.88$.

3-3-4 Doping concentrations dependency of magnetoluminescence of **Py_R**

Similar emission decay behaviors were also observed in **Py_4** (Figures 3-3-15a and 3-3-16) and **Py_22** (Figures 3-3-15b and 3-3-17), with lower and higher radical concentrations than **Py_10**. On the other hand, **Py_0.10**, which exhibited only a monomer emission, displayed no changes in amplitude or lifetime (Figure 3-3-18). These results suggested that the MFE species and mechanism of aggregated PyBTM were the same in all the **Py_R** crystals.

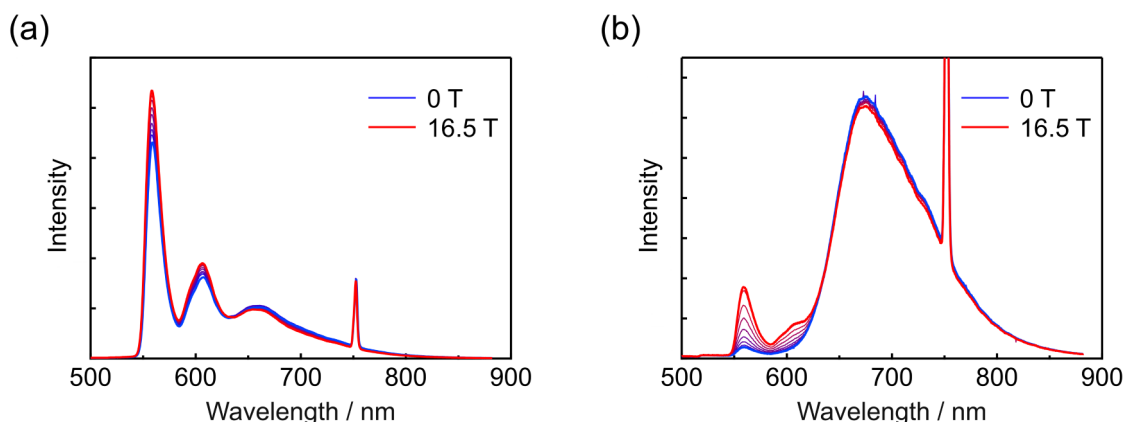


Figure 3-3-15. Emission spectra of **Py_4 and **Py_22** under magnetic fields.** Emission spectra of (a) **Py_4** and (b) **Py_22** at 4.2 K under magnetic fields of 0 to 16.5 T. Peaks at 750 nm are due to the excitation laser light ($\lambda_{\text{ex}} = 375$ nm).

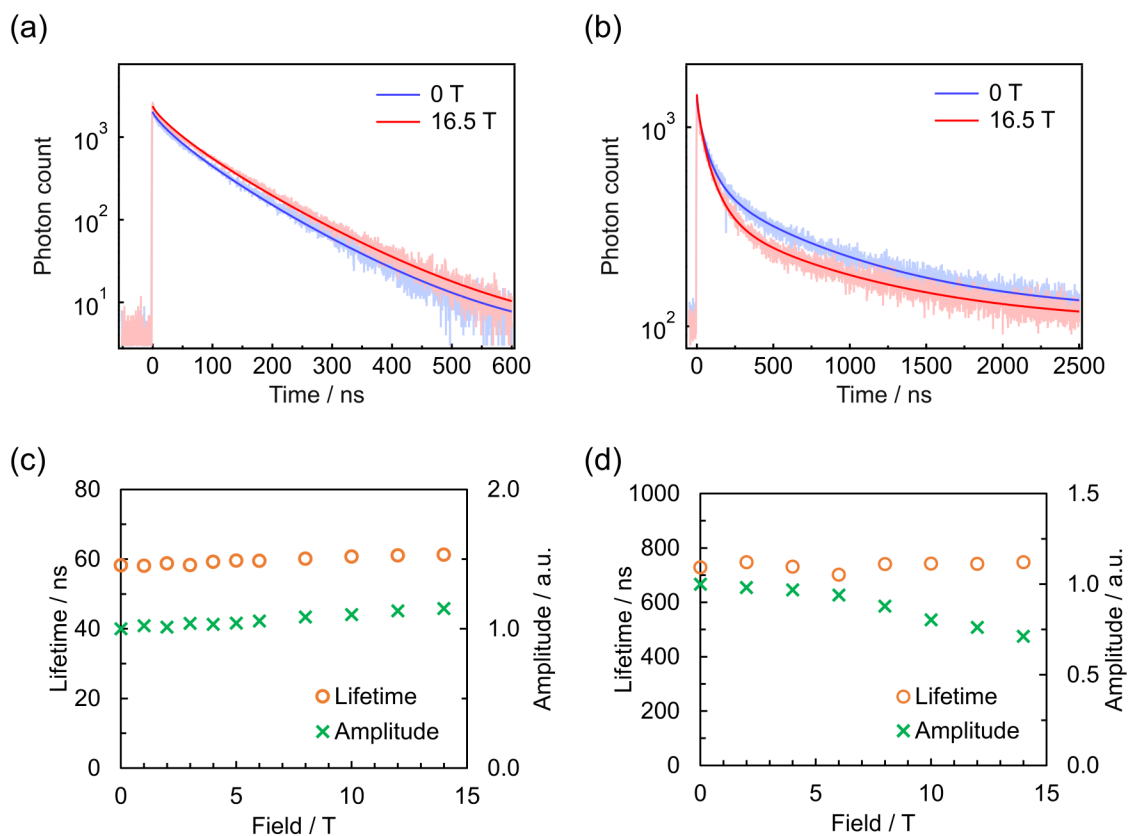


Figure 3-3-16. Emission decays of Py₁₀. (a,b) Emission decays of **Py₄** and corresponding fits at 4.2 K under magnetic fields of 0 and 16.5 T at (a) 553 nm (b) and 700 nm. (c,d) Magnetic field dependences of lifetimes and amplitudes at 4.2 K at (c) 553 nm with $\beta = 0.78$ and (d) 700 nm with $\beta = 0.90$.

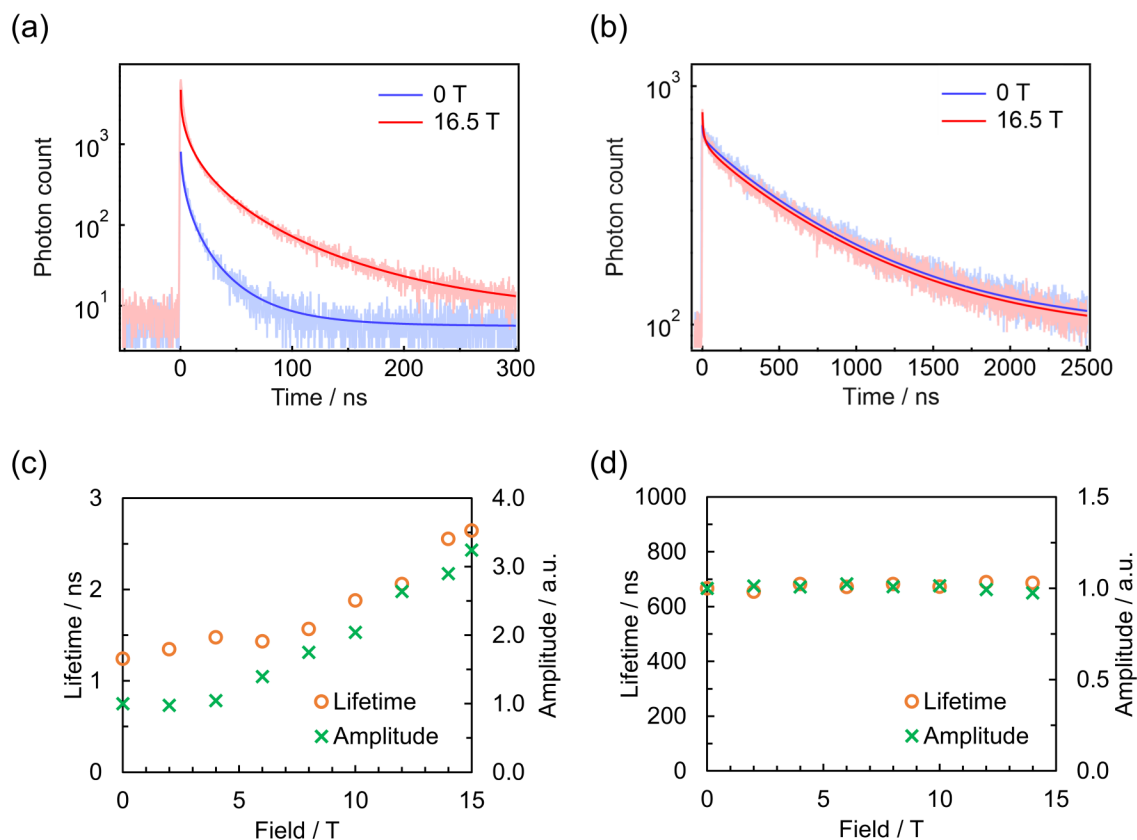


Figure 3-3-17. Emission decays of **Py₂₂.** (a,b) Emission decays of **Py₂₂** and corresponding fits at 4.2 K under magnetic fields of 0 and 16.5 T at (a) 559 nm (b) and 700 nm. (c,d) Magnetic field dependences of lifetimes and amplitudes at 4.2 K at (c) 559 nm with $\beta = 0.41$ and (d) 700 nm with $\beta = 0.90$.

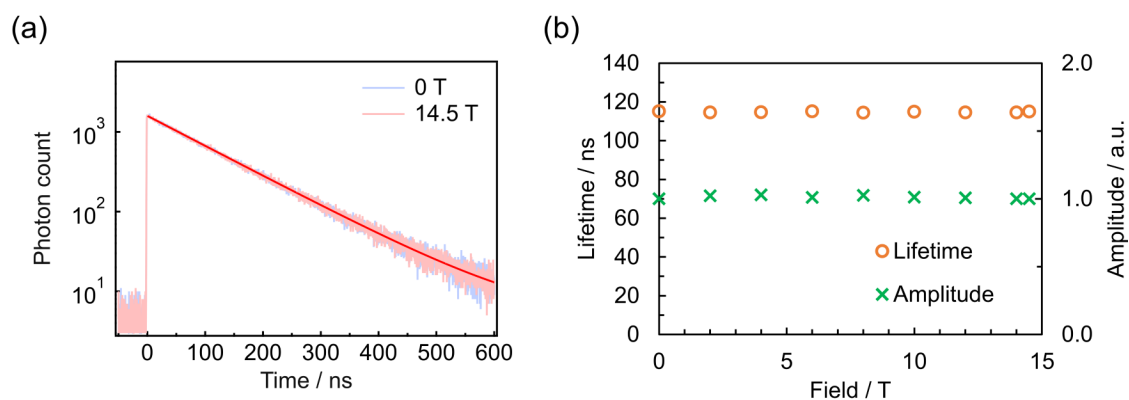


Figure 3-3-18. Emission decays of **Py_{0.10}.** (a) Emission decays of **Py_{0.10}** at 4.2 K under 0 and 14.5 T and corresponding fits at 565 nm and (b) magnetic field dependences of the lifetimes and amplitudes with $\beta = 1.00$.

3-3-5 Temperature dependency of magnetoluminescence of **Py_R**

The field- and temperature-dependent emission spectra of **Py₁₀** were measured from 0 to 18 T and 4.2 to 20 K (Figure 3-3-19). The ratio of emission intensities at 560 and 663 nm ($\lambda_{560}/\lambda_{663}$), mainly attributed to the monomer and excimer emissions, respectively, were plotted (Figure 3-3-20). $\lambda_{560}/\lambda_{663}$ at 4.2 K increased by about 3 times as the magnetic field reached 18 T; it started to increase sigmoidally from around 2 T, and then was almost saturated over 16 T. As the temperature increased from 4.2 K to 20 K, the magnitude of the increase was gradually decreased. These behaviors were reversible with temperature, showing that the radicals did not decompose.

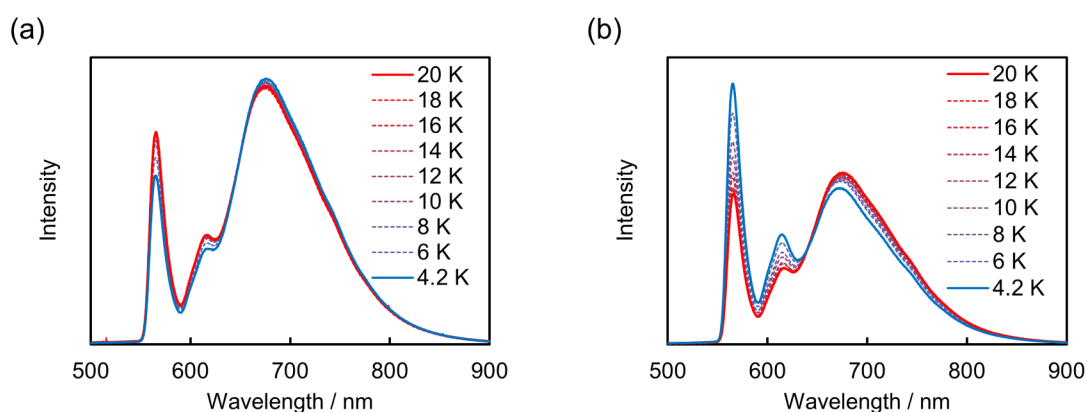


Figure 3-3-19. Temperature-dependences of emission spectra. Emission spectra of **Py₁₀** at 4.2, 6, 8, 10, 12, 14, 16, 18, and 20 K under (a) 0 T and (b) 14.5 T.

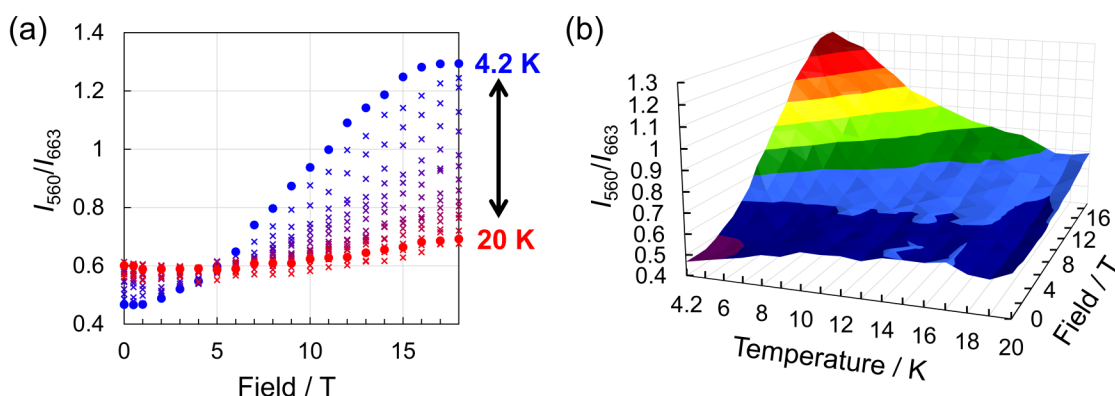


Figure 3-3-20. Temperature-dependences of magnetoluminescence behaviors. (a) Magnetic field dependence of $\lambda_{560}/\lambda_{663}$ of **Py₁₀** at 4.2, 5, 6, 7, ..., and 20 K and (b) 3D mapping of (a).

Temperature-dependent emission decays also visualized the negative effect of the thermal energy on the MFE. Figure 3-3-21 shows the temperature-dependent emission decays for the monomer emission at 563 nm of **Py_10** at 0 and 14.5 T. The differences in the amplitude and lifetime between decays at 0 and 14.5 T (*i.e.*, the MFE) at 4.2 K reduced with increasing temperature, and became negligible at 20 K. Temperature-dependences of excimer emission decays showed similar results, where the MFE was diminished as temperature increased (Figure 3-3-22). These results indicate thermally activated processes involved in the mechanism of the MFE with its activation energy below $k_B T$ with $T = 20$ K.

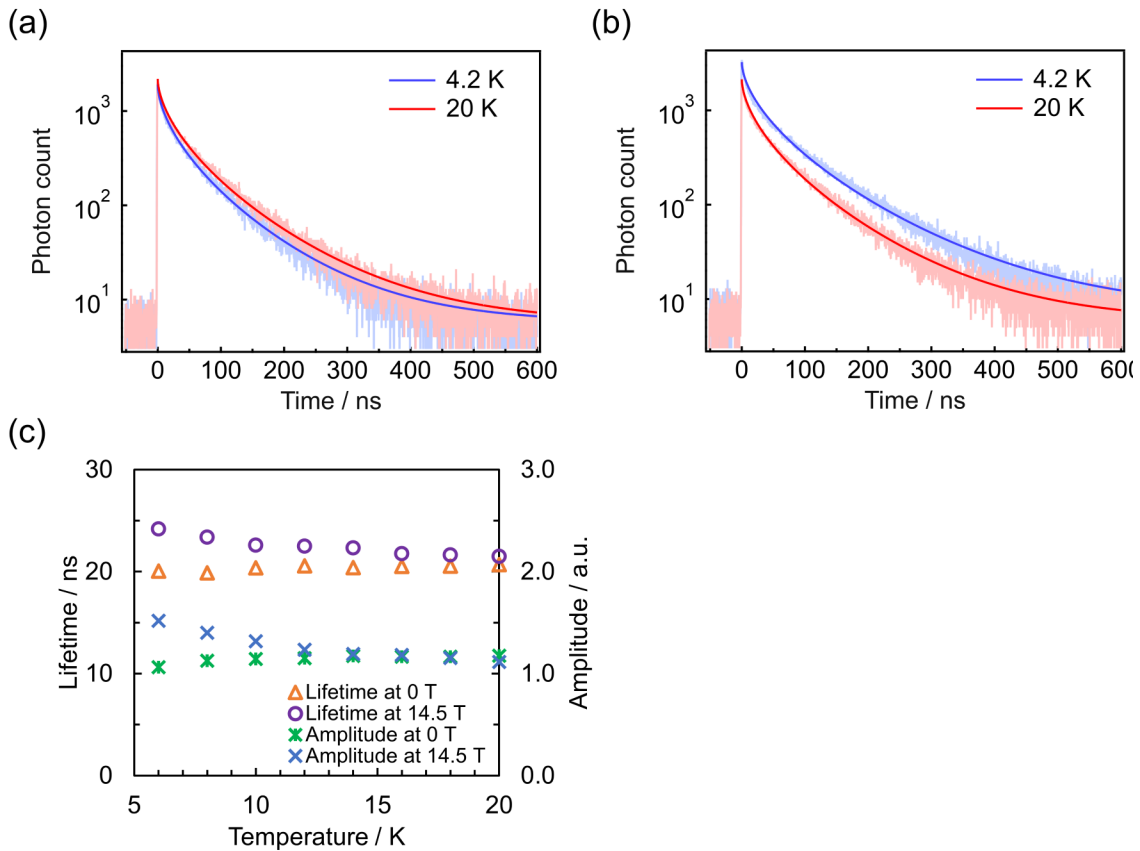


Figure 3-3-21. Temperature-dependence of the monomer emission decays of **Py_10.** (a,b) Emission decays and corresponding fits of **Py_10** at 4.2 K and 20 K under (a) 0 T and (b) 14.5 T at 563 nm. (c) Temperature-dependences of their lifetimes and amplitudes with $\beta = 0.59$ under 0 and 14.5 T for **Py_10**.

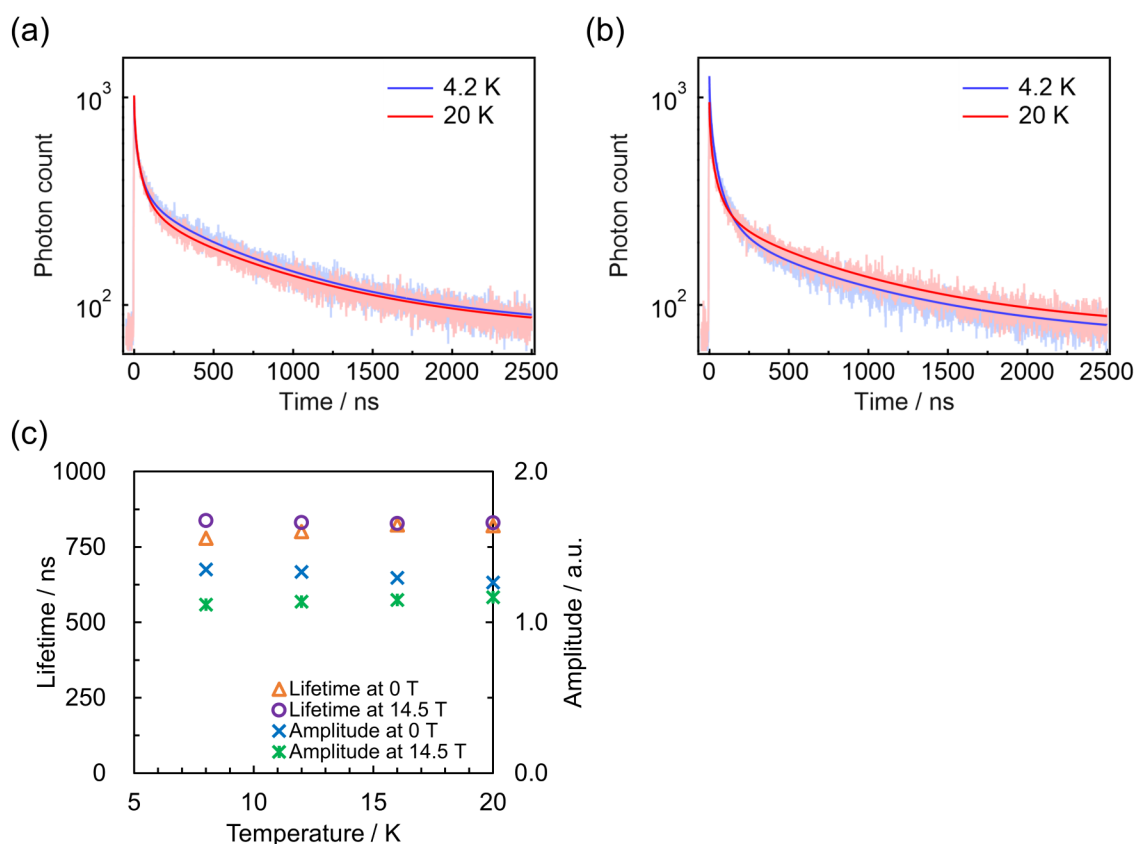


Figure 3-3-22. Temperature-dependence of the excimer emission decays of Py₁₀.

(a,b) Emission decays and corresponding fits of **Py₁₀** at 4.2 K and 20 K under (a) 0 T and (b) 14.5 T at 674 nm. (c) Temperature-dependences of their lifetimes and amplitudes with $\beta = 0.88$ under 0 and 14.5 T for **Py₁₀**. The figure only shows the component corresponding to the excimer emission.

3-3-6 Mechanism of magnetoluminescence of **Py_R**

The emission lifetime measurements allowed us to construct a scheme for the MFE based on the following four results (Figure 3-3-23a): the monomer emission amplitude increased with the magnetic field (Figure 3-3-17c); the MFE was counteracted by thermal energy (Figure 3-3-19 to 21); the photon counts of the monomer emission decay had the largest values just after photoexcitation (Figure 3-3-17a); and the lifetime of the monomer emission increased with the magnetic field (Figure 3-3-17c).

The increase in amplitude of the monomer emission with an external magnetic field suggests that the spin sublevel population of a PyBTM dimer in the ground state is associated with the MFE (Figure 3-3-23a, green dashed box); the amplitude should be independent of the field-sensitive kinetics in the excited states (*i.e.*, field-dependent ISC) and thus be determined by the characteristics of the ground state. The spin states of the PyBTM dimers (*i.e.*, the population between the S, T₊, T₀, and T₋ states) are modulated by the magnetic field and heat (via Zeeman splitting and the Boltzmann distribution, respectively). In the absence of a magnetic field, the population of the S state is the largest, whereas the population of the T₋ state increases with a magnetic field and becomes dominant because the exchange interactions (J) between the radicals in **Py_R** are antiferromagnetic (Figure 3-3-23b).²⁵ This ground-state associated MFE is consistent with the decrease in the MFE with increasing the temperature; the thermal energy increases the population in the S state and decreases the population in the T₋ state at 14.5 T, and thus counteracts the MFE. The highest photon count occurring just after photoexcitation suggests that the radical dimers are excited to emissive states via photoexcitations and following fast relaxations to the lowest excited states based on Kasha's rule³⁶ (Figure 3-3-23a, magenta dashed box), because the photon count corresponds the populations in the emissive excited states. Furthermore, the increase in lifetime of the monomer emission with magnetic field suggests the existence of two excited states with different lifetimes. Considering that the populations of triplet ground states are increased by applying the magnetic field, the triplet excited states should have longer lifetimes than the singlet excited states (Figure 3-3-23a, blue dashed box).

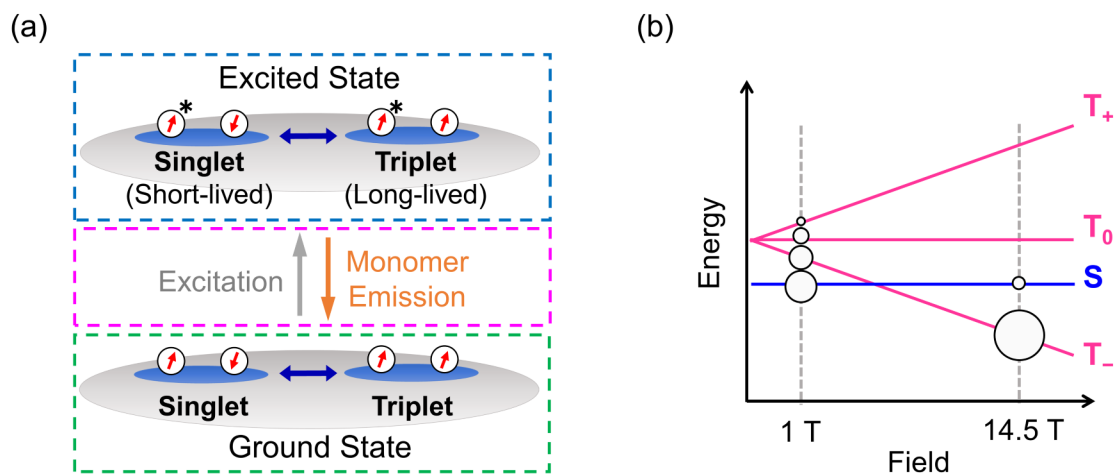


Figure 3-3-23. Scheme of magnetoluminescence and spin sublevel population of a dimer radical. (a) Scheme based on lifetime measurements, showing the changes in spin sublevel populations in the ground state (green dashed box), direct excitations to emissive states (magenta dashed box), and two excited states with different lifetimes (blue dashed box). (b) Population distribution as a function of applied magnetic field.

Based on this discussion, I proposed the MFE scheme for **Py₂R** (Figure 3-3-24a). Two factors in the scheme are sensitive to the magnetic field: the distribution among the singlet (S) and triplet (T_{-} , T_0 , T_{+}) ground states (ground-state MFE) and the ISC between singlet (S) and triplet (T_0) in RPs by the Δg mechanism (excited-state MFE). The (R-R) is a PyBTM dimer in the ground state with singlet or triplet spin multiplicity. Photoirradiation excites a PyBTM radical R in (R-R) to form a RP state, ($R^{*}---R$). The coupling between R^{*} and R in ($R^{*}---R$) is so weak that it can behave as PyBTM monomer and exhibits emission with transition rate k_{m1} ($k = 1/\tau$ in Eq. 3-3-1) and stretch factor β_1 .²⁶ $^1(R---R)^{*}$ can generate the singlet excimer, $^1(R-R)^{*}$, with rate constant k_{Sex} . I also assumed a close RP,³⁷⁻⁴⁰ ($R^{*}--R$), where field-sensitive ISC does not happen because of the energy gap between the S and the T_0 states resulting from non-negligible exchange interactions (Figure 3-3-24b). Although the $^3(R--R)$ state displays a PyBTM monomer emission with transition rate k_{m2} and stretch factor β_2 , the $^1(R--R)$ state is assumed to form the singlet excimer immediately after photoexcitation because of strong intrapair interactions. As the population of the $^3(R--R)$ state increased with magnetic field, the populations in the excited states responsible for monomer emission increased, which is consistent with the increase in monomer emission amplitudes with a magnetic field.

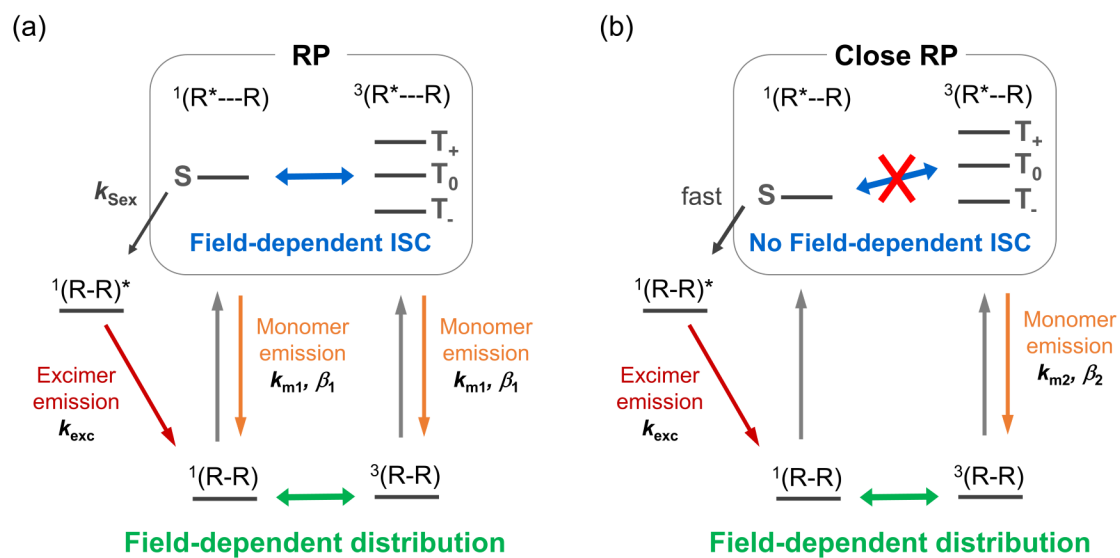


Figure 3-3-24. Proposed species responsible for the MFE. k_{m1} , k_{m2} , and k_{exc} are the totals of radiative and nonradiative transition rates for the monomer emission of RP, that of close RP, and the excimer emission, respectively.

A quantum mechanical simulation was performed based on the scheme in Figure 3-3-24 with the parameters of Entry 1 in Table 3-3-3. Figure 3-3-25ab shows that the magnetic field dependences of the monomer emission intensities and decays were well reproduced by the simulation, although the excimer emission intensity changes were overestimated (Figure 3-3-26). This overestimation indicated that more aggregated species, which are negligibly sensitive to the magnetic field, contributed to the excimer emission. The trends of temperature dependence of the emission decay were also reproduced (Figure 3-3-27). Figure 3-3-24cd shows the simulated monomer emission intensities without the excited-state or ground-state MFE, and the shaded areas show the contribution of each MFE. Although the excited-state MFE slightly contributed to the emission intensity in the low-field region, the ground-state MFE greatly increased the emission intensity in the high-field region. The values of the parameters were estimated with various restriction conditions listed in Table 3-3-3, and Figure 3-3-28 shows the simulated emission decays and intensities with these parameters. In all cases, the contributions of “ground-state MFE” to monomer emission intensities were much superior to those of “excited-state MFE”, as observed in Figure 3-3-25. These results suggest that the ground-state MFE is critical to magnetoluminescence in this system (Figure 3-3-29a); this is distinct from conventional ground-state closed-shell systems, in which only excited state MFEs occur (Figure 3-3-29b).

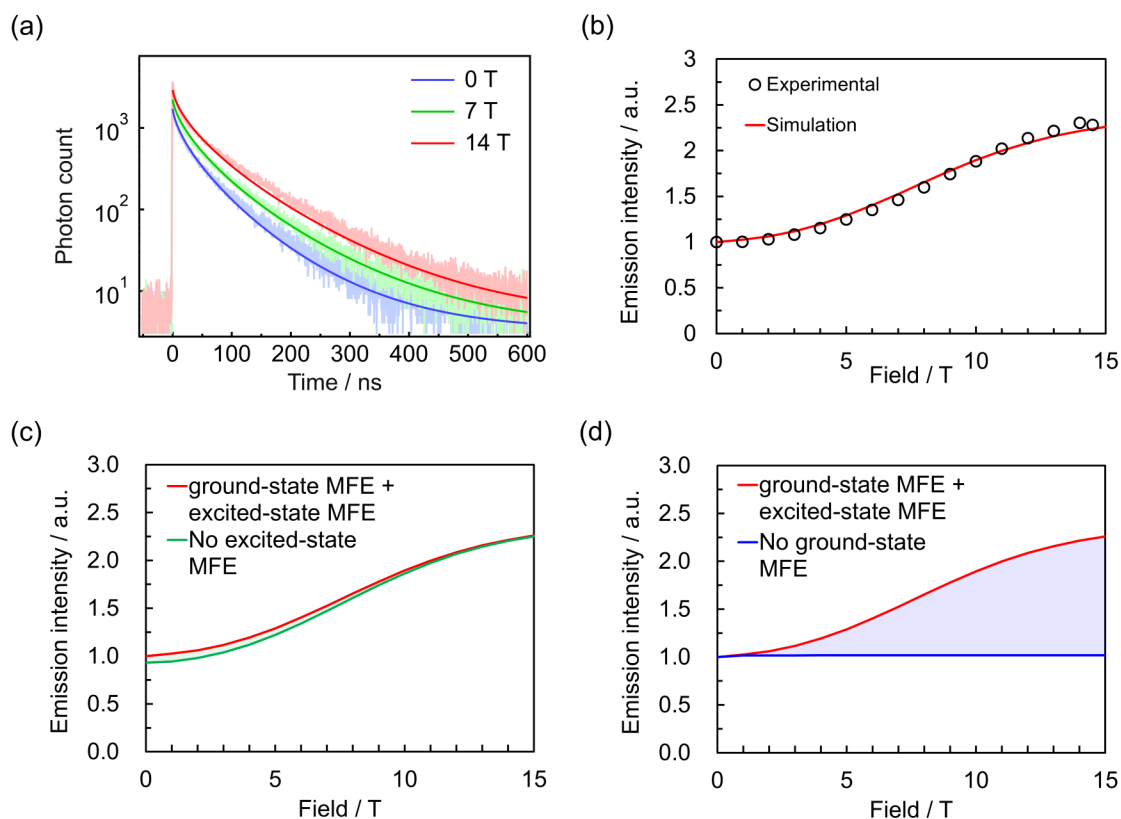


Figure 3-3-25. Simulations of monomer emission decays and intensities. (a) Simulated and experimental monomer emission decays ($\lambda_{\text{em}} = 563$ nm) at 0, 7, and 14 T at 4.2 K. (b) Simulated and experimental magnetic field dependences of monomer emission intensities. (c,d) Simulated monomer emission intensities without considering the MFE on (c) the ground states and (d) the excited states.

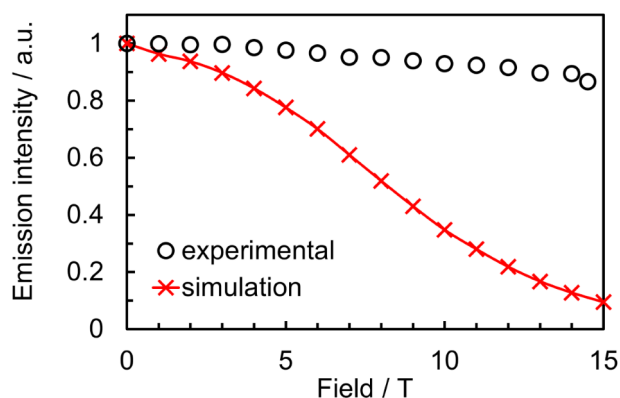


Figure 3-3-26. Simulated and experimental magnetic-field-dependences ($\lambda_{\text{em}} = 674$ nm) of excimer emission intensities at 4.2 K.

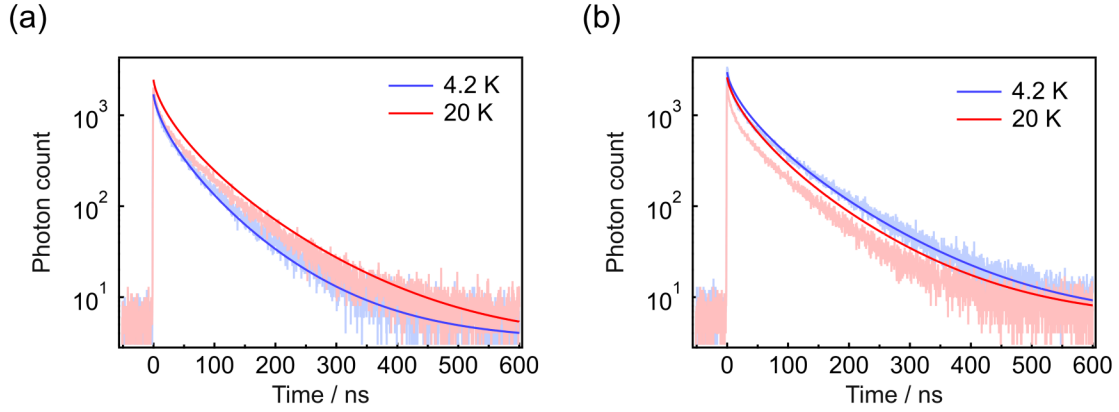
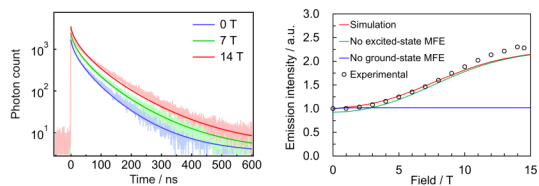


Figure 3-3-27. Simulated and experimental emission decays ($\lambda_{\text{em}} = 563$ nm) at 4.2 K and 20 K under (a) 0 T and (b) 16.5 T at 563 nm.

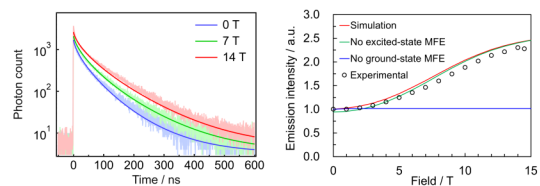
Table 3-3-3. The estimated values of the parameters, k_{m1} , k_{m2} , β_1 , β_2 , k_{Sex} , and the ratio of (population) \times (radiative transition rate) for (RP species)/(Close RP species). The values written in bold letters indicate the fixed parameters

Entry	k_{m1} / 10^7 s^{-1}	k_{m2} / 10^7 s^{-1}	β_1	β_2	k_{Sex} / 10^7 s^{-1}	Ratio of (population) \times (radiative transition rate) for (RP species)/ (Close RP species)
1	3.24	3.51	0.63	$= \beta_1$	1.71	0.7
2	3.58	4.50	0.60	$= \beta_1$	1.51	0.4
3	2.97	2.99	0.66	$= \beta_1$	1.86	1.0
4	6.37	2.35	0.51	0.7425	1.45	0.7
5	4.78	2.44	0.68	$= \beta_1$	0.50	0.7
6	4.21	2.82	0.65	$= \beta_1$	1.00	0.7
7	2.98	3.56	0.64	$= \beta_1$	2.00	0.7
8	3.08	2.35	0.71	$= \beta_1$	5.00	0.7
9	2.30	$= 2k_{\text{m1}}$	0.66	$= \beta_1$	1.96	0.7

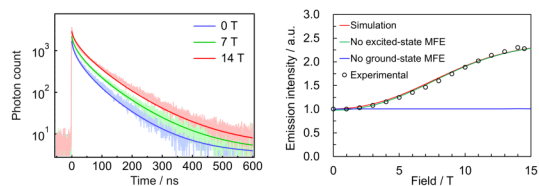
Entry 2



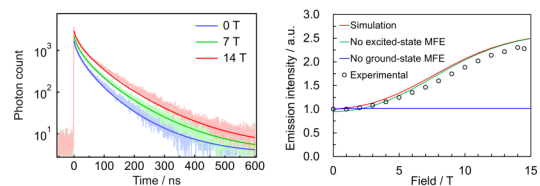
Entry 3



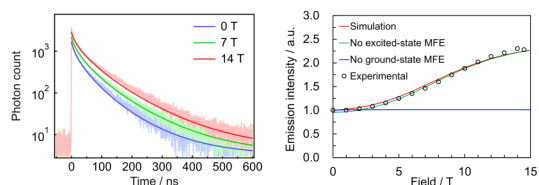
Entry 4



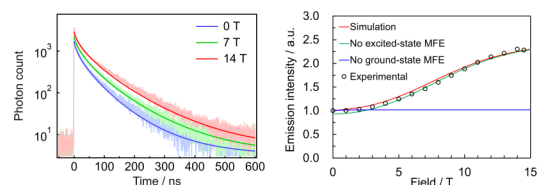
Entry 5



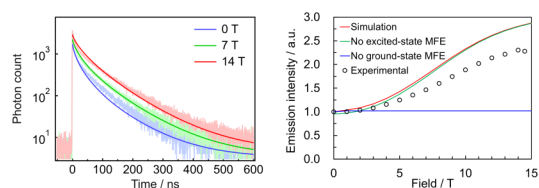
Entry 6



Entry 7



Entry 8



Entry 9

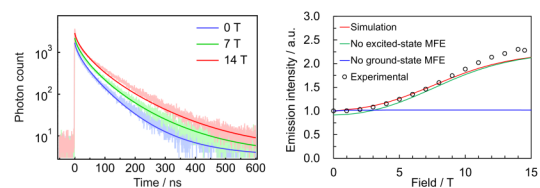


Figure 3-3-28. Simulations of monomer emission decays and intensities with the various parameters. Simulated monomer emission decays at 0, 7, and 14 T and magnetic field dependences of monomer emission intensities for each entry listed in Table 3-3-3 at 4.2 K. The results for Entry 1 are shown Figure 3-3-25.

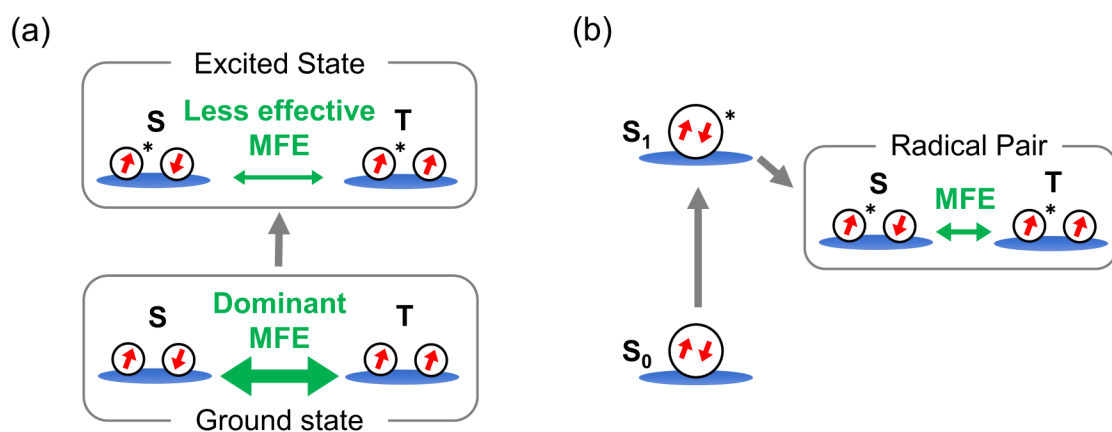


Figure 3-3-29. Schematic images of MFEs. (a) radicals (this system) and (b) conventional ground-state closed-shell molecules.

3-4 Conclusions

PyBTM-doped molecular crystals, **Py_R**, were shown to display unique emission behaviors depending on the radical concentration and magnetic field. **Py_0.05** showed an excellent ϕ_{em} of 0.89 at room temperature. The high emission efficiency with the doublet emitter proves the radicals' great potential for the high-performance emitting devices. The magnetoluminescence in organic radicals was observed for the first time in **Py_4**, **Py_10**, and **Py_22**. The mechanism of the MFE was revealed by time-resolved emission measurements under a magnetic field and the dependences of lifetimes and amplitudes on doping concentration and temperature. In-depth investigations in the magnetic field region of 0~18 T allowed us to construct MFE schemes unique to luminescent organic radicals with doublet characters. The simulated emission decay curves based on the MFE schemes agreed well with experimental data. The results suggested that the MFE in this system was dominated by magnetic-field-sensitive spin sublevel populations in the ground states. These characteristics are based on the degree of freedom in the ground-state spin multiplicities of aggregated radicals, and have not been achieved in conventional ground-state closed-shell molecules to the best of my knowledge.

These results not only provide the first example of magnetic field-luminescence correlated properties of organic radicals but also contribute to the molecular design of materials showing magnetoluminescence with organic radicals to achieve novel spin-luminescence correlated properties.

3-5 References

- [1] D. Le Sage, K. Arai, D. R. Glenn, S. J. Devience, L. M. Pham, L. Rahn-Lee, M. D. Lukin, A. Yacoby, A. Komeili and R. L. Walsworth, *Nature*, 2013, **496**, 486–489.
- [2] A. H. Devir-Wolfman, B. Khachatryan, B. R. Gautam, L. Tzabary, A. Keren, N. Tessler, Z. V. Vardeny and E. Ehrenfreund, *Nat. Commun.*, 2014, **5**, 4529.
- [3] J. Wang, A. Chepelianskii, F. Gao and N. C. Greenham, *Nat. Commun.*, 2012, **3**, 1191.
- [4] U. E. Steiner and T. Ulrich, *Chem. Rev.*, 1989, **89**, 51–147.
- [5] H. Hayashi, Introduction to Dynamic Spin Chemistry: Magnetic Field Effects on Chemical and Biochemical Reactions, World Scientific, Singapore, **2004**, p.1–254.
- [6] Y. Mori, Y. Sakaguchi and H. Hayashi, *J. Phys. Chem. A*, 2002, **106**, 4453–4467.
- [7] M. Murakami, K. Maeda and T. Arai, *Chem. Phys. Lett.*, 2002, **362**, 123–129.
- [8] Y. Mori, Y. Sakaguchi and H. Hayashi, *Chem. Phys. Lett.*, 1998, **286**, 446–451.
- [9] H. Pan, Y. Shen, L. Luan, K. Lu, J. Duan and B. Hu, *J. Phys. Chem. C*, 2015, **119**, 8089–8094.
- [10] K. Kato, S. Hagi, M. Hinoshita, E. Shikoh and Y. Teki, *Phys. Chem. Chem. Phys.*, 2017, **19**, 18845–18853.
- [11] R. C. Johnson and R. E. Merrifield, *Phys. Rev. B*, 1970, **1**, 896–902.
- [12] R. E. Merrifield, *J. Chem. Phys.*, 1968, **48**, 4318–4319.
- [13] G. B. Piland, J. J. Burdett, D. Kurunthu and C. J. Bardeen, *J. Phys. Chem. C*, 2013, **117**, 1224–1236.
- [14] T. Mani and S. A. Vinogradov, *J. Phys. Chem. Lett.*, 2013, **4**, 2799–2804.
- [15] L. R. Faulkner and A. J. Bard, *J. Am. Chem. Soc.*, 1969, **91**, 6495–6497.
- [16] Q. Peng, A. Obolda, M. Zhang and F. Li, *Angew. Chem. Int. Ed.*, 2015, **54**, 7091–7095.
- [17] Y. Hattori, T. Kusamoto and H. Nishihara, *Angew. Chem. Int. Ed.*, 2014, **53**, 11845–11848.
- [18] A. Obolda, X. Ai, M. Zhang and F. Li, *ACS Appl. Mater. Interfaces*, 2016, **8**, 35472–35478.
- [19] D. Blasi, D. M. Nikolaidou, F. Terenziani, I. Ratera and J. Veciana, *Phys. Chem. Chem. Phys.*, 2017, **19**, 9313–9319.

- [20] S. Kimura, T. Kusamoto, S. Kimura, K. Kato, Y. Teki and H. Nishihara, *Angew. Chem. Int. Ed.*, 2018, **57**, 12711–12715.
- [21] S. Kimura, A. Tanushi, T. Kusamoto, S. Kochi, T. Sato and H. Nishihara, *Chem. Sci.*, 2018, **9**, 1996–2007.
- [22] A. Altomare, G. Cascarano, C. Giacovazzo, A. Guagliardi, M. C. Burla, G. Polidori and M. Camalli, *J. Appl. Cryst.* 1994, **27**, 435.
- [23] G. M. Sheldrick, *Acta Cryst. A* 2008, **64**, 112–122.
- [24] Y. Sawada, S. Kimura, K. Watanabe and M. Nakano, *J. Low Temp. Phys.*, 2013, **170**, 424–429.
- [25] K. Kato, S. Kimura, T. Kusamoto, H. Nishihara and Y. Teki, *Angew. Chem. Int. Ed.*, 2019, **58**, 2606–2611.
- [26] M. N. Berberan-Santos, E. N. Bodunov and B. Valeur, *Chem. Phys.*, 2005, **315**, 171–182.
- [27] C. W. Tang, S. A. Vanslyke and C. H. Chen, *Appl. Phys. Lett.*, 1989, **65**, 3610–3616.
- [28] R. Pandey, G. Méhes, A. Kumar, R. S. Singh, A. Kumar, C. Adachi and D. S. Pandey, *J. Lumin.*, 2017, **181**, 252–260.
- [29] Y. Beldjoudi, M. Nascimento, Y. J. Cho, H. Yu, H. Aziz, D. Tonouchi, K. Eguchi, M. M. Matsushita, K. Awaga, I. O. Osorio-roman, C. P. Constantinides and J. M. Rawson, *J. Am. Chem. Soc.*, 2018, **140**, 6260–6270.
- [30] X. Ai, E. W. Evans, S. Dong, A. J. Gillett, H. Guo, Y. Chen, T. J. H. Hele, R. H. Friend and F. Li, *Nature*, 2018, **563**, 536–540.
- [31] A. Abdurahman, T. J. H. Hele, Q. Gu, J. Zhang, Q. Peng, M. Zhang, R. H. Friend, F. Li and E. W. Evans, *Nat. Mater.*, 2020, **19**, 1224–1229.
- [32] C. Liu, E. Hamzehpoor, Y. Sakai-Otsuka, T. Jadhav and D. F. Perepichka, *Angew. Chem. Int. Ed.*, 2020, **59**, 23030–23034.
- [33] V. Ptatschek, B. Schreder, K. Herz, U. Hilbert, W. Ossau, G. Schottner, O. Raha, T. Bischof, G. Lermann, A. Materny, W. Kiefer, G. Bacher, A. Forchel, D. Su, M. Giersig, G. Mu and L. Spanhel, *J. Phys. Chem. B*, 1997, **101**, 8898–8906.
- [34] A. L. Wong, J. M. Harris and D. B. Marshall, *Can. J. Phys.*, 1990, **68**, 1027–1034.
- [35] R. Métivier, I. Leray, J.-P. Lefèvre, M. Roy-Auberger, N. Zanier-Szydłowski and B. Valeur, *Phys. Chem. Chem. Phys.*, 2003, **5**, 758–766.
- [36] M. Kasha, *Discuss. Faraday Soc.*, 1950, **9**, 14–19.
- [37] Y. Zhang, G. P. Berman and S. Kais, *Int. J. Quant. Chem.*, 2015, **115**, 1327–1341.

- [38] M. Murakami, K. Maeda and T. Arai, *J. Phys. Chem. A*, 2005, **109**, 5793–5800.
- [39] S. Stob, J. Kemmink and R. Kaptein, *J. Am. Chem. Soc.*, 1989, **111**, 7036–7042.
- [40] L. M. Antill and J. R. Woodward, *J. Phys. Chem. Lett.*, 2018, **9**, 2691–2696.

Chapter 4

Magnetoluminescence of PyBTM-based Zn^{II} complexes doped in matrices

4-1 Introduction

In Chapter 3, I have demonstrated that PyBTM doped into αH -PyBTM molecular crystals exhibits magnetic-field-sensitive luminescence, magnetoluminescence as the first examples of spin-luminescence correlated properties of organic radicals.¹ The studies suggested that changes in spin multiplicities of aggregated radicals played a key role of the MFE. However, magnetoluminescence of stable radicals has to date been observed for only a few pure organic luminescent radicals. Therefore, it is important to expand the scope of candidates displaying magnetoluminescence to achieve novel spin-correlated photofunctions in organic radicals. Especially, the development of metal–radical complexes showing magnetoluminescence is a promising strategy because of the designability for controlling the molecular and electronic structures.

In this chapter, I prepared $Zn^{II}(hfac)_2(\alpha H\text{-PyBTM})_2$ (Figure 4-1-1a) crystals in which αH -PyBTM was substituted with various concentrations of PyBTM (**PyZn_R**, where R indicates the concentration (wt%) of PyBTM), and investigated their luminescent properties under an external magnetic field.² **PyZn_5**, **PyZn_10**, and **PyZn_20** are the first reported compounds for luminescent radical-ligated metal complexes showing excimer emissions. Their luminescence behaviors were modulated significantly by applying magnetic fields, suggesting that magnetoluminescence properties is common, even in radical-based metal complexes. In this system, two types of spin multiplicity changes, which would contribute to the magnetoluminescence, can occur: intramolecular spin multiplicity changes in $Zn^{II}(hfac)_2(PyBTM)_2$ (Figure 4-1-1b) and intermolecular changes in the dimer of $Zn^{II}(hfac)_2(\alpha H\text{-PyBTM})(PyBTM)$ (Figure 4-1-1c). Here I discuss which of these spin multiplicity changes contributed to the MFE.

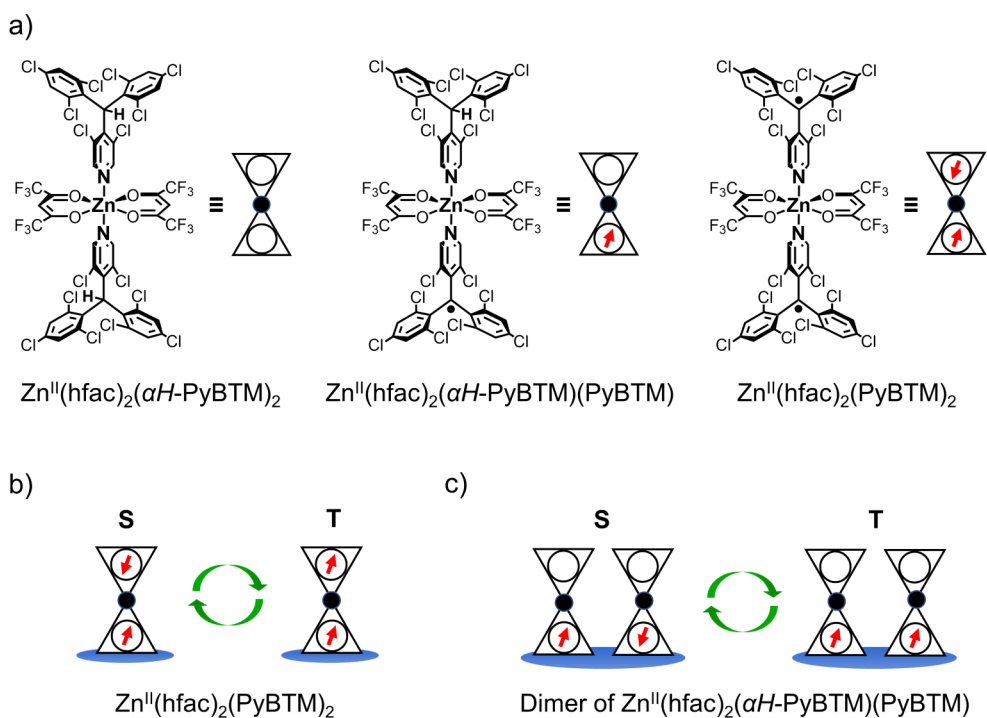


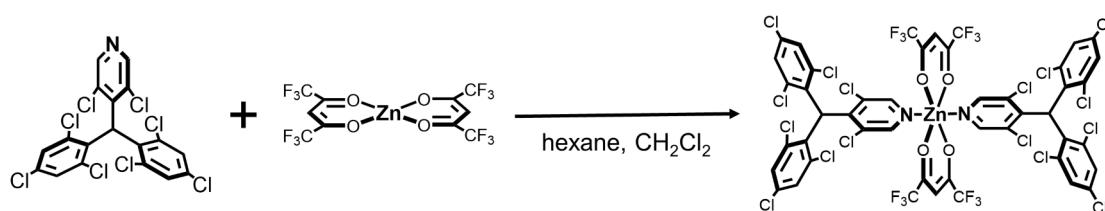
Figure 4-1-1. Molecular structures and possible spin multiplicity changes. (a) Molecular structures of $\text{Zn}^{\text{II}}(\text{hfac})_2(\alpha H\text{-PyBTM})_2$, $\text{Zn}^{\text{II}}(\text{hfac})_2(\alpha H\text{-PyBTM})(\text{PyBTM})$, and $\text{Zn}^{\text{II}}(\text{hfac})_2(\text{PyBTM})_2$. (b)(c) possible spin multiplicity changes in (b) $\text{Zn}^{\text{II}}(\text{hfac})_2(\text{PyBTM})_2$ and (c) dimer of $\text{Zn}^{\text{II}}(\text{hfac})_2(\alpha H\text{-PyBTM})(\text{PyBTM})$.

4-2 Experimental section

4-2-1 Materials

All chemicals were reagent grade and purchased commercially. Water was purified using AUTOPURE WD500 (Yamato Scientific Co., Ltd.). Dichloromethane (CH_2Cl_2), diethyl ether (Et_2O), *n*-hexane and tetrahydrofuran (THF) used for syntheses were purified through organic solvent purifier (Nikko Hansen Co., Ltd.). PyBTM and αH -PyBTM were prepared according to the procedures reported in the literature.³

4-2-2 Synthesis of $\text{Zn}^{\text{II}}(\text{hfac})_2(\alpha H\text{-PyBTM})_2$



Under nitrogen atmosphere, $\text{Zn}^{\text{II}}(\text{hfac})_2 \cdot 2\text{H}_2\text{O}$ (21.0 mg, 0.041 mmol) was dissolved in dry *n*-hexane (10 mL) under reflux. αH -PyBTM (46.0 mg, 0.088 mmol) dissolved in dry *n*-hexane (3 mL) and dry CH_2Cl_2 (1 mL) was added to the solution at 80 °C, and stirred for 3 h. The resulted suspension was kept overnight at room temperature. The white precipitate was collected, washed with *n*-hexane, and dried in vacuo. Recrystallization from CH_2Cl_2 -*n*-hexane afforded $\text{Zn}^{\text{II}}(\text{hfac})_2(\alpha H\text{-PyBTM})_2$ (44.5 mg, 0.029 mmol) in 71% yield. Elem. Anal. Calcd for $\text{C}_{46}\text{H}_{16}\text{Cl}_{16}\text{F}_{12}\text{N}_2\text{O}_4\text{Zn}$: C, 36.32; H, 1.06; N, 1.84. Found: C, 36.01; H, 1.26; N, 1.95. ^1H NMR (400 MHz, CDCl_3) δ 8.48 (s, 1H), 8.35 (s, 1H), 7.41 (d, $J = 2.2$ Hz, 1H), 7.39 (d, $J = 2.2$ Hz, 1H), 7.29 (d, $J = 2.1$ Hz, 1H), 7.25 (d, $J = 2.1$ Hz, 1H), 6.72 (s, 1H), 6.12 (s, 1H). The peaks attributed to αH -PyBTM were almost matched with those of isolated αH -PyBTM in CDCl_3 ,³ suggesting the dissociation in CDCl_3 . ^{13}C NMR (100 MHz, CDCl_3) δ 180.5, 180.2, 179.8, 179.5, 148.6, 147.1, 146.9, 137.9, 137.5, 137.2, 137.1, 135.8, 134.8, 134.7, 132.2, 131.8, 130.4, 130.0, 128.8, 128.5, 121.5, 118.6, 115.8, 112.9, 90.0, 49.8.

4-2-3 Instruments and experimental methods

Instrumentation

^1H and ^{13}C NMR spectra were recorded with a JEOL JNM-ECS400 spectrometer at room temperature. Chemical shifts in ppm were referenced to tetramethylsilane (0.00 ppm) as an internal standard. Steady-state emission and excitation spectra at room temperature were measured with JASCO FP8600 spectrometers. Excitation spectra of **PyZn_10** were measured by dispersing in water and corrected by subtracting those of $\text{Zn}^{\text{II}}(\text{hfac})_2(\alpha\text{H-PyBTM})_2$. Sample solutions were bubbled with argon before measurement. Absolute photoluminescence quantum yields were measured with a Hamamatsu Photonics Quantaaurus-QY C11347-01. Fluorescence lifetime measurements were performed using a measurement system with a picosecond diode laser with the emission wavelength of 375 nm (Advanced Laser Diode Systems PIL037X) as a light source, a single grating spectrometer (Andor Kymera193i-B1), and a multichannel CCD detector (Andor iDus DV420A-OE). Powder X-ray diffraction were performed using Rigaku MiniFlex with $\text{Cu-K}\alpha$ radiation, operating at 40 kV and 15 mA.

The data for single crystal X-ray diffraction analysis were collected at 123 K on a ROD, Synergy Custom system (Rigaku Oxford Diffraction) equipped with mirror monochromated $\text{Mo-K}\alpha$ radiation. A suitable single crystal was mounted on a looped film (micromount) with Paraton-N. Data were processed using CrysAlisPro 1.171.39.43c (Rigaku Oxford Diffraction). The structure was solved using ShelXT⁴ and the whole structure was refined against F^2 with SHELXL-2018/3.⁵ All non-hydrogen atoms were refined anisotropically. Hydrogen atoms were located in idealized positions and were refined using a riding model with fixed thermal parameters. Crystal structure data (CIF, CCDC 2008148) can be obtained free of charge from The Cambridge Crystallographic Data Centre.

Luminescence measurement under magnetic field

The system for luminescence measurement under magnetic field consists of a picosecond diode laser with the emission wavelength of 375 nm (Advanced Laser Diode Systems PIL037X) as a light source, a single grating spectrometer (Andor Kymera193i-B1), and a multichannel CCD detector (Andor iDus DV420A-OE). This optical measurement system is combined with a solenoid type superconducting magnet, which can generate up to 18 T.⁶ Optical fibers are used to lead a light from light sources to a sample at the center of the superconducting magnet and from the sample to the spectrometer. The system of the vicinity of a sample follows that of Chapter 3.

Deconvolution of the emission spectra of **PyZn_5** and **PyZn_10**

The emission spectra of **PyZn_5** and **PyZn_10** were deconvoluted into monomer and excimer emission components. The emission spectrum of **PyZn_1** was utilized as the monomer emission component, which could be fitted to the sum of four Gaussian bands with wavenumber as the x-axis (Figure 4-2-1a). Figure 4-2-1b showed the excimer emission component, consisted of two Gaussian bands and estimated from the difference between the emission spectra of **PyZn_1** and **PyZn_5**. The results of the deconvolutions were shown in Figures 4-2-2 and 4-3-9 shown later is the spectra where x-axes of Figure 4-2-2 were converted into wavelength.

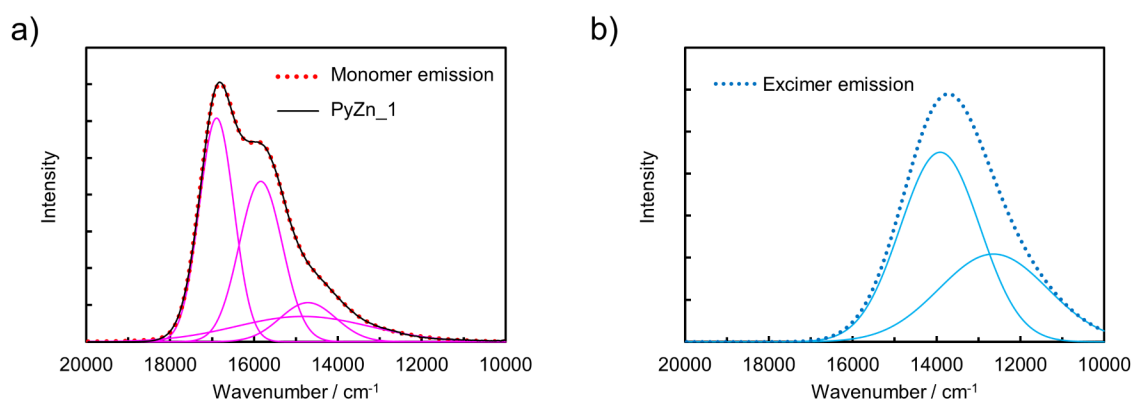


Figure 4-2-1. Deconvoluted monomer and excimer emission components. (a) The monomer and (b) excimer emission components and their Gaussian bands used for the deconvolution of the emission spectra of **PyZn_5** and **PyZn_10**.

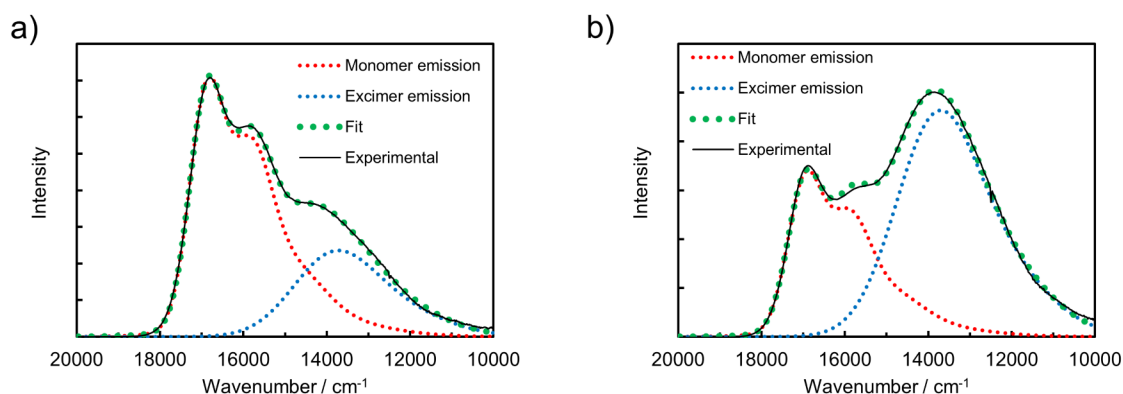


Figure 4-2-2. Deconvolutions of emission spectra of (a) **PyZn_5 and (b) **PyZn_10**.**

4-3 Results and Discussion

4-3-1 Preparation of **PyZn_R**

$\text{Zn}^{\text{II}}(\text{hfac})_2(\alpha H\text{-PyBTM})_2$ was prepared and characterized by the procedure described in the experimental section. The crystal structure of $\text{Zn}^{\text{II}}(\text{hfac})_2(\alpha H\text{-PyBTM})_2$ was revealed by a single-crystal X-ray diffraction analysis (Figure 4-3-1 and Table 4-3-1). It has the triclinic space group $P-1$ and the unit cell contains two crystallographically independent $\text{Zn}^{\text{II}}(\text{hfac})_2(\alpha H\text{-PyBTM})_2$ molecules with almost identical structures. The crystals of $\text{Zn}^{\text{II}}(\text{hfac})_2(\alpha H\text{-PyBTM})_2$ and $\text{Zn}^{\text{II}}(\text{hfac})_2(\text{PyBTM})_2$ ⁷ were isostructural except for the positions of the central carbon atoms of (αH -)PyBTM moieties; those in the former crystals were sp^3 -hybridized and disordered into two positions and those in the latter crystals were sp^2 -hybridized. Trifluoromethyl groups in the hfac ligands were also disordered at two positions in one of the two crystallographically independent molecules.

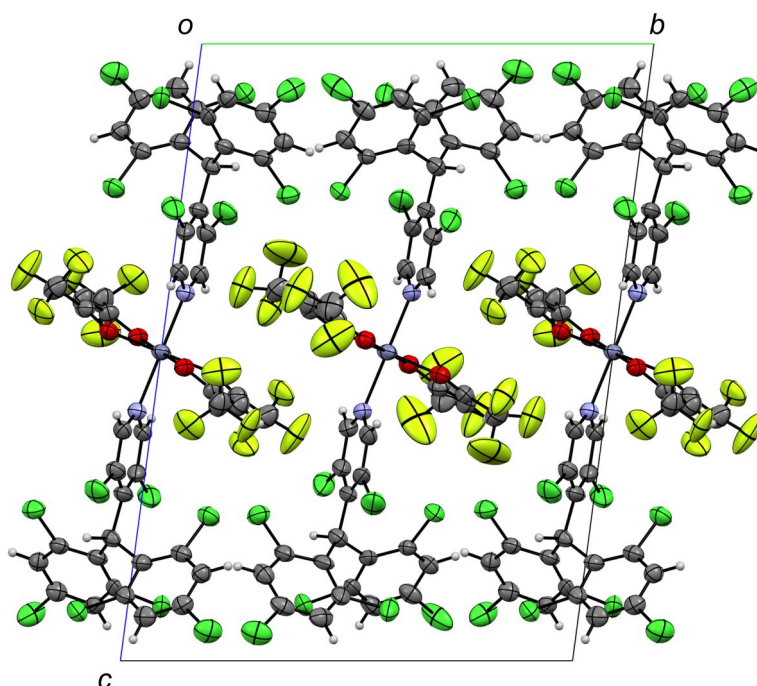


Figure 4-3-1. Crystal structure. Crystal structure of $\text{Zn}^{\text{II}}(\text{hfac})_2(\alpha H\text{-PyBTM})_2$ viewed along the a -axis. Disorders of the central carbon atoms of αH -PyBTM and the trifluoromethyl groups are omitted for clarity.

Table 4-3-1. Crystallographic data of $\text{Zn}^{\text{II}}(\text{hfac})_2(\alpha\text{H-PyBTM})_2$

Empirical formula	$\text{C}_{46}\text{H}_{16}\text{Cl}_{16}\text{F}_{12}\text{N}_2\text{O}_4\text{Zn}$
$F_w / \text{g mol}^{-1}$	1521.18
Crystal system	Triclinic
Space group	$P\bar{1}$
Crystal size / mm	$0.20 \times 0.03 \times 0.03$
Temperature / K	123
$a / \text{\AA}$	8.9829(6)
$b / \text{\AA}$	15.1174(8)
$c / \text{\AA}$	20.8813(7)
$\alpha / ^\circ$	97.411(4)
$\beta / ^\circ$	94.728(4)
$\gamma / ^\circ$	90.909(5)
$V / \text{\AA}^3$	2801.4(3)
$\rho_{\text{calcd}} / \text{g cm}^{-3}$	1.803
$\lambda / \text{\AA}$	0.71073
μ / mm^{-1}	1.288
Reflection collected	34662
Independent reflections	12845
Parameters	809
R_{int}	0.0519
R_1^a	0.0792
wR_2^b	0.2601
GoF ^c	1.090

^a $R_1 = \Sigma ||F^o| - |F^c|| / \Sigma |F^o|$ ($I > 2\sigma(I)$). ^b $wR_2 = [\Sigma (w(F^{o2} - F^{c2})^2 / \Sigma w(F^{o2})^2)]^{1/2}$ ($I > 2\sigma(I)$).

^cGoF = $[\Sigma (w(F^{o2} - F^{c2})^2 / \Sigma (N^r - N^p)^2)]$.

PyZn_R was prepared by following procedures. PyBTM, αH -PyBTM, and $\text{Zn}^{\text{II}}(\text{hfac})_2$ were dissolved in dry CH_2Cl_2 and the solvent was slowly evaporated at room temperature in the dark. The precipitated crystals of **PyZn_R** were collected and washed with dry *n*-hexane. The PXRD analyses revealed the uniformity of crystal structures of **PyZn_R** (Figure 4-3-2). The similarity among PXRD patterns of **PyZn_R**, $\text{Zn}^{\text{II}}(\text{hfac})_2(\alpha H\text{-PyBTM})_2$, and $\text{Zn}^{\text{II}}(\text{hfac})_2(\text{PyBTM})_2$ suggested that αH -PyBTM was substituted for PyBTM while maintaining the crystal structure as observed similarly in **Py_R** in Chapter 3. I assumed that three species, $\text{Zn}^{\text{II}}(\text{hfac})_2(\alpha H\text{-PyBTM})_2$, $\text{Zn}^{\text{II}}(\text{hfac})_2(\alpha H\text{-PyBTM})(\text{PyBTM})$, and $\text{Zn}^{\text{II}}(\text{hfac})_2(\text{PyBTM})_2$ were randomly mixed in the crystals as suggested in the following section.

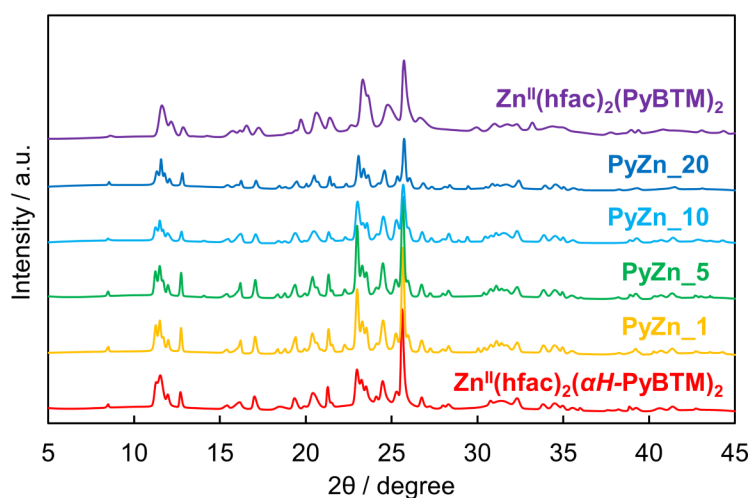


Figure 4-3-2. Powder X-ray diffraction patterns of **PyZn_R**.

4-3-2 Optical properties of **PyZn_R** at ambient conditions

The luminescence behaviors of **PyZn_R** were strongly dependent of the PyBTM concentration in the crystals. **PyZn_1**, with the lowest concentration, had a maximum emission wavelength, λ_{em} , of 595 nm upon photoexcitation at $\lambda_{\text{ex}} = 370$ nm (Figure 4-3-3). Considering the low radical concentration in the crystals, the luminescence originated from $\text{Zn}^{\text{II}}(\text{hfac})_2(\alpha\text{H-PyBTM})(\text{PyBTM})$, the complex with one PyBTM radical. The spectral shape was similar to that of **Py_1** in Chapter 3 ($\lambda_{\text{em}} = 563$ nm).¹ The emission wavelength was bathochromically shifted because of coordination to the positively charged Zn^{II} ion, as observed in Au^{I} -PyBTM complex; the coordination led lower the energy level of the β -SOMO, decreasing the emission energy.⁸⁻¹⁰ A new emission band around $\lambda_{\text{em}} = 725$ nm appeared and emission at $\lambda_{\text{em}} = 595$ nm was suppressed as the radical concentration increased. These trends are similar to those in **Py_R** in Chapter 3 and previous reports,^{1,11} and thus the new emission band was attributed to the excimer. Here, if $\text{Zn}^{\text{II}}(\text{hfac})_2(\text{PyBTM})_2$ was preferentially formed and thus **Py_R** consisted of the mixture of $\text{Zn}^{\text{II}}(\text{hfac})_2(\alpha\text{H-PyBTM})_2$ and $\text{Zn}^{\text{II}}(\text{hfac})_2(\text{PyBTM})_2$, the excimer emission could not appear with increasing the radical concentration. Therefore, these results confirmed that $\alpha\text{H-PyBTM}$ in $\text{Zn}^{\text{II}}(\text{hfac})_2(\alpha\text{H-PyBTM})_2$ crystals was randomly replaced with PyBTM. The excimer character was confirmed by the excitation spectra of **PyZn_10** at monomer- and excimer-centered emission wavelengths ($\lambda_{\text{em}} = 595$ and 725 nm, respectively). The similarity of the spectra suggested that the long-wavelength emission originated from the excimer formed in the excited states (Figure 4-3-4). Although both $\text{Zn}^{\text{II}}(\text{hfac})_2(\alpha\text{H-PyBTM})_2$ and the dimer of $\text{Zn}^{\text{II}}(\text{hfac})_2(\alpha\text{H-PyBTM})(\text{PyBTM})$ were possible excimer species, the species from which the excimer emission was derived could not be determined because they were randomly mixed in the crystals. The emission spectrum of isolated $\text{Zn}^{\text{II}}(\text{hfac})_2(\text{PyBTM})_2$ could not be obtained because PyBTM was dissociated in solution⁹ or during grinding with $\alpha\text{H-PyBTM}$ in the solid state (Figure 4-3-5). Considering the dissociations of ligated PyBTM in solution, **PyZn_R** prepared by co-crystallization of $\text{Zn}^{\text{II}}(\text{hfac})_2(\alpha\text{H-PyBTM})_2$ and $\text{Zn}^{\text{II}}(\text{hfac})_2(\text{PyBTM})_2$ is expected to have the same composition as **PyZn_R** in this study.

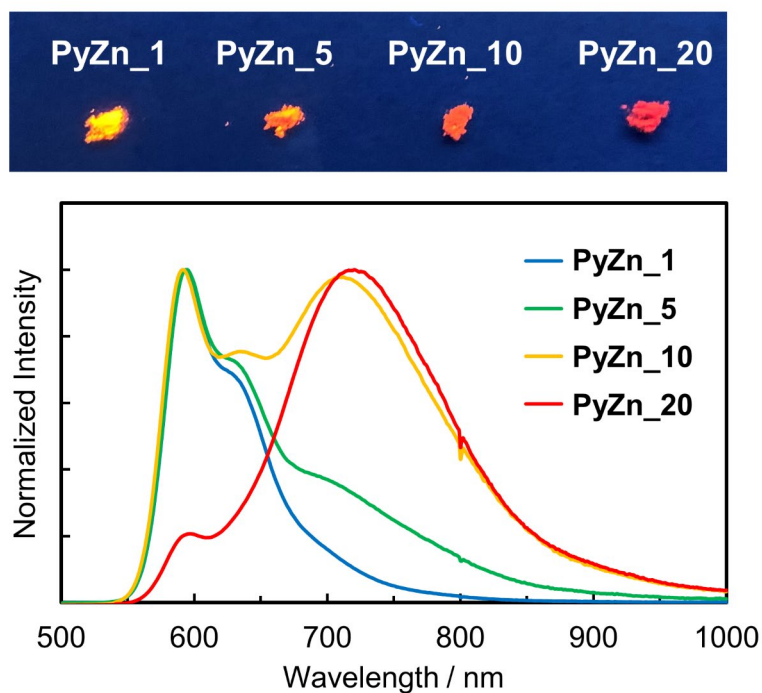


Figure 4-3-3. Normalized emission spectra (lower, $\lambda_{\text{ex}} = 370$ nm) and photograph (upper, $\lambda_{\text{ex}} = 365$ nm) of **PyZn_R**.

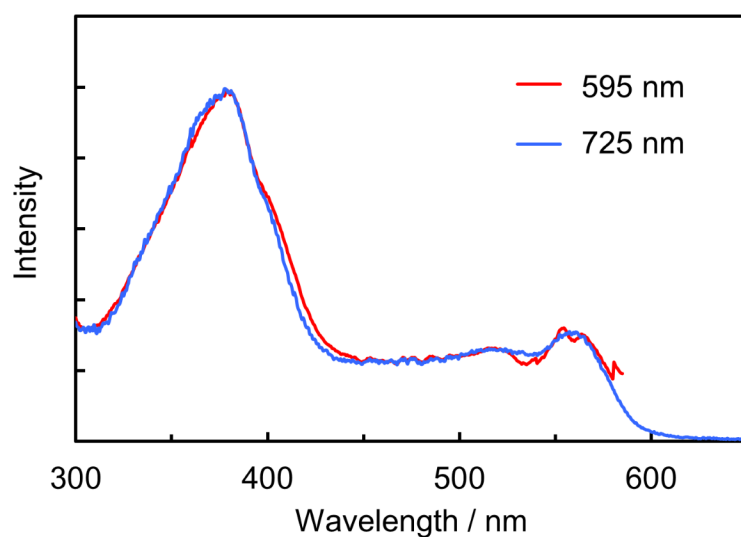


Figure 4-3-4. Excitation spectra. Excitation spectra of **PyZn_10** recorded at the emission wavelength of 595 and 725 nm.

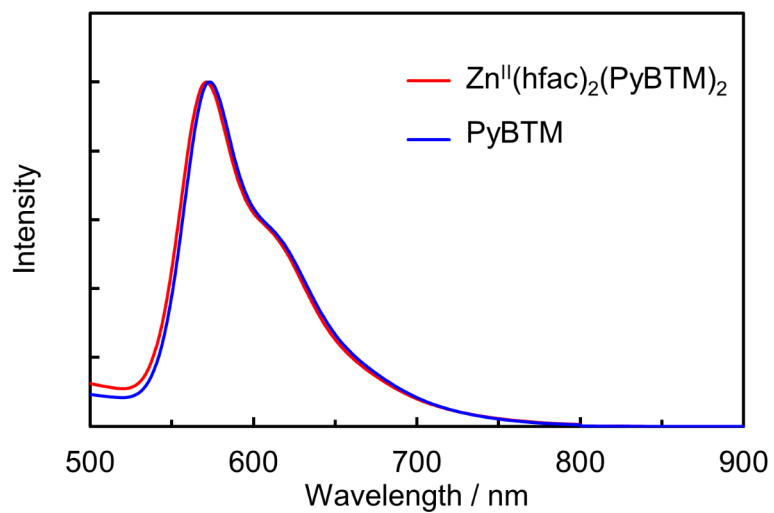


Figure 4-3-5. Emission spectra grinded with αH -PyBTM. Emission spectra of $\text{Zn}^{\text{II}}(\text{hfac})_2(\text{PyBTM})_2$ and PyBTM grinded with αH -PyBTM. The emission may result from free PyBTM dissociated by grinding.

Table 4-3-2 summarized the photophysical properties of **PyZn_R**. **PyZn_1** had the highest absolute emission quantum yield, ϕ_{em} , of 0.18. As PyBTM concentration increased, the excimer emission band emerged and ϕ_{em} decreased to 0.052 for **PyZn_20**. These behaviors can be explained by concentration quenching in the crystals and lower ϕ_{em} of excimer emission than that of monomer emission. The emission lifetimes of excimer-centered emissions for **PyZn_5**, **PyZn_10**, and **PyZn_20** were much longer than those of the monomer-centered emissions, and the emission decays were able to be fitted with single exponential curves (Figure 4-3-6). These results indicate that the excimer was a single component, and thus emissive species was either $\text{Zn}^{\text{II}}(\text{hfac})_2(\alpha\text{H-PyBTM})_2$ or the dimer of $\text{Zn}^{\text{II}}(\text{hfac})_2(\alpha\text{H-PyBTM})(\text{PyBTM})$.

Table 4-3-2. Photophysical properties of **PyZn_R**

radical concentration / wt%	ϕ_{em}	τ_1^{595} /ns	τ_2^{595} /ns	τ_3^{595} /ns	τ_1^{725} /ns	τ_2^{725} /ns
1	0.18	19 (56)	48 (43)	174 (1.0)	—	—
5	0.11	7.9 (63)	25 (35)	153 (2.0)	20 (87)	862 (13)
10	0.078	4.7 (73)	17 (26)	215- (1.7)	21 (76)	771 (24)
20	0.052	1.8 (90)	11 (8.0)	245 (1.7)	32 (18)	746 (82)

τ_1^{595} , τ_2^{595} , τ_3^{595} , τ_1^{725} , and τ_2^{725} are lifetime components (and relative amplitudes) for lifetimes at 595 and 725 nm. Short lifetime components at 725 nm, τ_1^{725} , can be attributed to monomer emissions overlapped at the measured wavelength.

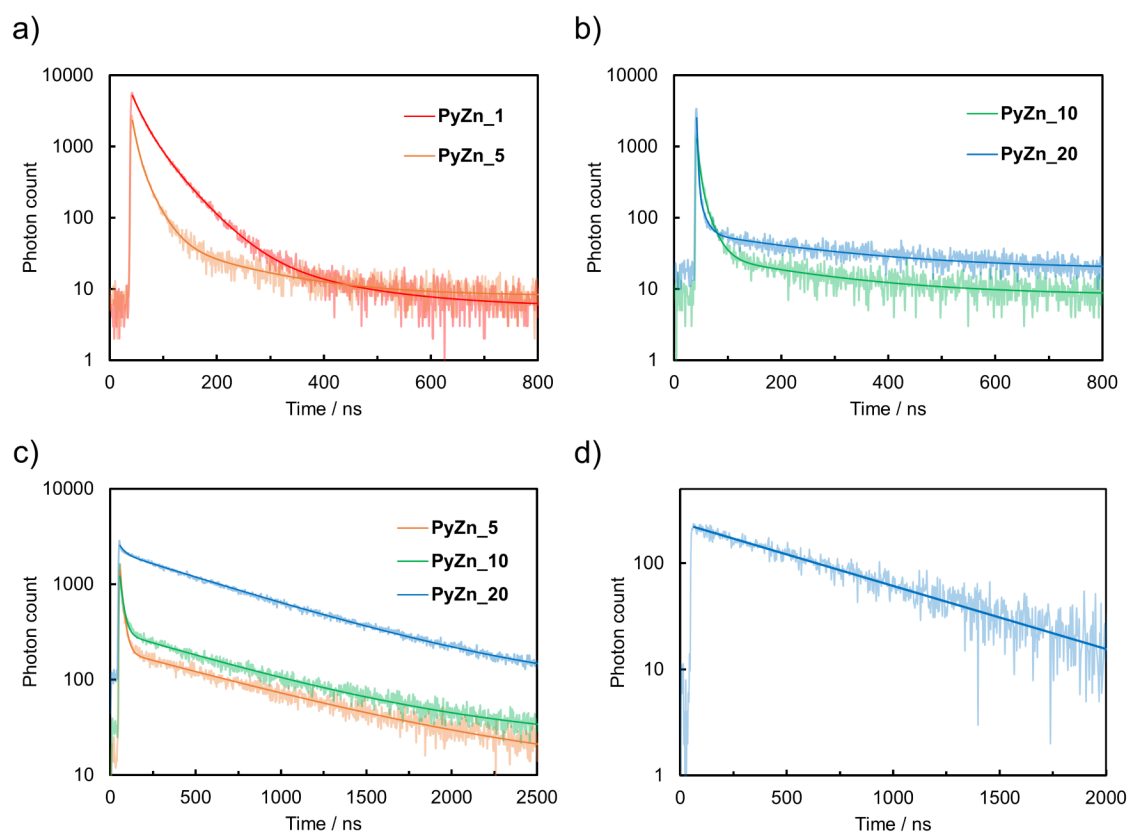


Figure 4-3-6. Emission decays of PyZn_R. Emission decays and corresponding fitted curves of **PyZn_R** at (a)(b) 595 and (c) 725 nm and (d) those of **PyZn_10** at 900 nm.

4-3-3 Magnetoluminescence of **PyZn_R**

The emission spectra of **PyZn_R** at 4.2 K under a magnetic field were measured to investigate their magnetoluminescence behaviors. Figure 4-3-7a shows the emission spectra of **PyZn_1**, which exhibited only monomer-centered emission, under external magnetic fields of up to 18 T. These spectra were identical and not affected by the magnetic fields, demonstrating an absence of MFE. This is consistent with the results in Chapter 3, where isolated PyBTM in host matrices did not show magnetoluminescence because of its luminescence based on the doublet character.¹ On the other hand, the emissions from the crystals with higher PyBTM concentrations, **PyZn_5**, **PyZn_10**, and **PyZn_20**, which exhibited both monomer- and excimer-centered emissions, clearly showed the responses to the external magnetic fields (Figure 4-3-7b-d). The monomer-centered emission at $\lambda_{\text{em}} = 595$ nm was substantially enhanced and the excimer-centered emission at $\lambda_{\text{em}} = 740$ nm was slightly suppressed as the applied magnetic field increased. These are the first examples of magnetoluminescence for the metal complexes with a ligated luminescent radical. The intensity changes at monomer- and excimer-centered emission wavelengths for **PyZn_5**, **PyZn_10**, and **PyZn_20** are shown in Figure 4-3-8a-c. Figure 4-3-8d shows difference emission spectra of **PyZn_10**. The magnitudes of the intensity changes at the monomer and excimer emissions were correlated, and the increased monomer emission intensities were much larger than the decreased excimer emission intensities (21, 18, and 28 times for **PyZn_5**, **PyZn_10**, and **PyZn_20**, respectively). These results suggested much higher ϕ_{em} of the monomer excited states than those of the excimer excited states.

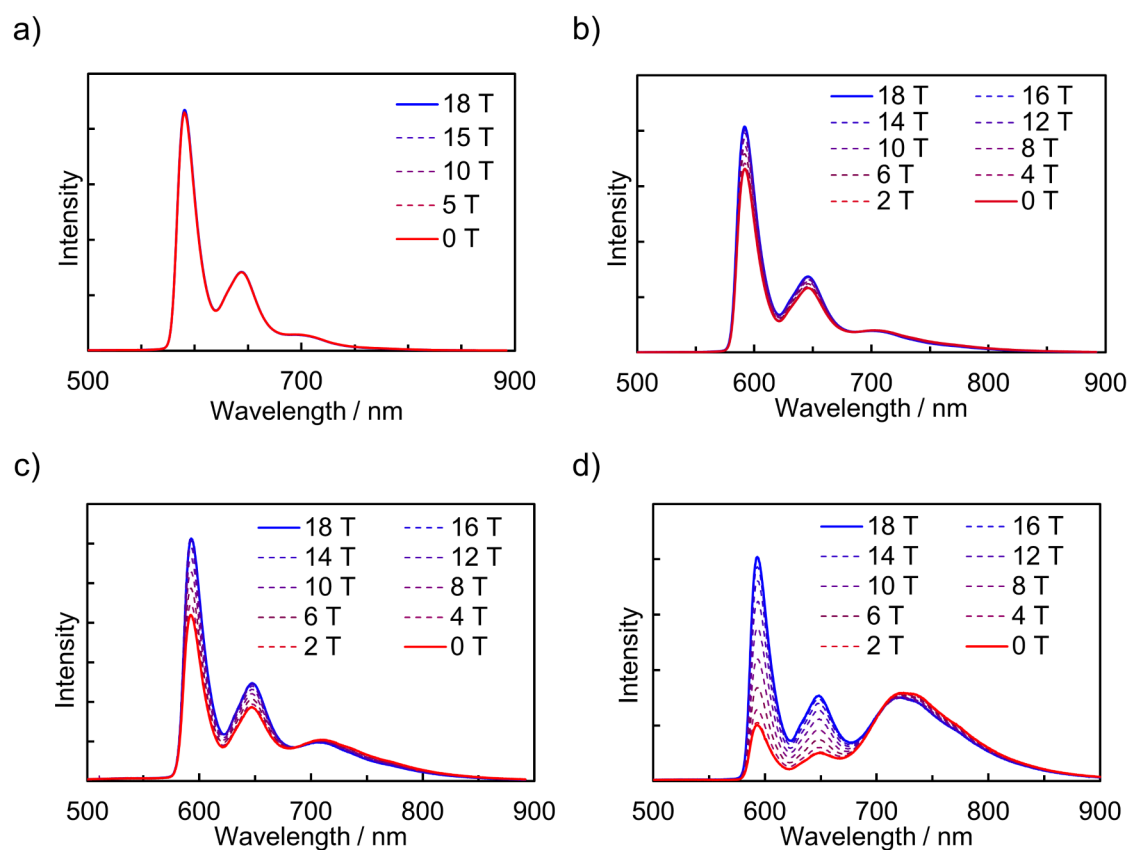


Figure 4-3-7. Magnetoluminescence of PyZn_R. Emission spectra of (a) **PyZn_1**, (b) **PyZn_5**, (c) **PyZn_10**, and (d) **PyZn_20** at 4.2 K under magnetic fields from 0 to 18 T.

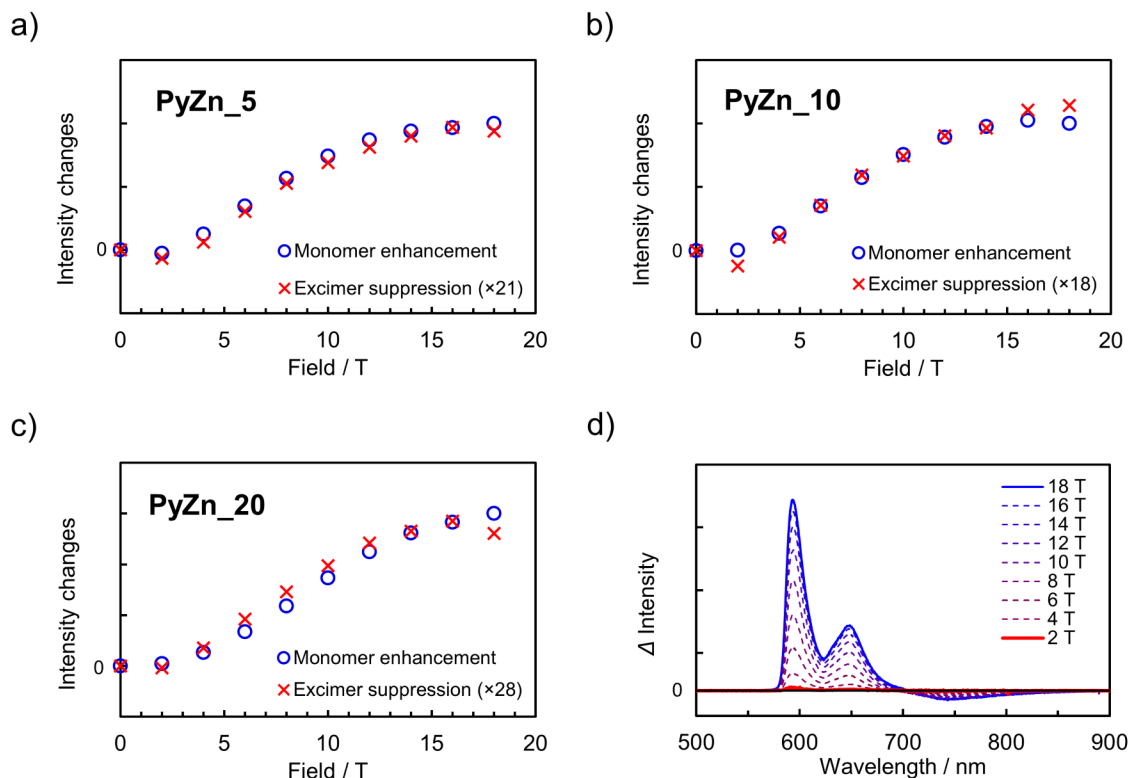


Figure 4-3-8. Intensity changes and difference emission spectra of PyZn_R under a magnetic field. Intensity changes of (a) **PyZn_5**, (b) **PyZn_10**, and (c) **PyZn_20** at monomer and excimer emission wavelengths ($\lambda_{\text{em}} = 595$ and 740 nm, respectively) at 4.2 K under magnetic fields from 0 to 18 T. Monomer enhancement and excimer suppression indicate the increase in monomer emission intensity and the decrease in excimer emission intensity from intensities under 0 T, respectively. (d) Difference emission spectra (Δ intensity) of **PyZn_10** at 4.2 K under magnetic fields compared with the spectrum at 0 T.

In **PyZn_R**, both $\text{Zn}^{\text{II}}(\text{hfac})_2(\text{PyBTM})_2$ and the dimer of $\text{Zn}^{\text{II}}(\text{hfac})_2(\alpha H\text{-PyBTM})(\text{PyBTM})$ were possible species contributing to the excimer emissions and the magnetoluminescence. As suggested by the excimer emission decay curves fitted with single components, the species showing the excimer emissions was either one of these two species. To identify the species, I considered the following three points. First, the abundance ratio of $\text{Zn}^{\text{II}}(\text{hfac})_2(\text{PyBTM})_2$ should be statistically much smaller than that of $\text{Zn}^{\text{II}}(\text{hfac})_2(\alpha H\text{-PyBTM})(\text{PyBTM})$ in the crystals of **PyZn_5** and **PyZn_10** (1/38 and 1/18, respectively). Second, the magnetoluminescence behaviors suggest that ϕ_{em} of the monomer excited states were much superior to those of the excimer excited states (Figure 4-3-8). Third, the contribution (peak area) of excimer-centered emission (I_{exc}) was comparable to that of monomer-centered emission (I_{mono}) in the emission spectra of **PyZn_5** and **PyZn_10** ($I_{\text{mono}}:I_{\text{exc}} = 2.4:1.0$ and $0.6:1.0$, respectively; Figure 4-3-9). If the excimer species were $\text{Zn}^{\text{II}}(\text{hfac})_2(\text{PyBTM})_2$, I_{exc} should be much smaller than I_{mono} for **PyZn_5** and **PyZn_10** according to the first and second points above, but this would contradict the third point. I note that the energy transfers in the excited states from monomer emissive states to excimer emissive states can be negligible because emission decays of **PyZn_10** at 900 nm, in which excimer-centered emission were dominant, did not show any slow rising time (Figure 4-3-6d). Therefore, I concluded that the species showing the excimer emissions in **PyZn_R** was not $\text{Zn}^{\text{II}}(\text{hfac})_2(\text{PyBTM})_2$, but the dimer of $\text{Zn}^{\text{II}}(\text{hfac})_2(\alpha H\text{-PyBTM})(\text{PyBTM})$. Considering the similarity between magnetoluminescence behaviors of **PyZn_R** and those of **Py_R** explained in Chapter 3, a similar mechanism for the magnetoluminescence is expected, in which the spin multiplicity in both the ground and excited states were modulated by external magnetic fields (Figure 4-3-10).^{1,12}

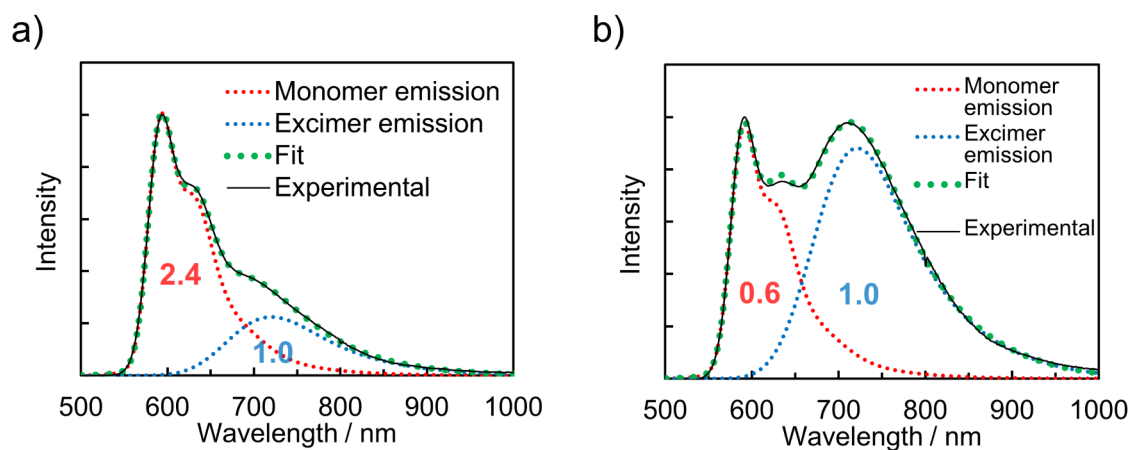


Figure 4-3-9. Deconvoluted emission spectra of PyZn_R. Emission spectra and their monomer and excimer emission components of (a) **PyZn_5** and (b) **PyZn_10** at room temperature.

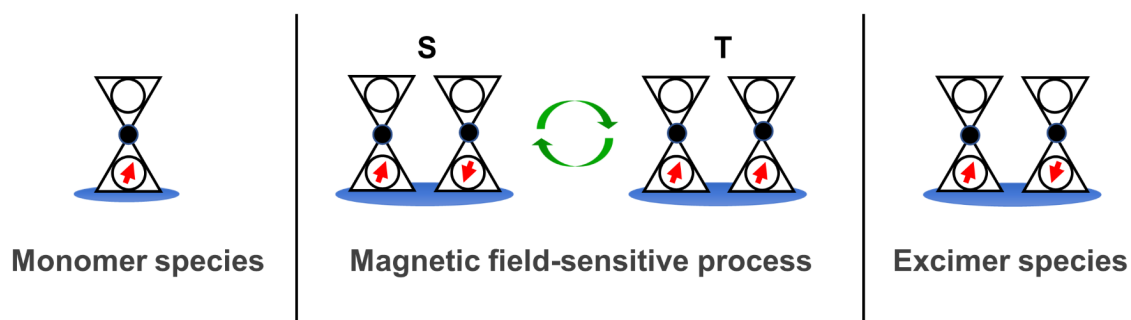


Figure 4-3-10. Proposed monomer species, magnetic field-sensitive process, and excimer species in PyZn_R.

4-4 Conclusions

In this chapter, the crystals of PyBTM-substituted $\text{Zn}^{\text{II}}(\text{hfac})_2(\alpha H\text{-PyBTM})_2$, **PyZn_R** were prepared and their luminescence behaviors were shown to depend on the PyBTM concentration and magnetic fields. **PyZn_1** showed emission from the isolated $\text{Zn}^{\text{II}}(\text{hfac})_2(\alpha H\text{-PyBTM})(\text{PyBTM})$ and the emission was insensitive to external magnetic fields. On the other hand, **PyZn_5**, **PyZn10**, and **PyZn_20** exhibited both monomer- and excimer-centered emissions and they were modulated significantly by external magnetic fields. These are the first observations of excimer emission and magnetoluminescence in metal complexes with ligated luminescent radicals. Considering their emission properties and MFEs on the luminescence behaviors, the excimer emissive species in this system was determined not as $\text{Zn}^{\text{II}}(\text{hfac})_2(\text{PyBTM})_2$ but as the dimer of $\text{Zn}^{\text{II}}(\text{hfac})_2(\alpha H\text{-PyBTM})(\text{PyBTM})$. These results suggest not only the generality of magnetoluminescence in doublet emitters but also the importance of the manner of interaction between radicals. Similarity in the MFEs on the luminescence behaviors between results in Chapter 3 and **PyZn_R** shown in the present study indicates that the magnetoluminescence is not compound-specific but common in luminescent radical compounds. Since complexations can control the inter/intramolecular interactions of spins, the development of magnetoluminescence in radical-ligated complexes would be a promising approach to develop novel spin-correlated photofunctions.

4-5 References

- [1] S. Kimura, T. Kusamoto, S. Kimura, K. Kato, Y. Teki and H. Nishihara, *Angew. Chem. Int. Ed.*, 2018, **57**, 12711–12715.
- [2] S. Kimura, S. Kimura, H. Nishihara and T. Kusamoto, *Chem. Commun.*, 2020, **56**, 11195–11198.
- [3] Y. Hattori, T. Kusamoto and H. Nishihara, *Angew. Chem. Int. Ed.*, 2014, **53**, 11845–11848.
- [4] G. M. Sheldrick, *Acta Cryst. A*, 2015, **71**, 3–8.
- [5] G. M. Sheldrick, *Acta Cryst. C*, 2015, **71**, 3–8.
- [6] Y. Sawada, S. Kimura, K. Watanabe and M. Nakano, *J. Low Temp. Phys.*, 2013, **170**, 424–429.
- [7] T. Kusamoto, Y. Hattori, A. Tanushi and H. Nishihara, *Inorg. Chem.*, 2015, **54**, 4186–4188.
- [8] Y. Hattori, T. Kusamoto and H. Nishihara, *Angew. Chem. Int. Ed.*, 2015, **54**, 3731–3734.
- [9] Y. Hattori, T. Kusamoto, T. Sato and H. Nishihara, *Chem. Commun.*, 2016, **52**, 13393–13396.
- [10] Y. Ogino, T. Kusamoto, Y. Hattori, M. Shimada, M. Tsuchiya, Y. Yamanoi, E. Nishibori, K. Sugimoto and H. Nishihara, *Inorg. Chem.*, 2017, **56**, 3909–3915.
- [11] D. Blasi, D. M. Nikolaidou, F. Terenziani, I. Ratera and J. Veciana, *Phys. Chem. Chem. Phys.*, 2017, **19**, 9313–9319.
- [12] K. Kato, S. Kimura, T. Kusamoto, H. Nishihara and Y. Teki, *Angew. Chem. Int. Ed.*, 2019, **58**, 2606–2611.

Chapter 5

Magnetoluminescence of radical-based coordination polymers

本章については、5 年以内に雑誌等で刊行予定のため、非公開。

Chapter 6

Concluding remarks

本章の一部については、5年以内に雑誌等で刊行予定のため、非公開。

As described in Chapter 1, organic radicals possessing unpaired electrons have been extensively studied to provide unique magnetic and electric properties, which are correlated with their spin states. In order to achieve spin-correlated properties unique to radicals, controlling a manner or a degree of assembly of radical molecules, which regulates the spin-spin interactions, would be a promising approach.

The aim of my Ph.D. research is to establish the novel luminescence properties of organic radicals based on interplay between spin and luminescence. While luminescent radicals have been the focus of the research as a new type of luminophores, such spin-correlated luminescence properties in organic radicals have never been accomplished despite their prospect as an approach to yield novel photofunctions unique to radicals. For the purpose, I prepared assembled (aggregated) radicals and investigated their luminescence properties in the studies.

First, 2D radical-based coordination polymers (CPs) were developed as a new class of assembly of radicals (Chapter 2) and then magnetic field effects (MFEs) on the luminescence, namely magnetoluminescence of radicals were developed as the first example of spin-correlated photofunctions of radicals (Chapters 3, 4, and 5).

In Chapter 3, emission properties of the PyBTM-doped αH -PyBTM molecular crystals, **Py_R** were investigated. **Py_0.05** showed an extraordinarily high room temperature ϕ_{em} of 0.89. **Py_R** showed monomer and excimer emissions depending on the doping concentration, suggesting the degree of aggregation of PyBTM was controlled by the doping ratio. The luminescence of **Py_0.1** at 4.2 K was not affected by magnetic field, demonstrating the absence of MFE on the emissions of isolated radicals. In contrast, the luminescence of **Py_4**, **Py_10**, and **Py_20** at 4.2 K were drastically modulated by external magnetic field. This is the first observation of magnetoluminescence of organic radicals. Moreover, the mechanism and key factors of the MFE were revealed by time-resolved emission measurements under a magnetic field and quantum simulations; the MFE was dominated by magnetic-field-sensitive spin sublevel populations of aggregated radicals in the ground states.

In Chapter 4, I described the magnetoluminescent behaviors of PyBTM-substituted $\text{Zn}^{\text{II}}(\text{hfac})_2(\alpha H\text{-PyBTM})_2$ crystals, **PyZn_R**. **PyZn_1** displaying luminescence from the monomer $\text{Zn}^{\text{II}}(\text{hfac})_2(\alpha H\text{-PyBTM})(\text{PyBTM})$ and did not show MFE on its emission. On the other hand, **PyZn_5**, **PyZn10**, and **PyZn_20** showed both monomer and excimer emissions, which were modulated strongly by the magnetic field. These results suggested the general nature of magnetoluminescence in radicals. Further spectroscopic studies determined the excimer emissive species as the $\text{Zn}^{\text{II}}(\text{hfac})_2(\alpha H\text{-PyBTM})(\text{PyBTM})$ dimer.

In conclusion, through developing the new radical compounds, I established the novel luminescence properties of organic radicals: magnetic-field-sensitive luminescence, magnetoluminescence, which are controlled by a degree of assembly of radicals. The materials, phenomena, and strategies demonstrated here open the door to a novel research field of radicals, “photofunctions based on the interplay between spin and luminescence”.

Appendix

本内容については、5年以内に雑誌等で刊行予定のため、非公開。

List of publications

Publication related to the thesis

1. "Magnetoluminescence in a Photostable, Brightly Luminescent Organic Radical in a Rigid Environment", Shun Kimura, Tetsuro Kusamoto, Shojiro Kimura, Ken Kato, Yoshio Teki and Hiroshi Nishihara, *Angew. Chem. Int. Ed.*, 2018, **39**, 12711–12715.
2. "Excimer emission and magnetoluminescence of radical-based zinc(II) complexes doped in host crystals", Shun Kimura, Shojiro Kimura, Hiroshi Nishihara and Tetsuro Kusamoto, *Chem. Commun.*, 2020, **56**, 11195–11198.
3. "Ground-state-dominated magnetic field effect on the luminescence of stable organic radicals", Shun Kimura, Shojiro Kimura, Ken Kato, Yoshio Teki, Hiroshi Nishihara and Tetsuro Kusamoto, *Chem. Sci.*, 2021, DOI: 10.1039/D0SC05965J.

Publications not related to the thesis

1. "One-dimensional magnetic chain composed of Cu^{II} and polychlorinated dipyridylphenylmethyl radical: temperature-dependent Jahn-Teller distortion correlated to π -conjugation and magnetic properties", Shun Kimura, Hikaru Uchida, Tetsuro Kusamoto and Hiroshi Nishihara, *Dalton Trans.*, 2019, **48**, 7090–7093.
2. "NIR Emission and Acid-Induced Intramolecular Electron Transfer Derived from a SOMO-HOMO Converted Non-Aufbau Electronic Structure", Akira Tanushi, Shun Kimura, Tetsuro Kusamoto, Moe Tomonaga, Yasutaka Kitagawa, Masayoshi Nakano and Hiroshi Nishihara, *J. Phys. Chem. C*, 2019, **123**, 4417–4423.
3. "Luminescent Radical-Excimer: Excited-State Dynamics of Luminescent Radicals in Doped Host Crystals", Ken Kato, Shun Kimura, Tetsuro Kusamoto, Hiroshi Nishihara and Yoshio Teki, *Angew. Chem. Int. Ed.*, 2019, **58**, 2606–2611.
4. "Cyclic heterometallic interactions formed from a flexible tripeptide complex showing effective antiferromagnetic spin coupling", Ryosuke Miyake, Eri Suganuma, Shun Kimura, Hirotoshi Mori, Jun Okabayashi and Tetsuro Kusamoto, *Angew. Chem. Int. Ed.*, DOI: 10.1002/anie.202013373.

Acknowledgement

In closing the thesis, I would like to appreciate everyone who supported me throughout my Ph.D. course.

First, I would like to express my sincere gratitude to my supervisor Professor Dr. Hiroshi Nishihara for his continuous support of the Ph.D. course research, for motivation, and helpful advice. I am also greatly thankful to Professor Dr. Mitsuhiko Shionoya for his warmest acceptance to join his research group and the supervision with a lot of support to my research in the final year of my Ph.D. course.

I am greatly thankful to my supervisor in Institute for Molecular Science, Associate Professor Dr. Tetsuro Kusamoto for his kind direction, discussion for my research and unfailing patience. I could not have imagined having a better advisor and mentor.

My sincere thanks also go to the staffs in Nishihara, Shionoya, and Kusamoto laboratories, Associate Professor Dr. Yoshinori Yamanoi, Assistant Professor Dr. Ryota Sakamoto, Project Assistant Professor Dr. Mariko Miyachi, Project Assistant Professor Dr. Kuo Fui Wu, Project Assistant Professor Dr. Hiroaki Maeda, Associate Professor Dr. Shohei Tashiro, Assistant Professor Dr. Hitoshi Ube, Assistant Professor Dr. Yusuke Takezawa, and Assistant Professor Dr. Ryota Matsuoka. They always helped me to conduct the research.

Many researchers technically supported this study. I appreciate Professor Dr. Tohru Sato, Dr. Motoyuki Uejima, and Mr. Ota Wataru in Kyoto University for theoretical calculations of trisPyM, Professor Dr. Yoshio Teki and Mr. Ken Kato in Osaka City University for the discussions and the quantum mechanical simulations to construct the MFE scheme, and Associate Professor Dr. Shojiro Kimura in Tohoku University for optical measurements under magnetic field.

I would like to deeply acknowledge to all members in Nishihara, Shionoya, and Kusamoto laboratories for their kind supports and all the fun.

I am indebted to JSPS Fellowship for Young Scientists and MERIT (Material Education program for the future leaders in Research, Industry, and Technology) in the MEXT Leading Graduate School Doctoral Program.

The most of Figures in Chapter 3 and 4 are reproduced from my publication on *Angewandte Chemie International Edition* published in 2018, *Chemical Science* published in 2021, and *Chemical Communications* published in 2020. I also thank to Royal Society of Chemistry and John Wiley & Sons, Inc. for allowing me to reuse them in this thesis.

Finally, I would like to express my greatest appreciation to my family for their unconditional love and support. Without them, I could not have completed my Ph.D. course.

December 2020

Shun Kimura